Postprint of: Zou Z., Hughes T., Scott M., Miao D., Sauer R., Efficient and robust quadratures for isogeometric analysis: Reduced Gauss and Gauss–Greville rules, COMPUTER METHODS IN APPLIED MECHANICS AND ENGINEERING, Vol. 392 (2022), 114722, DOI: 10.1016/j.cma.2022.114722

Efficient and Robust Quadratures for Isogeometric Analysis: Reduced Gauss and Gauss-Greville rules

Z. Zou[1], T.J.R Hughes[1], M.A. Scott[2,6], Di Miao[2], and R.A. Sauer[3,4,5]

[1]Oden Institute for Computational Engineering and Sciences, The University of Texas at Austin, Austin, TX USA
[2]Department of Civil and Environmental Engineering, Brigham Young University, Provo, UT USA
[3]Aachen Institute for Advanced Study in Computational Engineering Science, RWTH Aachen University, Aachen, Germany
[4]Faculty of Civil and Environmental Engineering, Gdańsk University of Technology, Gdańsk, Poland
[5]Department of Mechanical Engineering, Indian Institute of Technology, Kanpur, UP India
[6]Coreform LLC, Orem, UT, USA

2022-01-29

Abstract

This work proposes two efficient quadrature rules, reduced Gauss quadrature and Gauss-Greville quadrature, for isogeometric analysis. The rules are constructed to exactly integrate one-dimensional B-spline basis functions of degree p, and continuity class C^{p-k}, where k is the highest order of derivatives appearing in the Galerkin formulation of the problem under consideration. This is the same idea we utilized in [1], but the rules therein produced negative weights for certain non-uniform meshes. The present work improves upon [1] in that the weights are guaranteed to be positive for all meshes. The reduced Gauss quadrature rule is built element-wise according to the element basis degree and smoothness. The Gauss-Greville quadrature rule combines the proposed reduced Gauss quadrature and Greville quadrature [1]. Both quadrature rules involve many fewer quadrature points than the full Gauss quadrature rule and avoid negative quadrature weights for arbitrary knot vectors. The proposed quadrature rules are stable and accurate, and they can be constructed without solving nonlinear equations, therefore providing efficient and easy-to-use alternatives to full Gauss quadrature. Various numerical examples, including curved shells, demonstrate that they achieve good accuracy, and for $p = 5$ and 6 eliminate locking.

Keywords: reduced Gauss, Gauss-Greville, quadrature, isogeometric analysis

1 Introduction

Isogeometric analysis (IGA) [2] adopts the spline basis of CAD geometry as the basis for analysis. This unifying paradigm has the potential to eliminate the costly geometry clean-up and mesh generation steps which encumber traditional simulation workflows. Additionally, it also improves the simulation accuracy through geometrically exact analysis models and higher-order continuous spline

bases [3, 4, 5]. Higher-order smooth spline bases have important advantages over C^0-continuous Lagrange polynomial bases, including stronger capabilities in exactly representing complex models, offering diverse refinement schemes, such as h-, p- and k-refinements, without altering the geometry or its parameterization, and providing superior spectral approximation properties [4], etc. However, efficient and robust numerical implementation is still an open issue for IGA. Full Gauss quadrature rules, even though being used widely, are not efficient for IGA since they do not take into account the higher-order continuity of spline basis functions.

To take full advantage of the higher-order continuous spline basis, Hughes *et al.* [6] initiated the study of efficient quadrature rules for NURBS-based IGA and proposed the so-called "half-point rule" by leveraging the precise smoothness of basis functions across element boundaries. The half-point rule is optimal in the sense that it uses a minimal number of quadrature points to exactly integrate the polynomials appearing in the isogeometric Galerkin methods. Subsequently, extensive research efforts have been made to devise robust ways to obtain optimal or nearly optimal quadrature rules. The authors in [7, 8] proposed to solve local nonlinear equation systems to obtain sub-optimal quadrature rules. Johannessen [9] provided algorithms to determine optimal rules by taking Greville abscissae as the initial guess of solving global nonlinear equations. In addition to solving nonlinear equations, explicit recursion methods [10, 11, 12, 13] were used as alternative strategies for finding these rules for spline bases with restricted degrees and continuities. Besides the above optimal or nearly optimal quadrature rules, Calabrò *et al.* [14] presented a weighted quadrature rule together with a row-loop assembling algorithm to speed the formation of isogeometric matrices, which was extended to linear elasticity later in [15]. Various element-based reduced quadratures are also explored in [16] for computational efficiency, in which different classical quadrature rules are used for interior and boundary elements to achieve accuracy and stability.

Recently, Zou *et al.* [1] proposed Greville quadrature rules for isogeometric shell analysis. The Greville quadrature rules can be easily constructed without solving nonlinear equations and have been shown to achieve comparable accuracy as full Gauss quadrature rules but with significantly gain in efficiency. Unfortunately, for nonuniform knot vectors they may involve negative quadrature weights for non-uniform knot vectors, which are not preferred in numerical methods due to potential instability. In the present work, new quadrature rules are devised to obviate the negative weight issue that may occur with Greville quadrature rules.

1.1 Key contributions

We first propose a reduced Gauss quadrature rule for IGA, which can be easily constructed on the element level without solving any linear or nonlinear equations. Given a one-dimensional element with knot interval $[\xi_i, \xi_{i+1}]$, the number of Gauss quadrature points is simply $n = \max\{\lceil (m_i + m_{i+1})/2 \rceil, \lceil (p+1)/2 \rceil\}$, where m_i and m_{i+1} are the multiplicities of the knots ξ_i and ξ_{i+1}, p is the degree of basis functions, and $\lceil * \rceil$ is the ceiling function, which indicates the smallest integer greater than or equal to the number $*$. Unlike existing reduced quadrature rules, the proposed reduced Gauss quadrature rule is free of rank deficiency and spurious energy modes regardless of the basis degrees and interelement continuities. Additionally, compared with the Greville quadrature rules in [1], it has the following merits:

- Quadrature weights are positive for arbitrary knot vectors.
- The quadrature rule can be constructed on the element level without solving any equations.
- The quadrature rule, when applied to Galerkin formulations for fourth-order partial differential equations, asymptotically involves only two quadrature points per element in each para-

metric direction for quadratic and cubic bases. In contrast, the Greville quadrature rule [1] asymptotically requires three quadrature points.

- The convergence rate is one order higher than that for the Greville quadrature rules for even-order bases with degrees $p > 2$.

Even though the proposed reduced Gauss quadrature rule involves many fewer quadrature points than the full Gauss quadrature rule, the number of quadrature points increases as the basis degree increases. To decrease the number of quadrature points for higher-order bases, we then propose a combined quadrature rule, called the Gauss-Greville quadrature rule. As its name suggests, the Gauss-Greville quadrature rule employs the Greville quadrature rule on domains, where all Greville quadrature weights are positive, and the proposed reduced Gauss quadrature rule on elements that involve negative Greville quadrature weights. Since negative Greville quadrature weights only appear in areas where element sizes change abruptly, most Greville quadrature weights for a given spline are positive. Therefore, the compound Gauss-Greville quadrature rule avoids negative quadrature weights while keeping the number of quadrature points about the same as for the Greville quadrature rules [1], i.e., asymptotically requiring two and three points per element in each parametric direction for Galerkin formulations for second-order and fourth-order differential equations, respectively.

These rules are particularly efficient for shell applications with $p = 5$ and 6, in that they mitigate locking phenomena, and in particular membrane-bending locking. For a full description of the merits of Greville quadrature in shell analysis, see [1].

The outline of the remainder of this paper is as follows. In Section 2 notations are defined, and fundamental spline concepts and the Greville quadrature rules are reviewed. Section 3 describes the proposed reduced Gauss and Gauss-Greville quadrature rules, followed by stability and accuracy validation with generalized eigenvalue problems in Section 4. Several numerical examples are then solved in Section 5 and conclusions are drawn in Section 6.

2 Spline fundamentals and Greville quadratures

2.1 Spline bases

The Ith Bernstein polynomial of degree p on $[\xi_1, \xi_2]$ can be defined as

$$B_I^p(\xi) = \binom{p}{I-1} \left(\frac{\xi_2 - \xi}{\xi_2 - \xi_1}\right)^{p-I+1} \left(\frac{\xi - \xi_1}{\xi_2 - \xi_1}\right)^{I-1}, \tag{1}$$

where $\binom{p}{I-1} = \frac{p!}{(I-1)!(p-I+1)!}$ is a binomial coefficient. A univariate quadratic Bernstein basis on $[0, 1]$ is shown in Figure 1a. A degree p Bézier curve in $\mathbb{R}^d$ can be written as

$$\mathbf{x}(\xi) = \sum_{I=1}^{p+1} \mathbf{P}_I \, B_I^p(\xi), \quad \xi \in [\xi_1, \xi_2], \tag{2}$$

where $\mathbf{P}_I \in \mathbb{R}^d$ is called a control point.

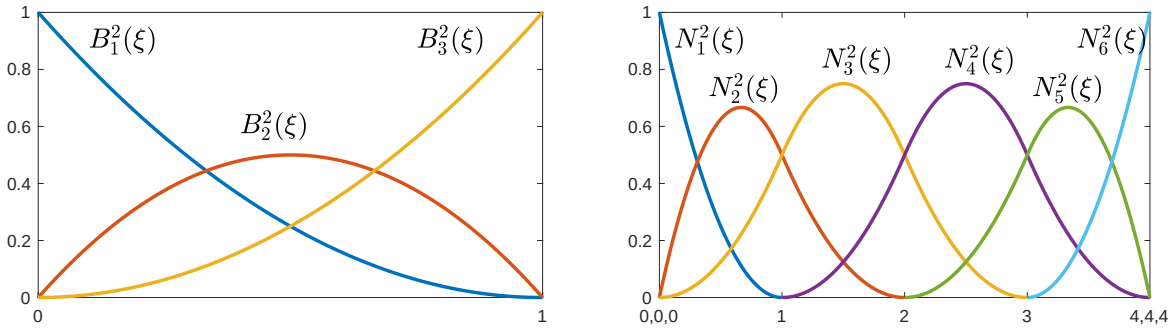

(a) Bernstein basis on $[0, 1]$.

(b) B-spline basis, $\Xi = \{0, 0, 0, 1, 2, 3, 4, 4, 4\}$.

Figure 1: A univariate quadratic Bernstein basis (a), a univariate quadratic C^1 B-spline basis (b).

A univariate B-spline basis can be defined by a knot vector $\Xi = \{\xi_1, \xi_2, \ldots, \xi_{n+p+1}\}$, which consists of a non-decreasing sequence of real numbers (i.e., knots), $\xi_I \leq \xi_{I+1}, I = 1, \ldots, n+p$, where p is the degree of the B-spline basis and n is the number of basis functions. A knot vector Ξ is called a uniform knot vector if all its knots are equally spaced. An open uniform knot vector refers to a knot vector with all its knots equally spaced except for $p+1$ repeated knots at each end.

The Ith B-spline basis function of degree p, denoted by $N_I^p(\xi)$, can be recursively defined as

$$N_I^0(\xi) = \begin{cases} 1, & \text{if} \quad \xi_I \leq \xi < \xi_{I+1} \\ 0, & \text{otherwise} \end{cases} \tag{3}$$

$$N_I^p(\xi) = \frac{\xi - \xi_I}{\xi_{I+p} - \xi_I} N_I^{p-1}(\xi) + \frac{\xi_{I+p+1} - \xi}{\xi_{I+p+1} - \xi_{I+1}} N_{I+1}^{p-1}(\xi). \tag{4}$$

B-spline basis functions are C^{p-m}-continuous at knot ξ_I, where m is the multiplicity of ξ_I in Ξ. In the following, we also say a B-spline basis is C^{p-m}-continuous, without specifying the value of m. In this case, it indicates that m can vary at different knots. A univariate quadratic B-spline basis is illustrated in Figure 1b.

Given a knot vector $\Xi = \{\xi_1, \xi_2, \ldots, \xi_{n+p+1}\}$ and a set of C^{p-m}-continuous B-spline basis functions $\left\{N_I^p\right\}_{I=1}^n$, we use the notation $\mathcal{S}_0^p$ to denote a spline space spanned by $\left\{N_I^p\right\}_{I=1}^n$, i.e.,

$$\mathcal{S}_0^p = \text{span}\left\{N_I^p\right\}_{I=1}^n, \tag{5}$$

and we use $\mathcal{S}_k^p$, $k = 1, 2$, to denote a spline space spanned by a set of C^{p-m-k}-continuous B-spline basis functions whose associated knot vector has the same knot intervals as Ξ but with the multiplicity of each interior knot increased by k.

A pth-degree B-spline curve can be written as

$$\mathbf{x}(\xi) = \sum_{I=1}^{n} \mathbf{P}_I N_I^p(\xi), \quad \xi \in [\xi_1, \xi_{n+p+1}]. \tag{6}$$

A pth-degree NURBS curve can be represented as

$$\mathbf{x}(\xi) = \sum_{I=1}^{n} \mathbf{P}_I w_I R_I^p(\xi), \quad \xi \in [\xi_1, \xi_{n+p+1}], \tag{7}$$

where the NURBS basis function R_I^p is defined by

$$R_I^p(\xi) = \frac{N_I^p(\xi)}{W(\xi)}, \tag{8}$$

where $N_I^p(\xi)$ is the Ith p-degree B-spline basis function,

$$W(\xi) = \sum_{I=1}^{n} w_I N_I^p(\xi) \tag{9}$$

is a weighting function, and w_I is the weight corresponding to control point $\mathbf{P}_I$.

Note that unless it is necessary, the superscript p on the basis functions will be dropped hereafter for notation simplicity. Higher-dimensional analogs to these spline concepts can be created using tensor products.

2.2 Greville abscissa

For a degree p B-spline with knot vector Ξ, the Ith Greville abscissa [17] is given by

$$x_I = \frac{1}{p}(\xi_{I+1} + \xi_{I+2} + \cdots + \xi_{I+p}), \quad I = 1 \cdots n. \tag{10}$$

Figure 2 illustrates the Greville abscissae for a univariate quadratic B-spline with knot vector $\Xi = \{0, 0, 0, 1, 2, 3, 4, 4, 4\}$. Note that the number of Greville points is equal to the number of B-spline basis functions and therefore equal to the number of control points. Greville abscissae were originally defined for B-splines, but one can calculate them for NURBS since (10) only depends on the associated basis degree and knot vector.

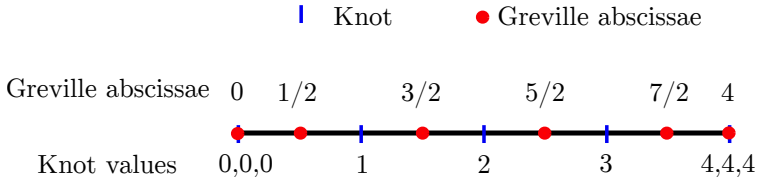

Figure 2: Greville abscissae corresponding to the knot vector $\Xi = \{0, 0, 0, 1, 2, 3, 4, 4, 4\}$.

2.3 Greville quadrature

Numerical integration of a univariate function, $f(x)$, can be written as

$$\int_{\hat{I}} f \mathrm{d}\hat{I} \approx \sum_{I=1}^{n} f(x_I) w_I, \tag{11}$$

where f is the integrand, $\hat{I}$ is the integration domain, $\{x_I\}_{I=1}^n$ are the n quadrature points, and $\{w_I\}_{I=1}^n$ are the corresponding weights. Given a univariate p-degree ($p \geq 2$) B-spline basis $\{N_I\}_{I=1}^n$ with an open knot vector $\Xi = \{\xi_1, \xi_2, \ldots, \xi_{n+p+1}\}$, the Greville quadrature rule [1] chooses the Greville abscissae $\{x_I\}_{I=1}^n$ to be the quadrature points and calculates the weights $\{w_I\}_{I=1}^n$ by

solving the following moment fitting system of equations

$$\begin{bmatrix} \int_{\hat{I}} N_1(\xi)\mathrm{d}\xi \\ \int_{\hat{I}} N_2(\xi)\mathrm{d}\xi \\ \vdots \\ \int_{\hat{I}} N_n(\xi)\mathrm{d}\xi \end{bmatrix} = \begin{bmatrix} N_1(x_1) & N_1(x_2) & \cdots & N_1(x_n) \\ N_2(x_1) & \ddots & \cdots & N_2(x_n) \\ \vdots & & \vdots & \vdots \\ N_n(x_1) & \cdots & \cdots & N_n(x_n) \end{bmatrix} \begin{bmatrix} w_1 \\ w_2 \\ \vdots \\ w_n \end{bmatrix}, \tag{12}$$

where the left-hand side contains the moments [18, 19], which can be calculated analytically [9, 20],

$$\int_{\hat{I}} N_i(\xi)\mathrm{d}\xi = \frac{\xi_{i+p+1} - \xi_i}{p+1}. \tag{13}$$

(12) ensures that the Greville quadrature rule can exactly integrate all linear combinations of the univariate B-spline basis $\{N_I\}_{I=1}^n$. Assume the spline space used for IGA is $\mathcal{S}_0^p$, it is shown in [1] that a spline space $\mathcal{S}_k^p$ has to be used to generate stable and accurate quadrature rules for IGA, where k is the highest order of derivatives in the Galerkin formulation.

Note that Section 2.1 mentioned that the knot vector of $\mathcal{S}_k^p$ is generated by increasing the multiplicities of the interior knots of the knot vector of $\mathcal{S}_0^p$ by k. If the multiplicity of an original interior knot ξ_I is m and $m+k>p$, the generated knot vector will result in an overlapped Greville point at ξ_I, which leads to an ill-conditioned system of (12). To avoid this case, we first divide the original knot vector into different open knot vectors at knots with $m+k>p$, and then build an $\mathcal{S}_k^p$ for each of these divided open knot vectors. Afterward, the new $\mathcal{S}_k^p$'s and their associated knot vectors will be substituted into (12) to produce Greville quadratures on different knot intervals. Note dividing the knot vector is only used to build the Greville quadrature rule and the spline basis used for analysis is not altered.

3 Definition of quadrature rules

This section introduces the proposed reduced Gauss quadrature and the compound Gauss-Greville quadrature rules in a one-dimensional setting. Higher-dimensional quadratures can then be constructed through a tensor product of one-dimensional quadratures.

Let $\{N_I\}_{I=1}^n$ be a degree p B-spline basis with open knot vector $\Xi = \{\xi_1, \ldots, \xi_i, \xi_{i+1}, \ldots, \xi_{n+p+1}\}$, where ξ_i and ξ_{i+1} are two distinct knot values. We call the knot interval $[\xi_i, \xi_{i+1}]$ a Bézier element, or simply an element, and denote it by e.

3.1 Reduced Gauss quadrature

For a Galerkin formulation, where the highest order of derivatives is k, the reduced Gauss quadrature rule on element e involves n Gauss quadrature points, where n has to satisfy the following two requirements:

Requirement 1: $n \geq \lceil (m_i + m_{i+1})/2 \rceil$, where m_i and m_{i+1} are the multiplicities of the knot values ξ_i and ξ_{i+1}, and $\lceil * \rceil$ indicates the smallest integer greater than or equal to the number *.

Requirement 2: The quadrature rule can accurately integrate all functions in the spline space $\mathcal{S}_k^p$ defined in Section 2. As the n-point Gauss quadrature rule is exact for polynomials of degree $2n-1$ or less, this accuracy requirement is satisfied if $(2n-1) \geq p$, i.e. $n \geq \lceil (p+1)/2 \rceil$.

Requirement 1 determines the quadrature point number on the element level according to the regularity of the basis functions. The number of quadrature points is designed to be close to the number of Greville points on each element. For example, for a degree p Bézier element with C^{-1}-continuity (i.e., a degree p B-spline consisting of only one element), the number of quadrature points given by the first requirement is $(p+1)$, which is the same as the number of Greville points. For a maximally smooth Bézier element, the number of quadrature points is one, which also equals the average number of Greville points for a maximally smooth Bézier element within a large mesh. This idea is inspired by our previous work in [21], where numerical examples show that the Greville points can be chosen as the quadrature points, and the resulting stiffness and mass matrices are free of rank deficiency, regardless of the mesh sizes and the polynomial degrees. Unfortunately, even though the matrices are full rank, the system can suffer from spurious modes [21, 16, 7] due to a lack of integration accuracy. Our recent work in [1] shows that accurately integrating the spline basis functions in $\mathcal{S}_k^p$ is necessary to avoid spurious modes, to achieve a well-conditioned system of equations, and to obtain accurate displacement and stress results, which naturally leads to the second requirement here. Combining the two requirements, we obtain an n-point reduced Gauss quadrature rule on element e, where

$$n = \max\left\{\lceil (m_i + m_{i+1})/2 \rceil, \lceil (p+1)/2 \rceil\right\}. \tag{14}$$

Remarks.

1. The reduced Gauss quadrature rule asymptotically involves $(\lceil (p+1)/2 \rceil)^d$ quadrature points per element, where d is the parametric dimension. More specifically, if p is odd, the proposed reduced Gauss quadrature rule asymptotically uses $((p+1)/2)^d$ points per element, which is only $(1/2)^d$ of the number of full Gauss quadrature points; if p is even, this ratio is slightly larger than $(1/2)^d$ as $\lceil (p+1)/2 \rceil = (p+2)/2$. In either case, the reduced Gauss quadrature significantly reduces the number of quadrature points compared to the full Gauss quadrature.

2. If p is even, the order of accuracy of the reduced Gauss quadrature is

$$2n - 1 = 2 \times \lceil (p+1)/2 \rceil - 1 = p + 1, \tag{15}$$

which is one order higher than the required accuracy in Requirement 2. As will be seen later, this leads to the reduced Gauss quadrature rule achieving one order higher convergence rates than the Greville quadrature rule for even-order bases with degrees $p > 2$. For $p = 2$, optimal convergence rates are achieved by both quadrature rules, so there is no difference between the accuracy orders.

Figure 3 illustrates the reduced Gauss quadrature points for a basis degree, $p = 3$, with different knot vectors.

3.2 Gauss-Greville quadrature

Even though the reduced Gauss quadrature uses many fewer quadrature points than the full Gauss quadratures as remarked above, the number of quadrature points increases as the basis degree increases according to (14). The Greville quadrature rule [1], on the other hand, asymptotically uses only two or three quadrature points per element independent of the basis degrees, but it does not guarantee that all quadrature weights are positive. The proposed Gauss-Greville rule combines these two rules so that all quadrature weights are positive and the number of quadrature points is similar to the Greville quadrature rule. Assuming the Greville quadrature rule built with knot vector Ξ has negative quadrature weights on a set of elements, $\{e_i\}_{i \in \text{NEID}}$, where NEID is a set of element indices, the Gauss-Greville rule is then constructed as follows:

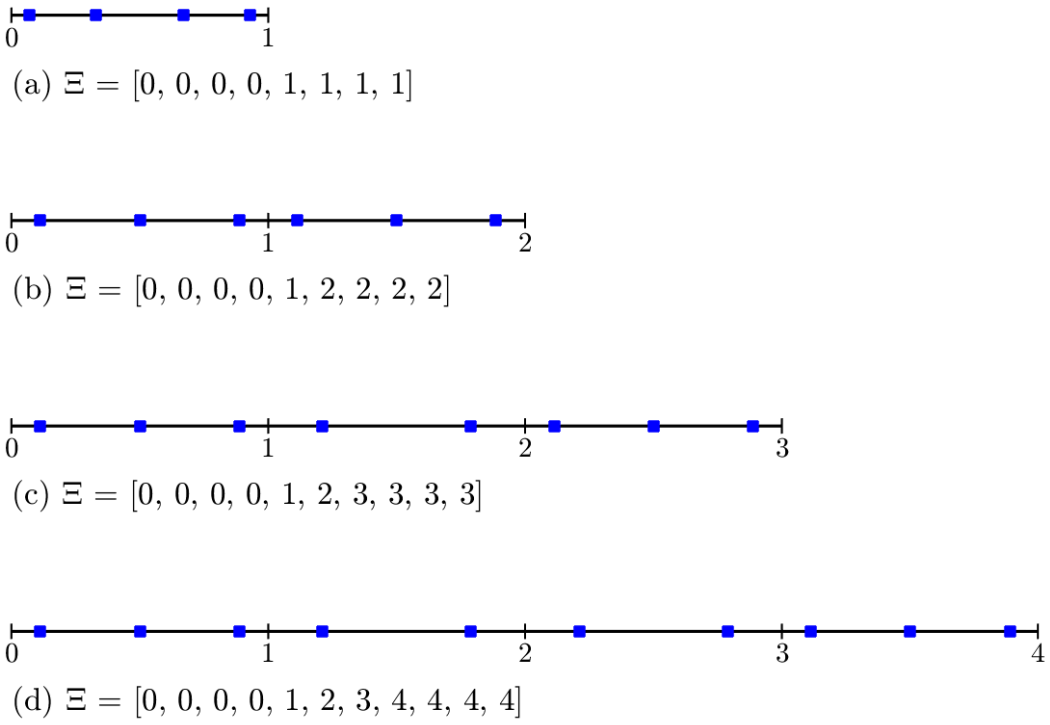

Figure 3: Reduced Gauss quadrature points for $p = 3$, $k = 1$, and various knot vectors. Blue squares indicate the reduced Gauss quadrature points.

Step 1: Replace the quadrature rules on elements $\{e_i\}_{i\in\text{NEID}}$ with the reduced Gauss quadrature proposed previously.

Step 2: Segment the knot vector Ξ into a set of open knot vectors $\{\Xi_i\}_{i=1}^{l}$ by removing the elements in $\{e_i\}_{i\in\text{NEID}}$. For instance, if only one element, e, corresponding to a knot interval $[\xi_i, \xi_{i+1}]$, has negative quadrature weights, then Ξ will be segmented into two open knot vectors as follows by removing the knot interval $[\xi_i, \xi_{i+1}]$ and adding repeated end knots,

$$\Xi_1 = \{\xi_1, \xi_2, \ldots, \underbrace{\xi_i, \ldots, \xi_i}_{p+1}\} \quad \text{and} \quad \Xi_2 = \{\underbrace{\xi_{i+1}, \ldots, \xi_{i+1}}_{p+1}, \ldots, \xi_{n+p+1}\}. \tag{16}$$

Step 3: Build Greville quadrature rule on each knot vector in $\{\Xi_i\}_{i=1}^{l}$.

Step 4: Check if all Greville quadrature weights associated with each Ξ_i are positive. If negative weights occur on some Ξ_i's, repeat Steps 1 to 3 with these Ξ_i's until all quadrature weights are positive.

Remarks.

1. In Step 1, if a Greville quadrature point on the interface of two adjacent elements has negative weight, the quadrature rules on these two elements are replaced with the reduced Gauss quadrature rules.

2. If a segmented knot vector Ξ_i generated in Step 2 includes only one element, the Greville quadrature rule built on this element will require $(p + 1)$ quadrature points, which is the same number as the full Gauss quadrature rule. To reduce the total number of quadrature points, one can first check the number of elements associated with Ξ_i before getting into Step 3 and constructing the Greville quadrature rule on Ξ_i. If the element number associated with Ξ_i is less than a user-defined number, then the reduced Gauss quadrature rules should be used directly on these elements instead of constructing the Greville quadrature rule. Besides helping to reduce the number of quadrature points, the user-defined number also gives users more control of the Gauss-Greville quadrature rule. For instance, if a huge number is given, e.g., a number greater than the total number of elements, Greville quadrature rules will never be built on any knot segment Ξ_i and the Gauss-Greville quadrature rule will degenerate to the reduced Gauss quadrature rule automatically.

3. Greville quadrature rule built on each segmented knot vector Ξ_i in Step 3 usually does not include negative weights. The authors only observed negative weights after Step 3 for a few cases of all tests considered, and repeating Steps 1 to 3 once eliminates all negative weights.

Algorithm 1 outlines the construction of the Gauss-Greville quadrature rule, in which the following subroutines are used:

- elemNum(EID) returns the number of elements for a given element index set, EID.
- getElemWithNegWgt($\{W_i\}_{i\in\text{EID}}$, EID) gets the indices of elements with negative Greville quadrature weights for a given set of Greville quadrature weights $\{W_i\}_{i\in\text{EID}}$, where W_i refers to the Greville quadrature weights on the ith global element.
- segmentKnotVector(Ξ, EID, NEID) segments a given knot vector Ξ into a set of open knot vectors $\{\Xi_i\}_{i=1}^{l}$ by removing elements $\{e_i\}_{i\in\text{NEID}}$ as described in Step 2 above. Here EID is a set of global element indices corresponding to the knot intervals of Ξ, and NEID $\subseteq$ EID is obtained from the function, getElemWithNegWgt, introduced above.

- BUILDREDUCEDGAUSS(NEID, $\mathcal{M}$, p) builds the reduced Gauss quadrature rule for each element e_i, $i \in$ NEID, according to (14), where the multiplicities m_i and m_{i+1} of the two associated element knots are obtained from the multiplicity vector $\mathcal{M}$ of distinct knots of the *original* knot vector.

- BUILDGREVILLEQUADRATURE(Ξ, p, k) builds the Greville quadrature for a given knot vector Ξ. For details, see Section 2.3 or [1].

The above subroutines are easy to program and omitted in this work for conciseness.

Algorithm 1 Computing the Gauss-Greville quadrature points $\{Q_i\}_{i\in\text{EID}}$ and weights $\{W_i\}_{i\in\text{EID}}$, where Q_i and W_i are vectors of quadrature points and weights of the ith global element.

Inputs: Knot vector Ξ; global element index set EID; multiplicity vector $\mathcal{M}$ of distinct knots of the *original* knot vector; basis degree p; the highest derivative order, k, in the Galerkin formulation; the minimal number of consecutive elements, n_{con}, to build the Greville quadrature rule.
Outputs: $\{Q_i\}_{i\in\text{EID}}$, $\{W_i\}_{i\in\text{EID}}$.

procedure BUILDGAUSSGREVILLE(Ξ, EID, $\mathcal{M}$, p, k, n_{con});
  $n_{\mathsf{el}} \leftarrow$ ELEMNUM(Ξ); ▷ Get the number of elements associated with Ξ.
  if $n_{\mathsf{el}} < n_{\mathsf{con}}$ **then**
    // Build reduced Gauss quadratures on all elements associated with the given knot vector Ξ.
    $[\{Q_i\}_{i\in\text{EID}}, \{W_i\}_{i\in\text{EID}}] \leftarrow$ BUILDREDUCEDGAUSS(EID, $\mathcal{M}$, p);
    return $[\{Q_i\}_{i\in\text{EID}}, \{W_i\}_{i\in\text{EID}}]$;
  else
    // Initialize Quadrature points and weights with Greville quadrature.
    $[\{Q_i\}_{i\in\text{EID}}, \{W_i\}_{i\in\text{EID}}] \leftarrow$ BUILDGREVILLEQUADRATURE(Ξ, p, k);
    // Sort out elements with negative Greville quadrature weights.
    NEID $\leftarrow$GETELEMWITHNEGWGT($\{W_i\}_{i\in\text{EID}}$, EID); ▷ NEID is a set of element indices.
    if NEID $\neq \emptyset$ **then** ▷ There exist elements with negative Greville quadrature weights.
      // Build reduced Gauss quadratures on elements with negative Greville quadrature weights.
      $[\{Q_i\}_{i\in\text{NEID}}, \{W_i\}_{i\in\text{NEID}}] \leftarrow$ BUILDREDUCEDGAUSS(NEID, $\mathcal{M}$, p);
      // Segment Ξ as explained in Step 2.
      // I_i is a set of global element indices corresponding to the knot intervals of Ξ_i.
      $[\{\Xi_i\}_{i=1}^{l}, \{\mathsf{I}_i\}_{i=1}^{l}] \leftarrow$ SEGMENTKNOTVECTOR(Ξ, EID, NEID);
      // Loop through each knot segment Ξ_i to build Gauss-Greville quadrature.
      for $i = 1, \ldots, l$ **do**
        if ELEMNUM(Ξ_i) $< n_{\text{con}}$ **then**
          $[\{Q_j\}_{j\in\mathsf{I}_i}, \{W_j\}_{j\in\mathsf{I}_i}] \leftarrow$ BUILDREDUCEDGAUSS(I_i, $\mathcal{M}$, p);
        else
          $[\{Q_j\}_{j\in\mathsf{I}_i}, \{W_j\}_{j\in\mathsf{I}_i}] \leftarrow$ BUILDGAUSSGREVILLE(Ξ_i, I_i, $\mathcal{M}$, p, k, n_{con});
        end if
      end for
    end if
    return $[\{Q_i\}_{i\in\text{EID}}, \{W_i\}_{i\in\text{EID}}]$;
  end if
end procedure

Figure 4 compares the distribution of Greville quadrature points and Gauss-Greville quadrature points for a quartic basis with knot vector $\Xi = [0, 0, 0, 0, 0, 1, 11, 16, 21, 26, 26, 26, 26, 26]$ and $k = 1$.

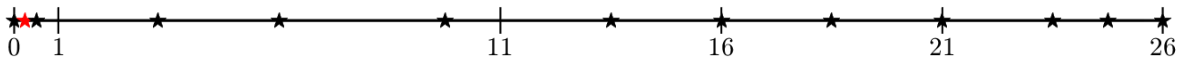

(a) Greville quadrature points.

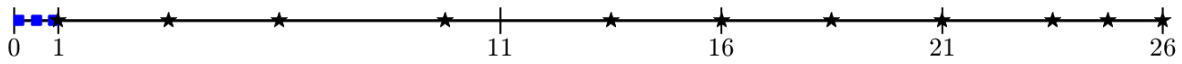

(b) Gauss-Greville quadrature points.

Figure 4: Greville and Gauss-Greville quadrature points for knot vector $\Xi = [0, 0, 0, 0, 0, 1, 11, 16, 21, 26, 26, 26, 26, 26]$, $p = 4$ and $k = 1$. Red stars indicate Greville points with *negative* weights; black stars indicate Greville points with *positive* weights; blue squares indicate reduced Gauss quadrature points.

It can be seen that the number of Gauss-Greville quadrature points is only one more than that of the Greville quadrature points. Table 1 gives the corresponding element quadrature points and weights with respect to the parent element domain $[-1, 1]$.

Table 1: Greville and Gauss-Greville quadrature points and weights, with respect to the parent element domain $[-1, 1]$, for the example in Figure 4.

element index	Greville		Gauss-Greville	
	point	weight	point	weight
1	-1.00000000000000	0.57267792549465	-0.77459666924148	0.55555555555556
	-0.50000000000000	-1.29269535049313	0.00000000000000	0.88888888888889
	0.00000000000000	3.78142340395716	0.77459666924148	0.55555555555556
2	-0.55000000000000	0.66119438134739	-1.00000000000000	0.17005188208617
	0.00000000000000	0.55405465377474	-0.50000000000000	0.62188901587302
	0.75000000000000	0.83875617981115	0.00000000000000	0.52757248677249
			0.75000000000000	0.84076978987150
3	0.00000000000000	1.26236897462701	0.00000000000000	1.26199873015873
4	-1.00000000000000	0.87016791228626	-1.00000000000000	0.87029841269841
	0.00000000000000	1.07309370605694	0.00000000000000	1.07304634920635
5	-1.00000000000000	0.97994352360960	-1.00000000000000	0.97996105820106
	0.00000000000000	0.83767825805710	0.00000000000000	0.83766857142857
	0.50000000000000	0.45174621744764	0.50000000000000	0.45175195767196
	1.00000000000000	0.20470978225714	1.00000000000000	0.20470857142857

4 Stability and accuracy

In this section, we demonstrate the stability and accuracy of the proposed reduced Gauss quadrature and Gauss-Greville quadrature rules through eigenvalue problems.

4.1 Laplace problem

We first consider the Laplace eigenvalue problem

$$-\Delta u = \lambda u \quad \text{in } \Omega, \tag{17a}$$

$$\nabla u \cdot \mathbf{n} = 0 \quad \text{on } \partial\Omega, \tag{17b}$$

where u is the eigenfunction, λ is the corresponding eigenvalue and $\mathbf{n}$ is the outward normal unit vector of the domain boundary $\partial\Omega$. This is a Neumann eigenvalue problem [22]. Its Galerkin variational formulation can be written as

$$\int_\Omega \nabla u^h \cdot \nabla v^h \,\mathrm{d}\Omega = \lambda \int_\Omega u^h v^h \,\mathrm{d}\Omega, \quad \forall v^h \in \mathcal{V}^h, \tag{18}$$

where, in the context of IGA, u^h and v^h are the discretized trial and test functions in terms of spline basis functions. The matrix form can be written as

$$(\mathbf{K} - \lambda \mathbf{M})\mathbf{\Psi} = \mathbf{0}, \tag{19}$$

where $\mathbf{K}$ and $\mathbf{M}$ are the stiffness and mass matrices, whose components can be calculated by

$$K_{IJ} = \int_\Omega \nabla N_I \nabla N_J \,\mathrm{d}\Omega, \tag{20}$$

$$M_{IJ} = \int_\Omega N_I N_J \,\mathrm{d}\Omega. \tag{21}$$

We demonstrate the stability and accuracy of the proposed quadratures through examining the eigenvalue problem (17) over a square domain $\Omega = (0, 2) \times (0, 2)$. The analytical solution is

$$u_j = \cos \frac{j_1 \pi}{2} x \cos \frac{j_2 \pi}{2} y, \tag{22}$$

$$\lambda_j = \frac{\pi^2}{4} \left(j_1^2 + j_2^2 \right), \tag{23}$$

where $j = (j_1, j_2)$ is an arbitrary pair of natural numbers, i.e., $j_1, j_2 \in \mathbb{N}$. According to the finite element error estimates [23, 24], the relative error of the jth approximate eigenvalue, λ_j^h, is bounded as

$$\frac{\lambda_j^h - \lambda_j}{\lambda_j} \leq c \left(h \lambda_j^{1/(2k)} \right)^{2(p+1-k)}, \tag{24}$$

where λ_j is the jth analytical eigenvalue, h is the mesh size, c is a constant independent of h and λ_j, and k is the order of derivatives in the weak form, which is 1 in the case of 18.

Numerical results verify that all three quadrature rules, i.e., full Gauss, reduced Gauss and Gauss-Greville quadrature rules, capture the unique zero eigenvalue for all mesh sizes and degrees considered, $p = 2$ to 6. Additionally, Figure 5 illustrates the convergence behavior of the three smallest non-zero and distinct eigenvalues for three quadrature rules with various basis degrees and uniform meshes. For $p = 2$, optimal convergence rates are observed for all three quadrature rules; for $p = 3$, full Gauss quadrature rule achieves optimal rates equal to 6, while the proposed reduced Gauss and Gauss-Greville quadrature rules obtain suboptimal convergence rates equal to 4; for higher-order bases, the relative errors for full Gauss quadrature rule reach machine precision quickly and therefore convergence rates are not clearly observed, but, for the proposed quadrature rules, a suboptimal convergence rate of 6 can still be seen for $p = 4$ and 5.

We note that for second-order PDEs, the Greville quadratures [1] do not involve negative quadrature weights with maximally smooth and uniform meshes. As a result, in this case the proposed Gauss-Greville rule is the same as the Greville quadrature rule [1]. To distinguish the proposed Gauss-Greville quadrature rule from the existing Greville quadrature rule, we also consider non-uniform meshes as shown in Figure 6a. For the Greville quadrature rule, negative Greville quadrature weights will occur with this initial mesh and its uniformly refinements, such as Figures 6b and c, etc. As can be seen in Figure 7, the convergence behavior for all three quadrature rules is basically consistent with what we observed above for the uniform mesh cases.

Tables 2 to 4 list the 50 smallest non-zero eigenvalues of the Laplace problem for $p = 2$ to 4, 32×32 elements and non-uniform meshes. It can be seen that the eigenvalues produced by the reduced Gauss and Gauss-Greville quadrature schemes are very close to those obtained from full Gauss quadrature, which shows that the proposed quadrature rules are free of spurious modes [16, 21, 7]. For higher p the accuracy gets even better and the results are omitted here.

Note in this benchmark and what follows, when studying the Gauss-Greville quadrature rule, we set the input variable n_{cons}, given in Algorithm 1, to be 1, to prevent the Gauss-Greville quadrature rule from degenerating to the reduced Gauss quadrature rule with very coarse meshes.

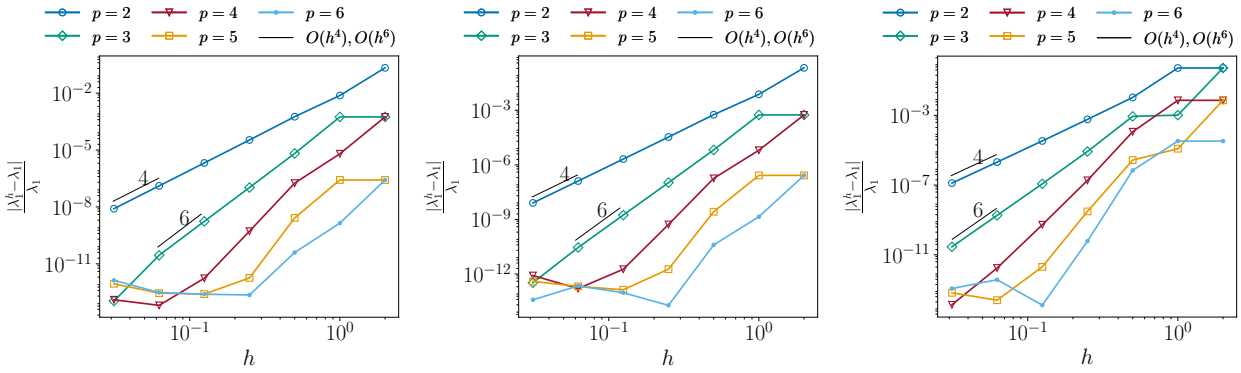

(a) Full Gauss, λ_1. (b) Full Gauss, λ_3. (c) Full Gauss, λ_4.

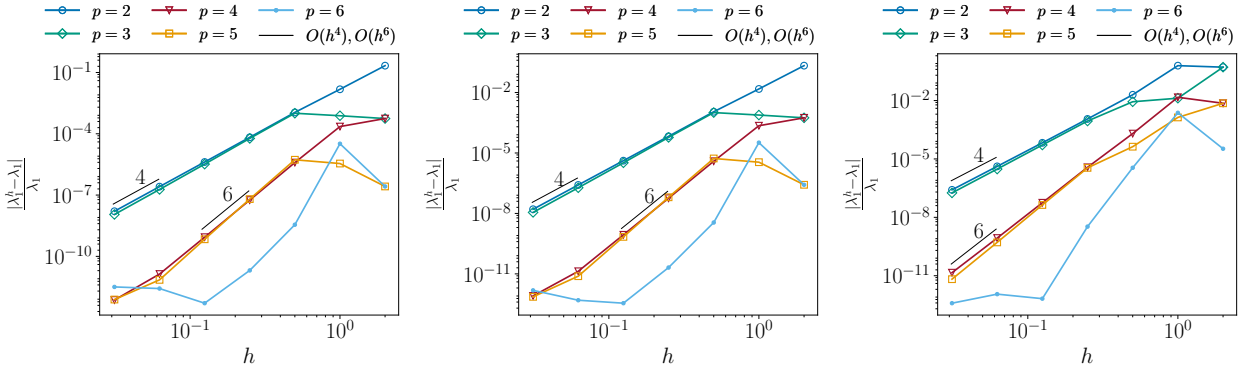

(d) Reduced Gauss, λ_1. (e) Reduced Gauss, λ_3. (f) Reduced Gauss, λ_4.

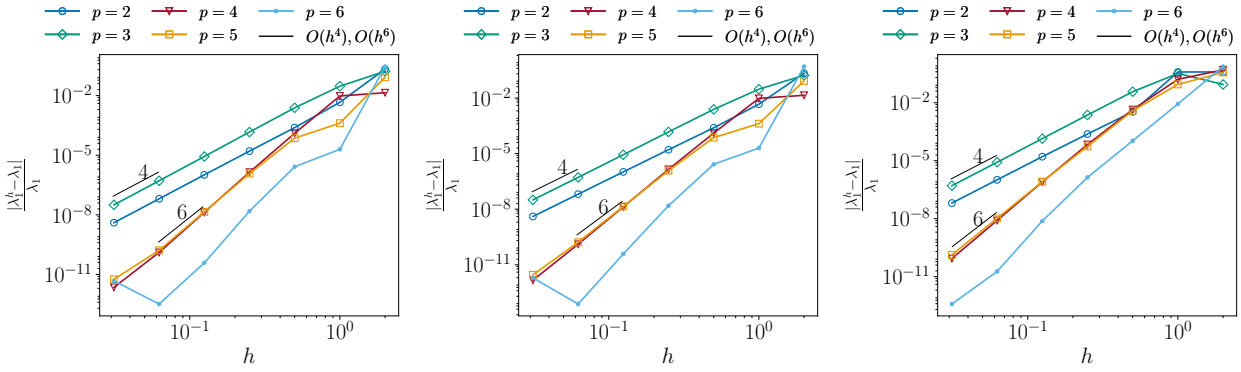

(g) Gauss-Greville, λ_1. (h) Gauss-Greville, λ_3. (i) Gauss-Greville, λ_4.

Figure 5: Laplace eigenvalue problem on $(0, 2) \times (0, 2)$: Convergence of the relative error of the three smallest non-zero and distinct eigenvalues, λ_1, λ_3 and λ_4, for $p = 2$ to 6, full Gauss, reduced Gauss and Gauss-Greville quadratures, and *uniform* meshes.

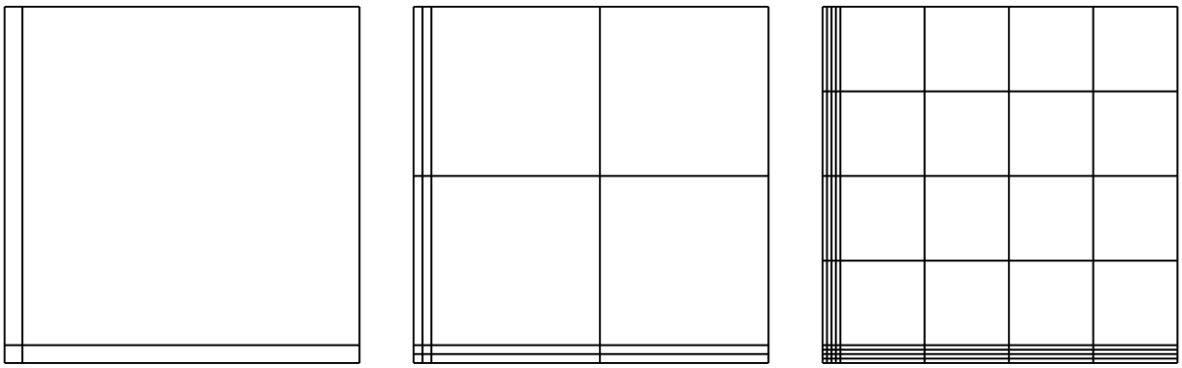

(a) Initial mesh. (b) Refine once. (c) Refine twice.

Figure 6: Laplace eigenvalue problem on $(0,2) \times (0,2)$: initial non-uniform mesh and its uniform refinements.

Table 2: The 50 smallest non-zero eigenvalues for the Laplace problem with full Gauss quadrature (GA), reduced Gauss quadrature (RGA) and Gauss-Greville quadrature (GA-GR), $p = 2$, 32×32 maximally smooth elements, and *non-uniform* meshes.

j	GA	RGA/GA	GA-GR/GA	j	GA	RGA/GA	GA-GR/GA
1	2.46741e+00	1.00000	1.00000	26	6.42271e+01	1.00099	0.99852
2	2.46741e+00	1.00000	1.00000	27	6.42271e+01	1.00099	0.99852
3	4.93481e+00	1.00000	1.00000	28	7.16296e+01	1.00089	0.99867
4	9.86988e+00	1.00002	0.99996	29	7.16296e+01	1.00089	0.99867
5	9.86988e+00	1.00002	0.99996	30	7.89941e+01	1.00041	0.99939
6	1.23373e+01	1.00002	0.99997	31	8.39695e+01	1.00079	0.99882
7	1.23373e+01	1.00002	0.99997	32	8.39695e+01	1.00079	0.99882
8	1.97398e+01	1.00002	0.99996	33	8.90635e+01	1.00221	0.99670
9	2.22098e+01	1.00013	0.99981	34	8.90635e+01	1.00221	0.99670
10	2.22098e+01	1.00013	0.99981	35	9.15309e+01	1.00215	0.99679
11	2.46772e+01	1.00011	0.99983	36	9.15309e+01	1.00215	0.99679
12	2.46772e+01	1.00011	0.99983	37	9.89334e+01	1.00199	0.99702
13	3.20797e+01	1.00009	0.99986	38	9.89334e+01	1.00199	0.99702
14	3.20797e+01	1.00009	0.99986	39	1.01257e+02	1.00078	0.99882
15	3.94970e+01	1.00041	0.99939	40	1.01257e+02	1.00078	0.99882
16	3.94970e+01	1.00041	0.99939	41	1.11273e+02	1.00179	0.99732
17	4.19644e+01	1.00038	0.99942	42	1.11273e+02	1.00179	0.99732
18	4.19644e+01	1.00038	0.99942	43	1.21543e+02	1.00428	0.99363
19	4.44196e+01	1.00013	0.99981	44	1.21543e+02	1.00428	0.99363
20	4.93669e+01	1.00033	0.99950	45	1.23519e+02	1.00103	0.99771
21	4.93669e+01	1.00033	0.99950	46	1.24011e+02	1.00419	0.99375
22	6.17068e+01	1.00031	0.99932	47	1.24011e+02	1.00419	0.99451
23	6.17068e+01	1.00031	0.99932	48	1.28561e+02	1.00165	0.99752
24	6.17597e+01	1.00103	0.99868	49	1.28561e+02	1.00165	0.99752
25	6.17597e+01	1.00103	0.99868	50	1.31413e+02	1.00396	0.99410

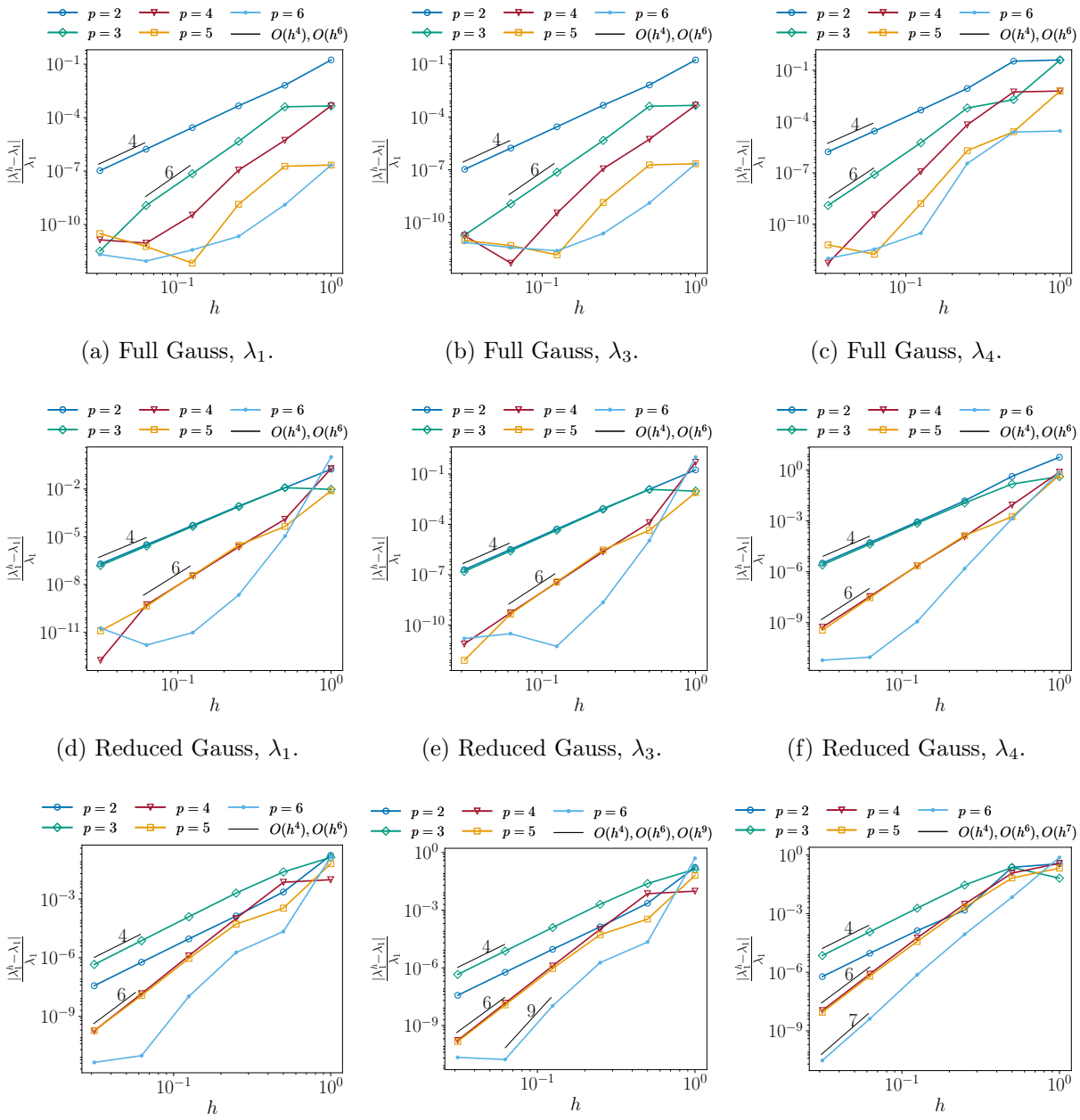

(a) Full Gauss, λ_1.

(b) Full Gauss, λ_3.

(c) Full Gauss, λ_4.

(d) Reduced Gauss, λ_1.

(e) Reduced Gauss, λ_3.

(f) Reduced Gauss, λ_4.

(g) Gauss-Greville, λ_1.

(h) Gauss-Greville, λ_3.

(i) Gauss-Greville, λ_4.

Figure 7: Laplace eigenvalue problem on $(0, 2) \times (0, 2)$: Convergence of the relative error of the three smallest and distinct eigenvalues, λ_1, λ_3 and λ_4, for $p = 2$ to 6, full Gauss, reduced Gauss and Gauss-Greville quadratures, and *non-uniform* meshes.

Table 3: The 50 smallest non-zero eigenvalues for the Laplace problem with full Gauss quadrature (GA), reduced Gauss quadrature (RGA) and Gauss-Greville quadrature (GA-GR), $p = 3$, 32×32 maximally smooth elements, and *non-uniform* meshes.

j	GA	RGA/GA	GA-GR/GA	j	GA	RGA/GA	GA-GR/GA
1	2.46740e+00	1.00000	1.00001	26	6.41542e+01	0.99836	1.00416
2	2.46740e+00	1.00000	1.00001	27	6.41542e+01	0.99836	1.00416
3	4.93480e+00	1.00000	1.00001	28	7.15564e+01	0.99853	1.00375
4	9.86961e+00	0.99996	1.00012	29	7.15564e+01	0.99853	1.00375
5	9.86961e+00	0.99996	1.00012	30	7.89573e+01	0.99931	1.00178
6	1.23370e+01	0.99997	1.00009	31	8.38934e+01	0.99869	1.00333
7	1.23370e+01	0.99997	1.00009	32	8.38934e+01	0.99869	1.00333
8	1.97392e+01	0.99996	1.00012	33	8.88352e+01	0.99639	1.00907
9	2.22066e+01	0.99979	1.00058	34	8.88352e+01	0.99639	1.00907
10	2.22066e+01	0.99979	1.00058	35	9.13026e+01	0.99649	1.00882
11	2.46740e+01	0.99981	1.00052	36	9.13026e+01	0.99649	1.00882
12	2.46740e+01	0.99981	1.00052	37	9.87048e+01	0.99675	1.00817
13	3.20762e+01	0.99984	1.00043	38	9.87048e+01	0.99675	1.00817
14	3.20762e+01	0.99984	1.00043	39	1.01165e+02	0.99869	1.00333
15	3.94787e+01	0.99931	1.00178	40	1.01165e+02	0.99869	1.00333
16	3.94787e+01	0.99931	1.00178	41	1.11042e+02	0.99707	1.00737
17	4.19461e+01	0.99935	1.00168	42	1.11042e+02	0.99707	1.00737
18	4.19461e+01	0.99935	1.00168	43	1.20938e+02	0.99313	1.01728
19	4.44133e+01	0.99979	1.00058	44	1.20938e+02	0.99313	1.01728
20	4.93483e+01	0.99944	1.00145	45	1.23374e+02	0.99352	1.00433
21	4.93483e+01	0.99944	1.00145	46	1.23406e+02	0.99326	1.01694
22	6.16853e+01	0.99832	1.00135	47	1.23406e+02	0.99804	1.01694
23	6.16853e+01	0.99832	1.00135	48	1.28314e+02	0.99729	1.00683
24	6.16868e+01	0.99946	1.00433	49	1.28314e+02	0.99729	1.00683
25	6.16868e+01	0.99946	1.00433	50	1.30808e+02	0.99364	1.01599

Table 4: The 50 smallest non-zero eigenvalues for the Laplace problem with full Gauss quadrature (GA), reduced Gauss quadrature (RGA) and Gauss-Greville quadrature (GA-GR), $p = 4$, 32×32 maximally smooth elements, and *non-uniform* meshes.

j	GA	RGA/GA	GA-GR/GA	j	GA	RGA/GA	GA-GR/GA
1	2.46740e+00	1.00000	1.00000	26	6.41525e+01	0.99999	0.99991
2	2.46740e+00	1.00000	1.00000	27	6.41525e+01	0.99999	0.99991
3	4.93480e+00	1.00000	1.00000	28	7.15547e+01	0.99999	0.99992
4	9.86960e+00	1.00000	1.00000	29	7.15547e+01	0.99999	0.99992
5	9.86960e+00	1.00000	1.00000	30	7.89568e+01	1.00000	0.99997
6	1.23370e+01	1.00000	1.00000	31	8.38917e+01	0.99999	0.99993
7	1.23370e+01	1.00000	1.00000	32	8.38917e+01	0.99999	0.99993
8	1.97392e+01	1.00000	1.00000	33	8.88268e+01	0.99997	0.99978
9	2.22066e+01	1.00000	0.99999	34	8.88268e+01	0.99997	0.99978
10	2.22066e+01	1.00000	0.99999	35	9.12942e+01	0.99997	0.99979
11	2.46740e+01	1.00000	0.99999	36	9.12942e+01	0.99997	0.99979
12	2.46740e+01	1.00000	0.99999	37	9.86964e+01	0.99997	0.99980
13	3.20762e+01	1.00000	0.99999	38	9.86964e+01	0.99997	0.99980
14	3.20762e+01	1.00000	0.99999	39	1.01164e+02	0.99999	0.99993
15	3.94784e+01	1.00000	0.99997	40	1.01164e+02	0.99999	0.99993
16	3.94784e+01	1.00000	0.99997	41	1.11033e+02	0.99998	0.99982
17	4.19458e+01	1.00000	0.99997	42	1.11033e+02	0.99998	0.99982
18	4.19458e+01	1.00000	0.99997	43	1.20905e+02	0.99992	0.99956
19	4.44132e+01	1.00000	0.99999	44	1.20905e+02	0.99992	0.99956
20	4.93480e+01	1.00000	0.99997	45	1.23370e+02	0.99994	0.99959
21	4.93480e+01	1.00000	0.99997	46	1.23372e+02	0.99992	0.99957
22	6.16850e+01	0.99999	0.99991	47	1.23372e+02	0.99997	0.99989
23	6.16850e+01	0.99999	0.99991	48	1.28305e+02	0.99998	0.99984
24	6.16851e+01	1.00000	0.99998	49	1.28305e+02	0.99998	0.99984
25	6.16851e+01	1.00000	0.99998	50	1.30775e+02	0.99992	0.99959

4.2 Bending of a Kirchhoff plate

To explore the stability and accuracy of the proposed quadrature rules for higher-order PDEs, we also consider the eigenvalue problem for the bending problem of a Kirchhoff plate [1]. The matrix form has the same format as (19) but with different stiffness and mass matrix components

$$K_{IJ} = \int_\Omega \mathbf{B}_I \mathbf{D} \mathbf{B}_J \mathrm{d}\Omega, \tag{25}$$

$$M_{IJ} = t \int_\Omega \rho N_I N_J \, \mathrm{d}\Omega, \tag{26}$$

where t is the plate thickness, ρ is the mass density,

$$\mathbf{D} = \frac{Et^3}{12(1-\nu^2)} \begin{bmatrix} 1 & \nu & 0 \\ \nu & 1 & 0 \\ 0 & 0 & \frac{1-\nu}{2} \end{bmatrix} \quad \text{and} \quad \mathbf{B}_I = - \begin{bmatrix} \frac{\partial^2 N_I}{\partial x^2} \\ \frac{\partial^2 N_I}{\partial y^2} \\ 2\frac{\partial^2 N_I}{\partial x \partial y} \end{bmatrix} \tag{27}$$

are the elasticity and strain-displacement matrices, E is Young's modulus and ν is Poisson's ratio.

We examine the eigenvalue problem for a square elastic plate with Young's modulus $E = 1000$, Poisson's ratio $\nu = 0$, mass density $\rho = 1000$, thickness $t = 0.1$, and edge length $L = 10$. Without prescribing any Dirichlet boundary conditions, the stiffness matrix $\mathbf{K}$ and the mass matrix $\mathbf{M}$ should be positive semi-definite and positive definite, respectively. The resulting eigenvalues should be non-negative real numbers, and three of them should be zeros corresponding to the three out-of-plane rigid body modes [1].

Numerical results with the proposed reduced Gauss and Gauss-Greville quadratures demonstrate that the resulting stiffness matrices have the correct rank deficiency 3 for all mesh sizes and degrees considered, $p = 2$ to 6. Figure 8 shows the convergence of the relative errors of the three smallest non-zero eigenvalues. The three reference eigenvalues in Table 5 are obtained from [1], which are calculated with a very fine mesh and full Gauss quadrature rule. It can be seen that, similar to full Gauss quadrature, both reduced Gauss and Gauss-Greville quadrature rules obtain optimal convergence rates for $p = 2$ and 3. For $p > 3$, the convergence rates are not optimal but they are greater than 4 before the differences between λ_j^h and λ_j decrease to 10^{-12}.

Tables 6 to 8 list the 50 smallest non-zero eigenvalues corresponding to the bending modes for $p = 2$ to 4, 32×32 maximally smooth elements. Again, the eigenvalues produced by the proposed quadrature schemes are very close to those obtained from full Gauss quadrature and the accuracy improves as the basis degrees increase. Note that for this problem only uniform meshes are used as they generate negative Greville quadrature weights for higher-order problems [1].

Table 5: Reference eigenvalues for the bending of a square elastic plate [1].

λ_1	λ_2	λ_3
2.0862971829e-05	4.1713658653e-05	4.1713659232e-05

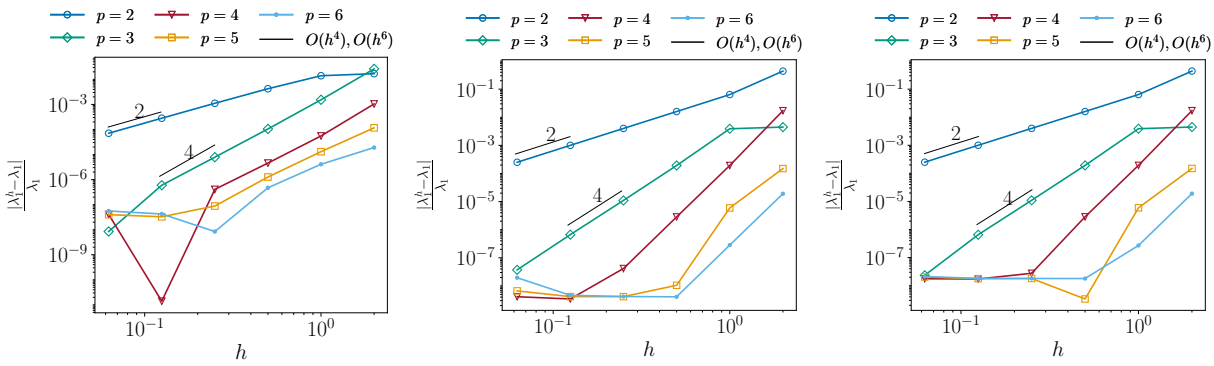

(a) Full Gauss, λ_1. (b) Full Gauss, λ_2. (c) Full Gauss, λ_3.

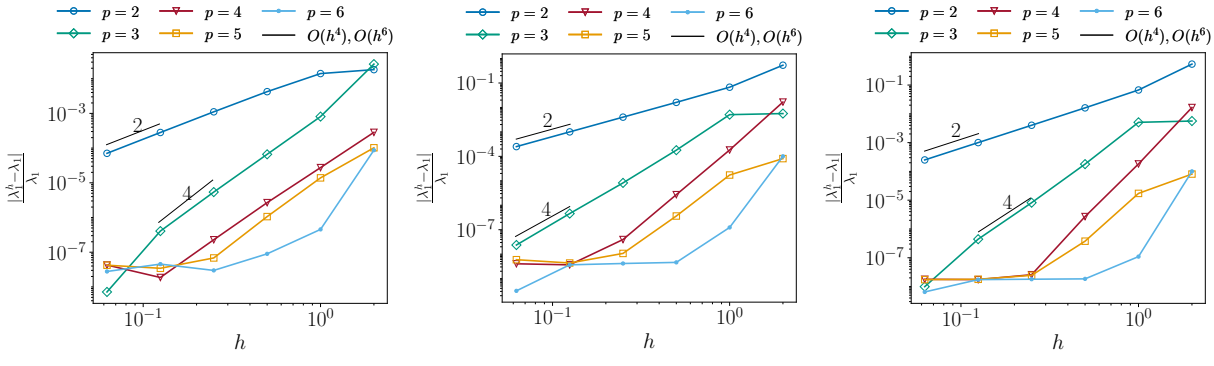

(d) Reduced Gauss, λ_1. (e) Reduced Gauss, λ_2. (f) Reduced Gauss, λ_3.

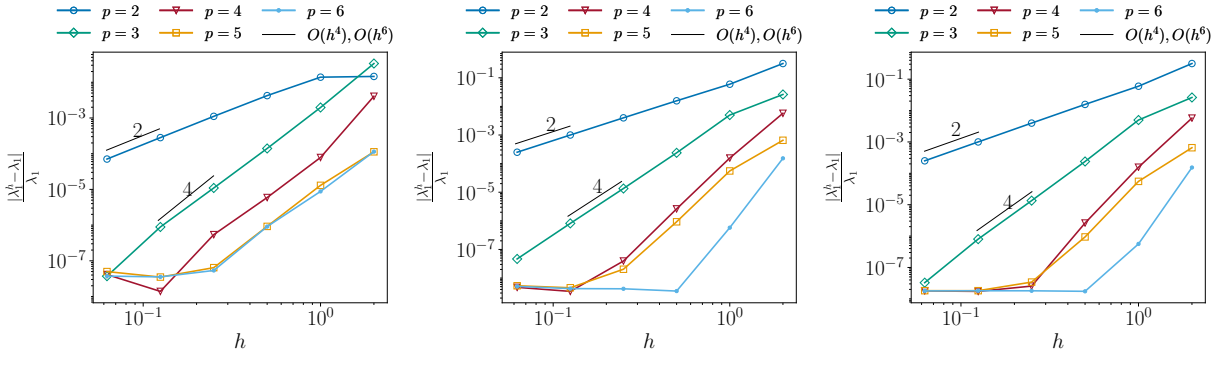

(g) Gauss-Greville, λ_1. (h) Gauss-Greville, λ_2. (i) Gauss-Greville, λ_3.

Figure 8: Bending of Kirchhoff plate: Convergence of the relative error of the three smallest non-zero eigenvalues, λ_1, λ_2 and λ_3, for $p = 2$ to 6, full Gauss, reduced Gauss and Gauss-Greville quadratures, and *uniform* meshes.

Table 6: The 50 smallest non-zero eigenvalues corresponding to the bending modes for full Gauss quadrature (GA), reduced Gauss quadrature (RGA) and Gauss-Greville quadrature (GA-GR), $p = 2$, 32×32 maximally smooth elements, and *uniform* meshes.

j	GA	RGA/GA	GA-GR/GA	j	GA	RGA/GA	GA-GR/GA
1	2.08861e-05	1.00000	1.00000	26	5.50374e-03	1.00089	0.99866
2	4.18805e-05	1.00001	0.99998	27	5.50374e-03	1.00089	0.99866
3	4.18805e-05	1.00001	0.99998	28	7.55163e-03	1.00060	0.99909
4	1.25162e-04	1.00001	0.99998	29	8.09529e-03	1.00206	0.99692
5	1.25162e-04	1.00001	0.99998	30	8.09529e-03	1.00206	0.99692
6	3.21733e-04	1.00008	0.99988	31	8.19785e-03	1.00094	0.99859
7	3.21733e-04	1.00008	0.99988	32	8.26421e-03	1.00094	0.99860
8	4.15300e-04	1.00002	0.99996	33	8.77268e-03	1.00206	0.99692
9	5.02597e-04	1.00008	0.99988	34	8.77268e-03	1.00206	0.99692
10	5.07066e-04	1.00008	0.99988	35	1.08714e-02	1.00206	0.99693
11	1.09748e-03	1.00009	0.99986	36	1.08906e-02	1.00205	0.99694
12	1.09748e-03	1.00009	0.99986	37	1.25565e-02	1.00113	0.99831
13	1.25789e-03	1.00032	0.99952	38	1.25565e-02	1.00113	0.99831
14	1.25789e-03	1.00032	0.99952	39	1.46387e-02	1.00207	0.99691
15	1.57251e-03	1.00032	0.99952	40	1.46387e-02	1.00207	0.99691
16	1.57251e-03	1.00032	0.99952	41	1.63862e-02	1.00418	0.99379
17	2.27835e-03	1.00017	0.99975	42	1.63862e-02	1.00418	0.99379
18	2.55933e-03	1.00033	0.99951	43	1.72959e-02	1.00418	0.99379
19	2.58483e-03	1.00032	0.99951	44	1.72971e-02	1.00418	0.99379
20	3.51962e-03	1.00090	0.99866	45	1.91178e-02	1.00161	0.99759
21	3.51962e-03	1.00090	0.99866	46	2.01099e-02	1.00417	0.99381
22	3.99764e-03	1.00090	0.99866	47	2.01099e-02	1.00417	0.99381
23	3.99985e-03	1.00089	0.99866	48	2.03619e-02	1.00222	0.99669
24	4.43807e-03	1.00039	0.99941	49	2.04940e-02	1.00221	0.99670
25	4.43807e-03	1.00039	0.99941	50	2.50337e-02	1.00416	0.99382

Table 7: The 50 smallest non-zero eigenvalues corresponding to the bending modes for full Gauss quadrature (GA), reduced Gauss quadrature (RGA) and Gauss-Greville quadrature (GA-GR), $p = 3$, 32×32 maximally smooth elements, and *uniform* meshes.

j	GA	RGA/GA	GA-GR/GA	j	GA	RGA/GA	GA-GR/GA
1	2.08631e-05	1.00000	1.00000	26	5.29308e-03	0.99948	1.00042
2	4.17141e-05	1.00000	1.00000	27	5.29308e-03	0.99948	1.00042
3	4.17141e-05	1.00000	1.00000	28	7.39657e-03	0.99919	1.00050
4	1.24774e-04	0.99999	1.00001	29	7.44660e-03	0.99954	1.00060
5	1.24774e-04	0.99999	1.00001	30	7.44660e-03	0.99954	1.00060
6	3.16989e-04	0.99998	1.00002	31	7.94513e-03	0.99915	1.00059
7	3.16989e-04	0.99998	1.00002	32	8.00334e-03	0.99913	1.00061
8	4.13363e-04	0.99996	1.00003	33	8.11573e-03	0.99940	1.00069
9	4.97022e-04	0.99995	1.00003	34	8.11573e-03	0.99940	1.00069
10	5.01380e-04	0.99995	1.00003	35	1.01853e-02	0.99903	1.00089
11	1.08730e-03	0.99989	1.00007	36	1.02028e-02	0.99903	1.00089
12	1.08730e-03	0.99989	1.00007	37	1.21915e-02	0.99866	1.00086
13	1.21857e-03	0.99993	1.00008	38	1.21915e-02	0.99866	1.00086
14	1.21857e-03	0.99993	1.00008	39	1.38815e-02	0.99850	1.00117
15	1.53088e-03	0.99988	1.00011	40	1.38815e-02	0.99850	1.00117
16	1.53088e-03	0.99988	1.00011	41	1.45679e-02	0.99893	1.00131
17	2.25288e-03	0.99976	1.00015	42	1.45679e-02	0.99893	1.00131
18	2.50848e-03	0.99974	1.00018	43	1.54646e-02	0.99873	1.00144
19	2.53229e-03	0.99974	1.00018	44	1.54657e-02	0.99873	1.00144
20	3.33210e-03	0.99981	1.00025	45	1.82334e-02	0.99821	1.00176
21	3.33210e-03	0.99981	1.00025	46	1.82334e-02	0.99821	1.00176
22	3.80546e-03	0.99972	1.00030	47	1.84924e-02	0.99795	1.00131
23	3.80757e-03	0.99972	1.00030	48	1.94652e-02	0.99783	1.00152
24	4.35867e-03	0.99953	1.00030	49	1.95719e-02	0.99780	1.00155
25	4.35867e-03	0.99953	1.00030	50	2.30622e-02	0.99746	1.00219

Table 8: The 50 smallest non-zero eigenvalues corresponding to the bending modes for full Gauss quadrature (GA), reduced Gauss quadrature (RGA) and Gauss-Greville quadrature (GA-GR), $p = 4$, 32×32 maximally smooth elements, and *uniform* meshes.

j	GA	RGA/GA	GA-GR/GA	j	GA	RGA/GA	GA-GR/GA
1	2.08630e-05	1.00000	1.00000	26	5.28792e-03	0.99999	1.00000
2	4.17137e-05	1.00000	1.00000	27	5.28792e-03	0.99999	1.00000
3	4.17137e-05	1.00000	1.00000	28	7.39179e-03	0.99999	1.00000
4	1.24771e-04	1.00000	1.00000	29	7.42867e-03	0.99999	0.99999
5	1.24771e-04	1.00000	1.00000	30	7.42867e-03	0.99999	0.99999
6	3.16962e-04	1.00000	1.00000	31	7.93728e-03	0.99999	1.00000
7	3.16962e-04	1.00000	1.00000	32	7.99524e-03	0.99999	1.00000
8	4.13338e-04	1.00000	1.00000	33	8.09662e-03	0.99999	0.99999
9	4.96973e-04	1.00000	1.00000	34	8.09662e-03	0.99999	0.99999
10	5.01329e-04	1.00000	1.00000	35	1.01625e-02	0.99999	0.99999
11	1.08714e-03	1.00000	1.00000	36	1.01798e-02	0.99999	0.99999
12	1.08714e-03	1.00000	1.00000	37	1.21779e-02	0.99999	1.00000
13	1.21814e-03	1.00000	1.00000	38	1.21779e-02	0.99999	1.00000
14	1.21814e-03	1.00000	1.00000	39	1.38514e-02	0.99998	0.99999
15	1.53034e-03	1.00000	1.00000	40	1.38514e-02	0.99998	0.99999
16	1.53034e-03	1.00000	1.00000	41	1.44945e-02	0.99997	0.99996
17	2.25236e-03	1.00000	1.00000	42	1.44945e-02	0.99997	0.99996
18	2.50754e-03	1.00000	1.00000	43	1.53882e-02	0.99997	0.99996
19	2.53131e-03	1.00000	1.00000	44	1.53893e-02	0.99997	0.99996
20	3.32874e-03	1.00000	1.00000	45	1.81476e-02	0.99996	0.99996
21	3.32874e-03	1.00000	1.00000	46	1.81476e-02	0.99996	0.99996
22	3.80170e-03	1.00000	1.00000	47	1.84652e-02	0.99998	1.00000
23	3.80380e-03	1.00000	1.00000	48	1.94235e-02	0.99997	0.99999
24	4.35667e-03	1.00000	1.00000	49	1.95293e-02	0.99997	0.99999
25	4.35667e-03	1.00000	1.00000	50	2.29599e-02	0.99995	0.99995

5 Numerical examples

In this section, we demonstrate the proposed quadratures through various numerical examples. The following quadrature rules are employed:

- GA: full *Gauss* quadrature, defined as $(p+1) \times (p+1)$ Gauss points, which is used for comparison;
- RGA: *reduced Gauss* quadrature, defined in Section 3.1;
- GA-GR: *Gauss-Greville* quadrature, defined in Section 3.2.

5.1 A manufactured solution for the Laplace equation on a 2D domain

In this section, we solve the Laplace equation, $\Delta u = 0$, on a square domain, $\Omega = (0,1) \times (0,1)$. Boundary conditions are calculated and applied according to a manufactured solution, $u(x) = \sinh(\pi x)\sin(\pi y)$. The initial mesh, shown in Figure 9a, consists of one skew quadratic element. For the mesh refinement studies uniform knot insertion, i.e., h-refinement, is used, while k-refinement is

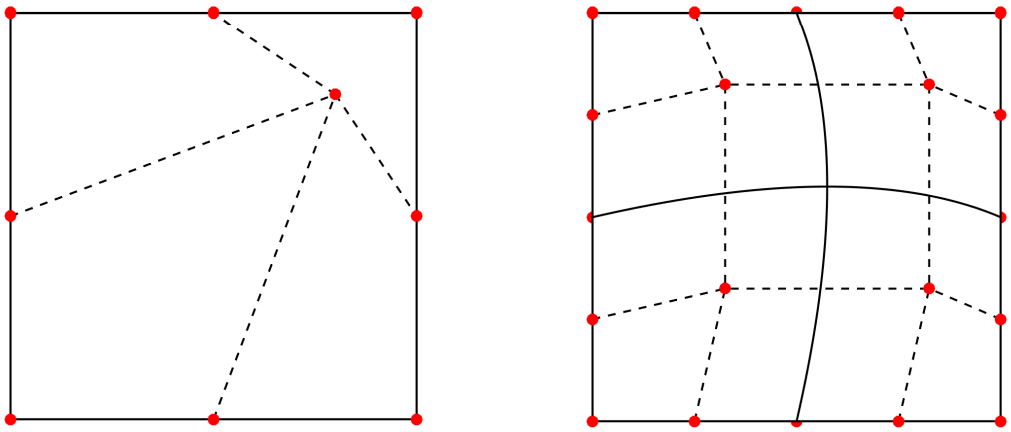

(a) Initial mesh. (b) Refine once.

Figure 9: Laplace equation $\Delta u = 0$, where $u = \sinh(\pi x)\sin(\pi y)$: Skew meshes and control nets, maximal smoothness, $p = 2$. Red dots denote control points.

applied to elevate the order. The skew initial mesh is used to make the geometrical mapping nonlinear [25, 26], thus leading to a non-constant determinant of the Jacobian matrix in the calculation of the stiffness matrices. Figure 10 compares the convergence rates of the L^2-norm error of the x-derivative of u for various quadrature rules, where the L^2-norm is calculated through the same quadrature rules used for analysis. As can be seen in Figure 10a, for the GA-GR rule, an optimal convergence rate is achieved for $p = 2$, whereas for $p > 2$ the convergence rates are 2.5. Figure 10b shows that for $p = 2$ the RGA obtains a superconvergence rate equal to 3. This is because, for this case, the RGA quadrature points are the 2×2 Gauss quadrature points, which happens to be the superconvergence points for the first derivative of u [27]. For odd degrees, i.e., $p = 3$ and 5, the convergence rates for RGA are 2.5, i.e., the same as GA-GR. For $p = 4$ and 6, the convergence rates for RGA are 3.5, which is one order higher than that for GA-GR as we explained in Section 3.
Next, we employ a non-uniform initial mesh as shown in Figure 11a, in which case, negative weights will occur with the Greville quadrature rules [1] but not with the proposed GA-GR and RGA rules. As can be seen in Figure 12, both GA-GR and RGA achieve the same convergence rates as those obtained with skewed meshes in Figure 10.

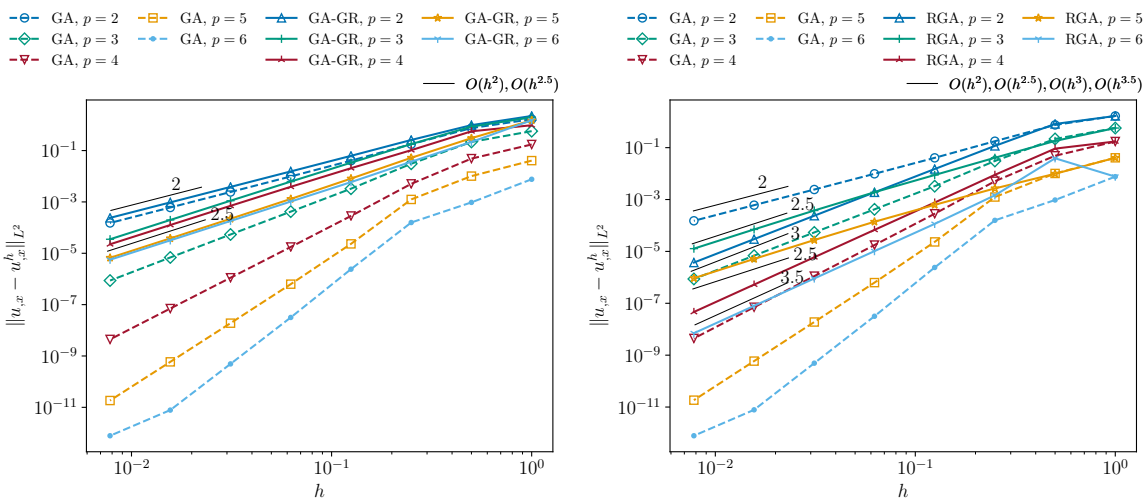

(a) GA VS GA-GR.

(b) GA VS RGA.

Figure 10: Laplace equation $\Delta u = 0$, where $u = \sinh(\pi x)\sin(\pi y)$: Convergence rates of the L^2-norm error of the x-derivative of the solution u, for quadratures GA, GA-GR and RGA, degrees $p = 2$ to 6, and *skew* meshes.

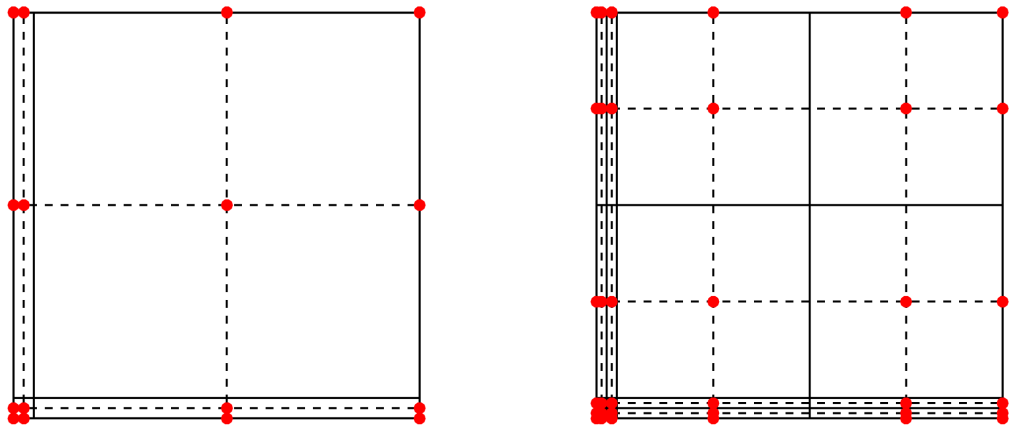

(a) Initial mesh.

(b) Refine once.

Figure 11: Laplace equation $\Delta u = 0$, where $u = \sinh(\pi x)\sin(\pi y)$: Non-uniform meshes and control nets, maximal smoothness, $p = 2$. Red dots denote control points.

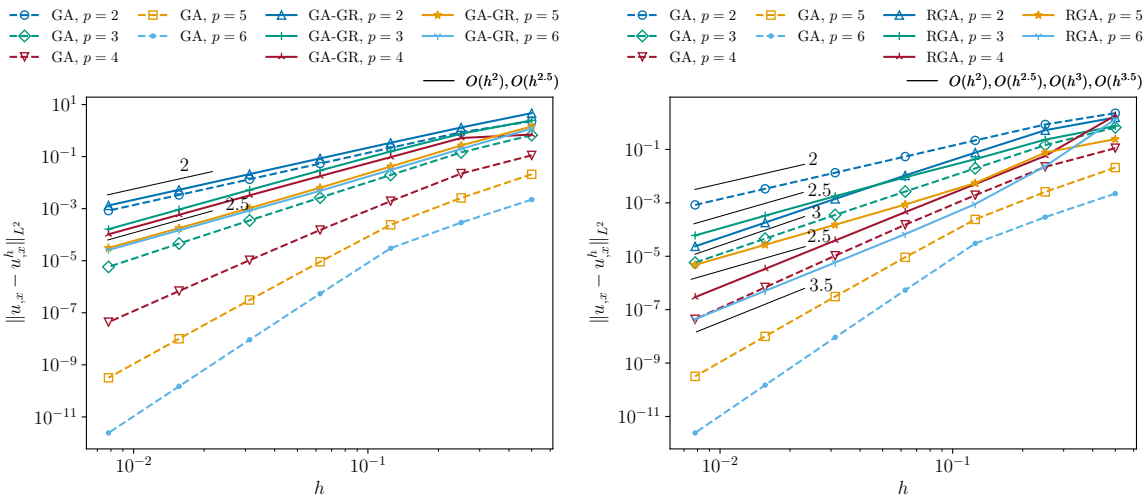

(a) GA VS GA-GR. (b) GA VS RGA.

Figure 12: Laplace equation $\Delta u = 0$, where $u = \sinh(\pi x)\sin(\pi y)$: Convergence rates of the L^2-norm error of the x-derivative of the solution u, for quadratures GA, GA-GR and RGA, degrees $p = 2$ to 6, and *non-uniform* meshes.

5.2 A manufactured solution for the Poisson equation on a 3D domain

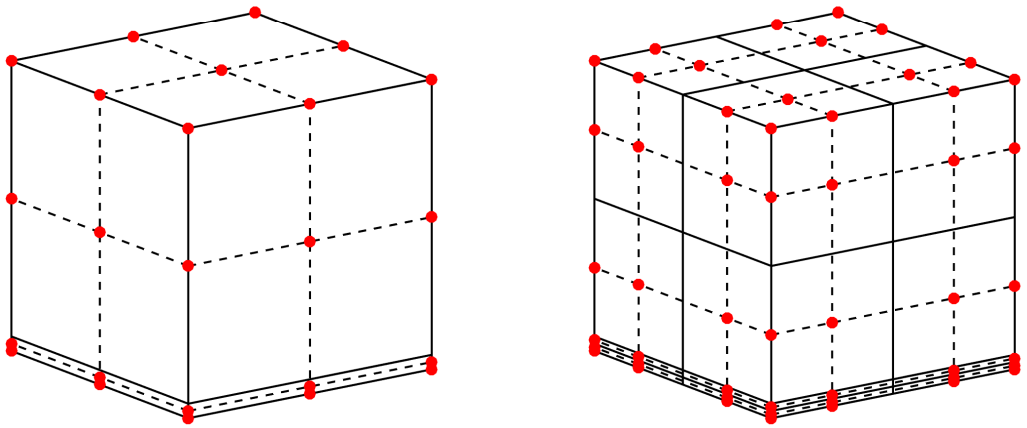

(a) Initial mesh. (b) Refine once.

Figure 13: Poisson equation, $-\Delta u = f$, with $u(x) = \sinh(\pi x)\sin(\pi y)\sin(\pi z)$: Non-uniform meshes and control nets, maximal smoothness, $p = 2$. Red dots denote control points.

In this section, we solve the Poisson equation, $-\Delta u = f$, on a cubic domain, $\Omega = (0,1) \times (0,1) \times (0,1)$, where f and the boundary conditions are calculated via the manufactured solution, $u(x) = \sinh(\pi x)\sin(\pi y)\sin(\pi z)$. The initial mesh, shown in Figure 13a, consists of two non-uniform quadratic elements, and uniform h- and k-refinements are used afterwards. Figure 13b shows the mesh after one h-refinement.

Figure 14 compares the convergence rates of the L^2-norm error of the x-derivative of u for various quadrature rules. As can be seen, the convergence rates for both GA-GR and RGA are the same as those observed for the 2D Laplace equation in Section 5.1. Next, we add a C^{p-2}-continuous surface

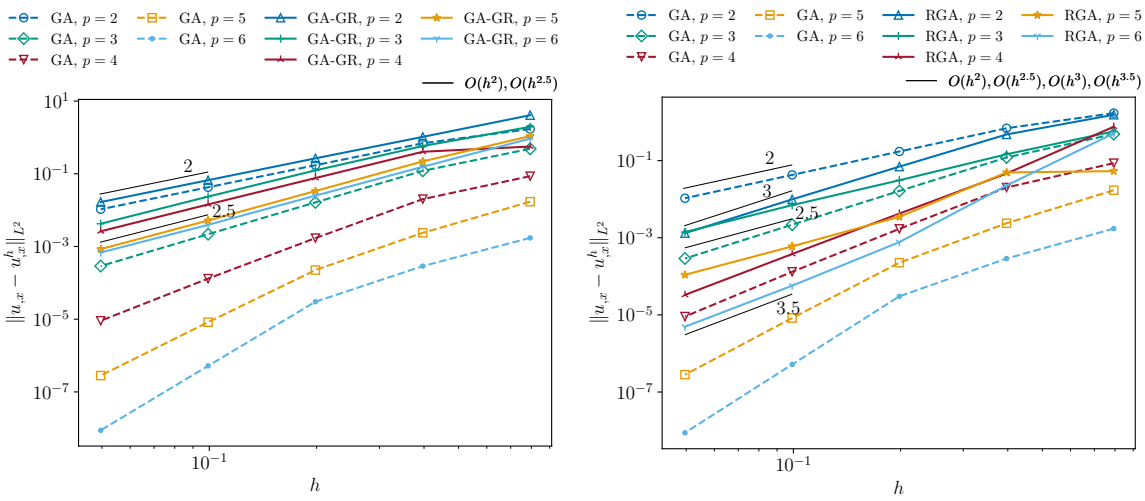

(a) GA VS GA-GR.

(b) GA VS RGA.

Figure 14: Poisson equation, $-\Delta u = f$, with $u(x) = \sinh(\pi x)\sin(\pi y)\sin(\pi z)$: Convergence rates of the L^2-norm error of the x-derivative of the solution u, for quadratures GA, GA-GR and RGA, degrees $p = 2$ to 6, and *non-uniform* meshes.

into the initial mesh as shown in Figure 15a, and keep it C^{p-2}-continuous in sequential refinement steps as shown in Figure 15b. Figure 16 shows that the convergence rates of the proposed quadrature rules are consistent with those observed in Figure 14 for meshes with maximal smoothness.

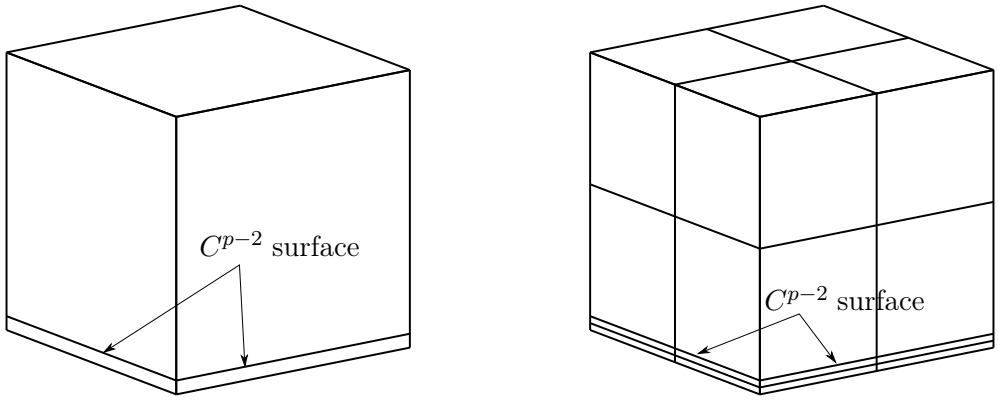

(a) Initial mesh with a C^{p-2}-continuous surface.

(b) Refine once.

Figure 15: Poisson equation, $-\Delta u = f$, with $u(x) = \sinh(\pi x)\sin(\pi y)\sin(\pi z)$: Non-uniform meshes with a C^{p-2}-continuous surface.

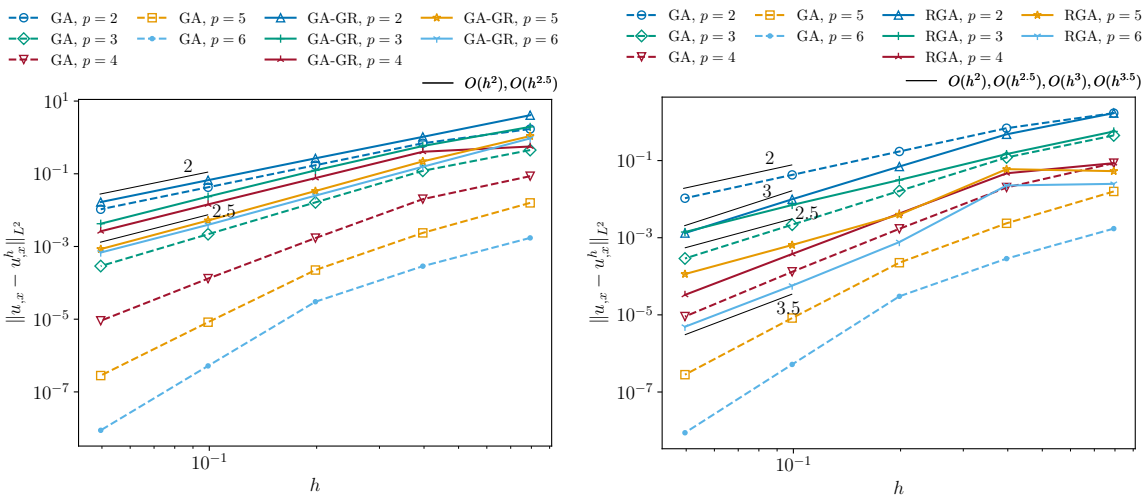

(a) GA VS GA-GR.

(b) GA VS RGA.

Figure 16: Poisson equation, $-\Delta u = f$, with $u(x) = \sinh(\pi x)\sin(\pi y)\sin(\pi z)$: Convergence rates of the L^2-norm error of the x-derivative of the solution u, for quadratures GA, GA-GR and RGA, degrees $p = 2$ to 6, and *non-uniform* meshes with a C^{p-2}-continuous surface.

5.3 A manufactured solution for the biharmonic equation on a 2D domain

In this section, we consider the biharmonic equation, $\Delta^2 u = f$, on the domain $(0,1) \times (0,1)$, where f is calculated from a manufactured solution, $u(x,y) = \sin^2(2\pi x)\sin^2(2\pi y)$, obtained from [28]. The initial mesh consists of 4×4 maximally smooth elements generated by uniformly subdividing the initial non-uniform mesh in Figure 11a. The corresponding homogeneous boundary conditions, $u = \frac{\partial u}{\partial \mathbf{n}} = 0$, are applied by clamping the degrees-of-freedom of the two outer rings of boundary nodes.

Figure 17 illustrates the convergence rates of the L^2-norm error of the x-derivative of the solution u for various quadrature rules and basis degrees. Like the full Gauss quadrature rule, both GA-GR and RGA achieve optimal rates for all degrees $p = 2$ to 6 except that GA-GR obtains a suboptimal convergence rate for $p = 5$. Note that, for $p = k = 2$, the Greville quadrature rule is identical to the Simpson's rule [1]. As a result, all Greville quadrature weights are positive and GA-GR is simply the Greville quadrature rule. The accuracy of Simpson's rule is well known and Schillinger et al. [16] showed that Simpson's rule achieves almost identical results as the full Gauss quadrature rule for quadratic IGA elements. Therefore, to avoid duplication, results for $p = 2$ were omitted in Figure 17.

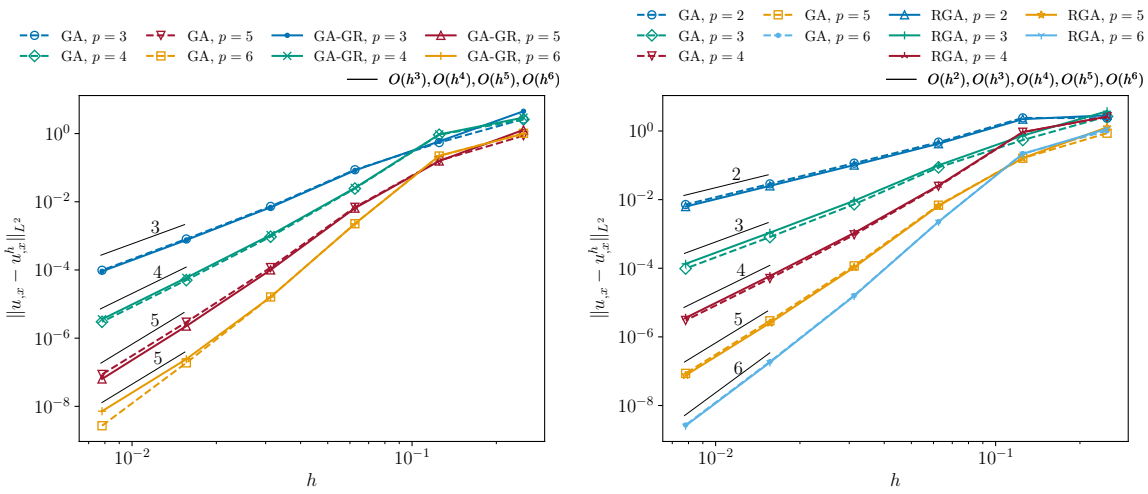

(a) GA VS GA-GR.

(b) GA VS RGA.

Figure 17: Biharmonic equation $\Delta^2 u = f$, where $u(x, y) = \sin^2(2\pi x)\sin^2(2\pi y)$: Convergence rates of the L^2-norm error of the x-derivative of the solution u, for quadratures GA, GA-GR and RGA, and various basis degrees.

5.4 Infinite plate with a hole

We next simulate the classical infinite elastic plate with a circular hole as shown in Figure 18a. Due to symmetry, only one quarter of the infinite plate is modeled as an annulus as illustrated in Figure 18b, where R_1 and R_2 are the inside and outside radii of the annulus, E is Young's modulus, and ν is Poisson's ratio. An analytical solution to this problem can be found in [29, 30] and is

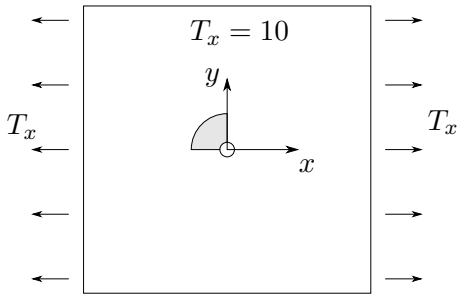

(a) Infinite plate with a hole subject to a uniaxial tension at $x = \pm\infty$.

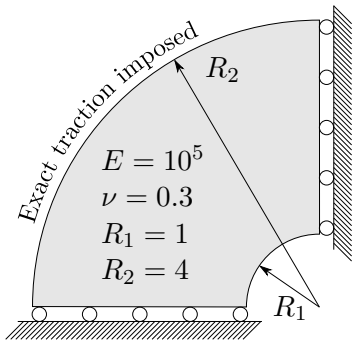

(b) Problem setup.

Figure 18: Schematics of infinite plate with a hole.

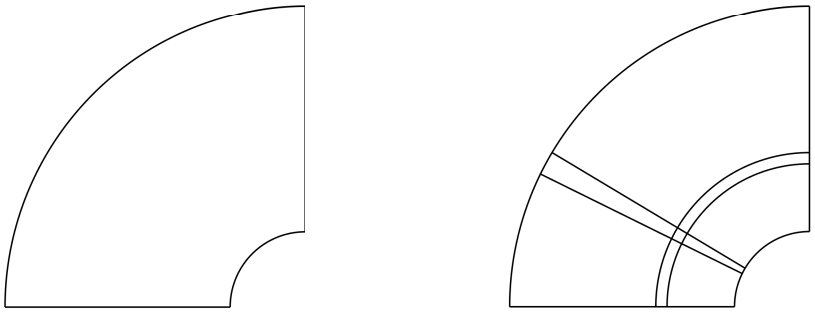

(a) Uniform mesh. (b) Non-uniform mesh.

Figure 19: Infinite plate with a hole: Initial meshes.

reproduced here for completeness

$$\begin{aligned}
\sigma_{rr}(r,\theta) &= \frac{T_x}{2}\left(1-\frac{R_1^2}{r^2}\right)+\frac{T_x}{2}\left(1-4\frac{R_1^2}{r^2}+3\frac{R_1^4}{r^4}\right)\cos(2\theta),\\
\sigma_{\theta\theta}(r,\theta) &= \frac{T_x}{2}\left(1+\frac{R_1^2}{r^2}\right)-\frac{T_x}{2}\left(1+3\frac{R_1^4}{r^4}\right)\cos(2\theta),\\
\sigma_{r\theta}(r,\theta) &= -\frac{T_x}{2}\left(1+2\frac{R_1^2}{r^2}-3\frac{R_1^4}{r^4}\right)\sin(2\theta).
\end{aligned} \tag{28}$$

Figure 20 compares the convergence rates of the L^2-norm of the stress component σ_{xx} error for GA, GA-GR and RGA. The initial mesh contains only one element as shown in Figure 19a and uniform h- and k-refinements are used afterward. As can be seen in Figure 20a, GA-GR achieves optimal rate for $p = 2$, and as the basis degrees increase the convergence rates are bounded from above by 2.5. For RGA, a superoptimal convergence rate 3 is achieved for $p = 2$ and suboptimal convergence rates 2.5 and 3.5 are obtained for odd- and even-order bases with degrees $p > 2$, respectively. Figure 21 shows contour plots of the stress component σ_{xx} for different quadrature rules and degrees with 10×10 maximally smooth elements. It can be seen that even though RGA and GA-GR use many fewer quadrature points than GA, the stress results are very similar.

We now consider a non-uniform initial mesh as shown in Figure 19b. The convergence behaviors and the stress contour plots, shown in Figures 22 and 23, are consistent with what we observed above for the uniform mesh cases.

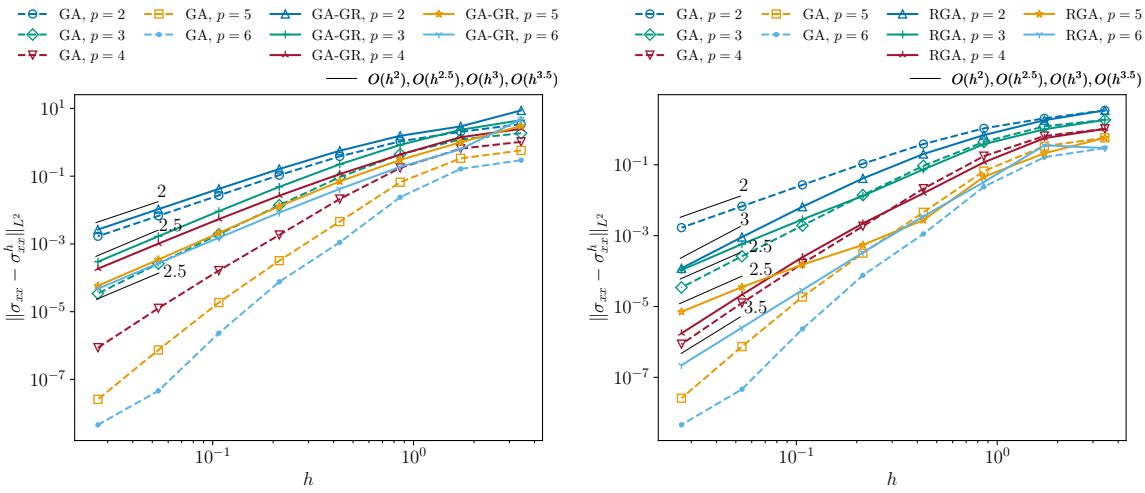

(a) GA VS GA-GR.

(b) GA VS RGA.

Figure 20: Infinite plate with a hole: Convergence rates of the L^2-norm of the stress component σ_{xx} error, for various quadratures, degrees $p = 2$ to 6, and *uniform* meshes.

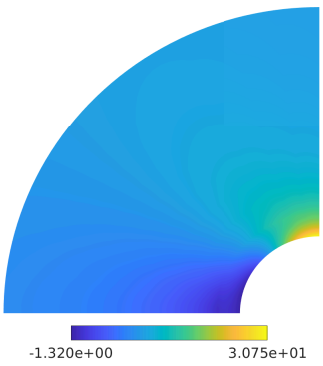

(a) GA, $p = 2$.

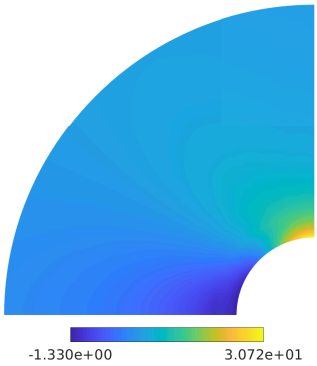

(b) GA-GR, $p = 2$.

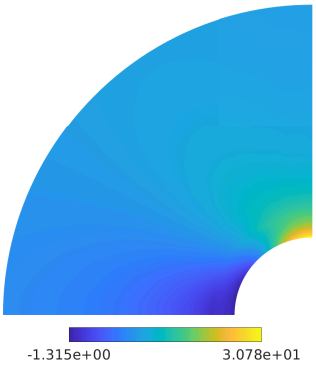

(c) RGA, $p = 2$.

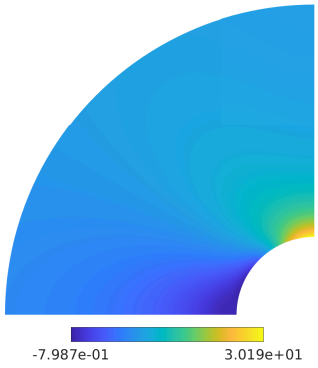

(d) GA, $p = 3$.

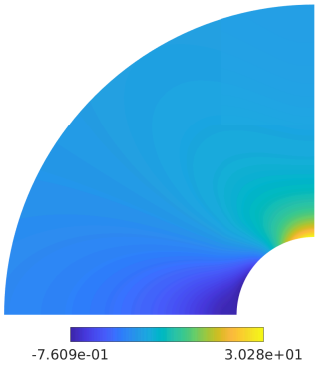

(e) GA-GR, $p = 3$.

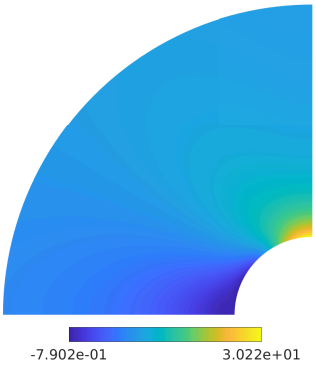

(f) RGA, $p = 3$.

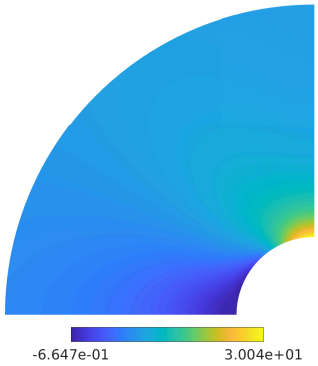

(g) GA, $p = 4$.

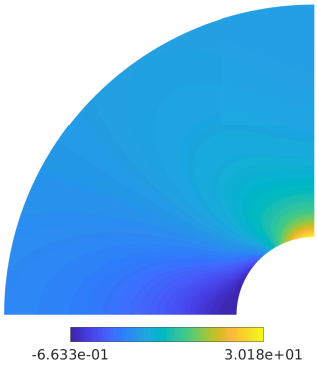

(h) GA-GR, $p = 4$.

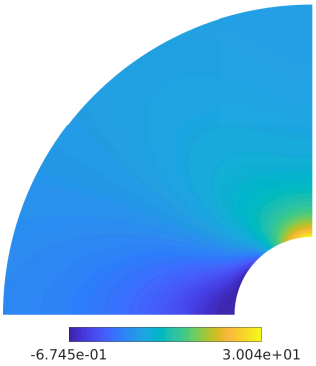

(i) RGA, $p = 4$.

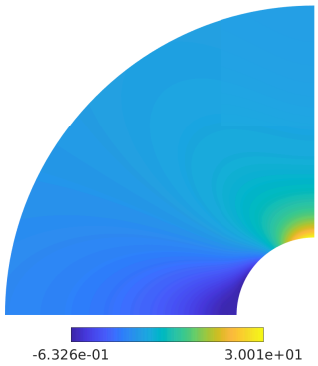

(j) GA, $p = 5$.

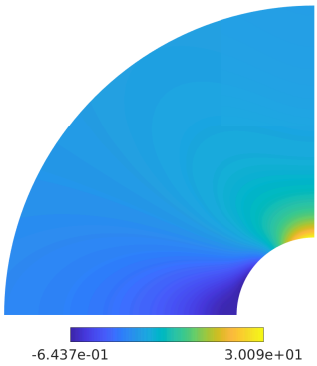

(k) GA-GR, $p = 5$.

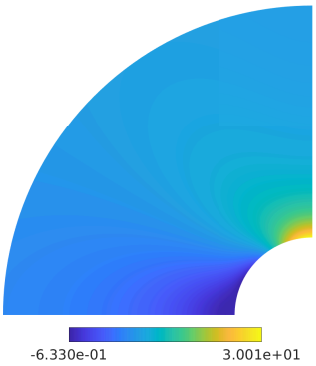

(l) RGA, $p = 5$.

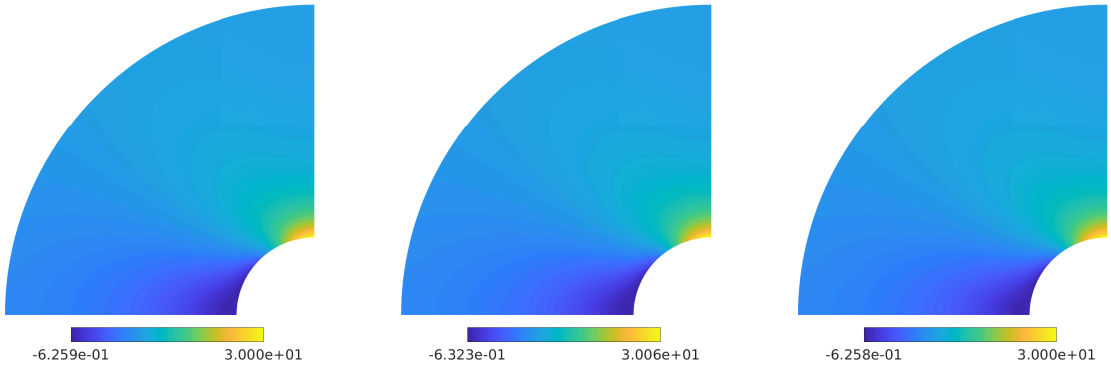

(m) GA, $p = 6$. (n) GA-GR, $p = 6$. (o) RGA, $p = 6$.

Figure 21: Infinite plate with a hole: Stress σ_{xx} for quadrature rules GA (left), GA-GR (middle) and RGA (right), degrees $p = 2$ to 6, 10×10 elements, *uniform* meshes. Note that the stress concentration of a factor of 3 in σ_{xx} is accurately captured in all cases.

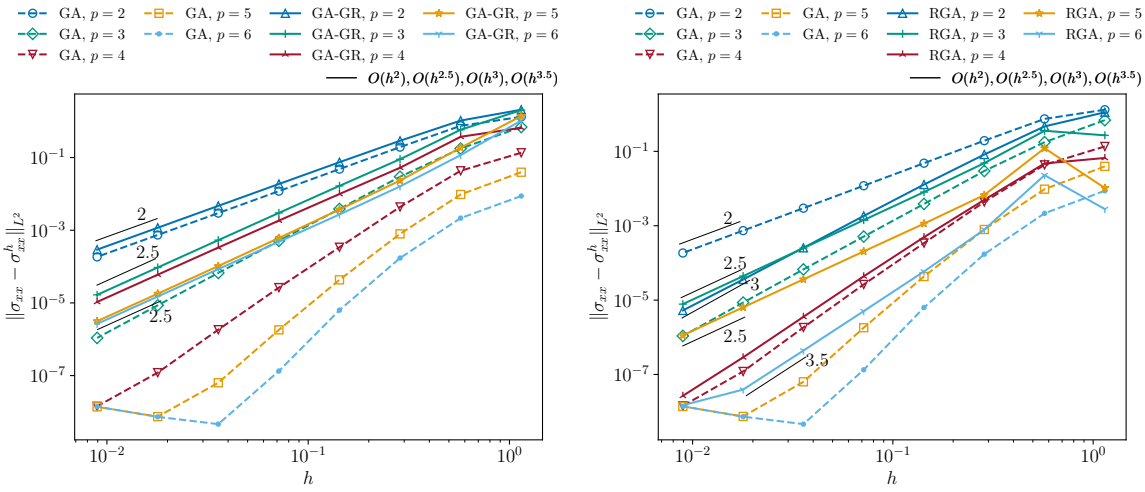

(a) GA VS GA-GR. (b) GA VS RGA.

Figure 22: Infinite plate with a hole: Convergence rates of the L^2-norm error with respect to the stress component σ_{xx}, for various quadratures, degrees $p = 2$ to 6, and *non-uniform* meshes.

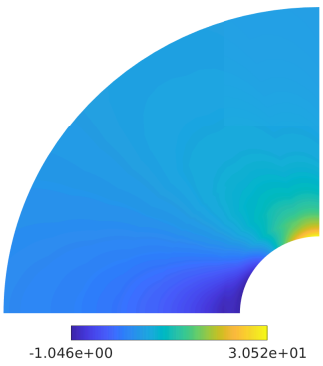

(a) GA, $p = 2$.

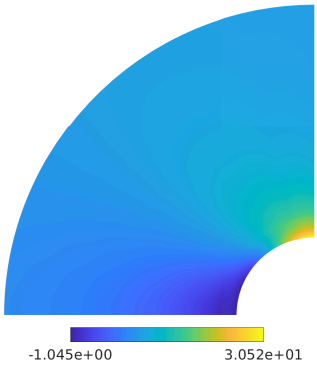

(b) GA-GR, $p = 2$.

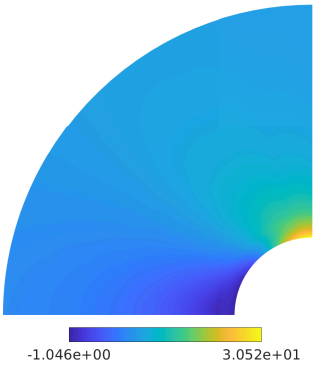

(c) RGA, $p = 2$.

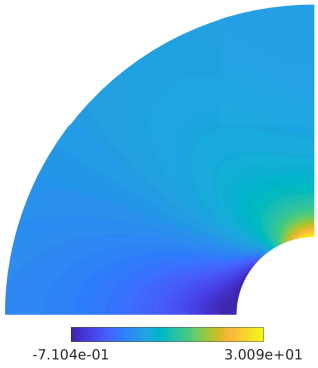

(d) GA, $p = 3$.

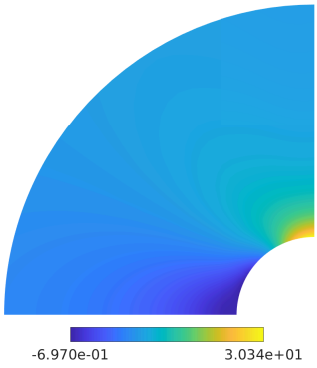

(e) GA-GR, $p = 3$.

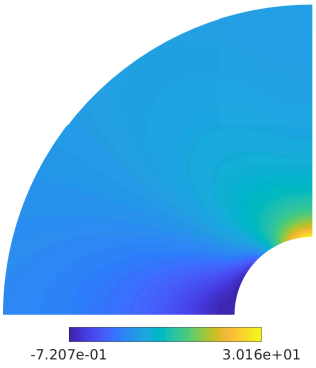

(f) RGA, $p = 3$.

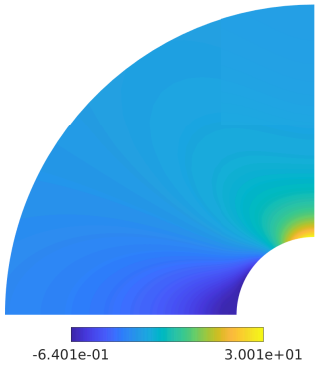

(g) GA, $p = 4$.

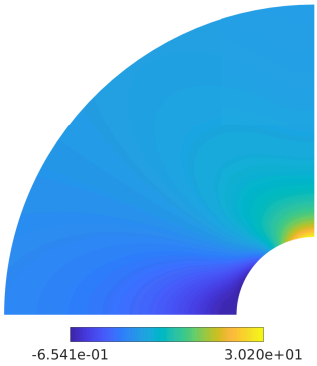

(h) GA-GR, $p = 4$.

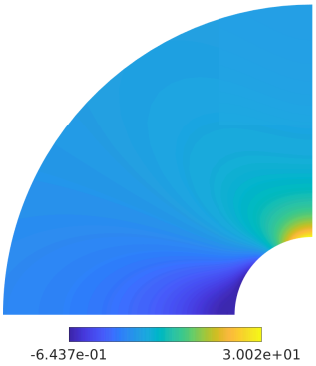

(i) RGA, $p = 4$.

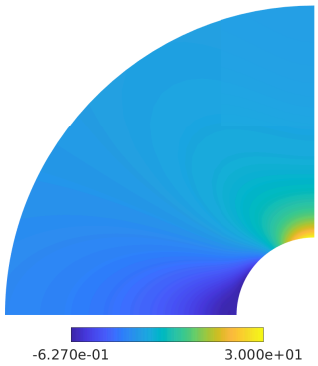

(j) GA, $p = 5$.

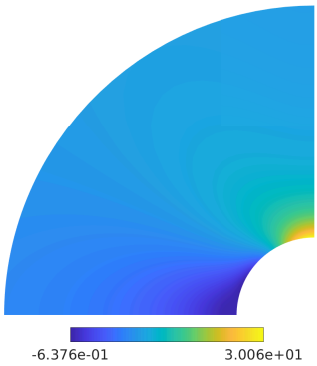

(k) GA-GR, $p = 5$.

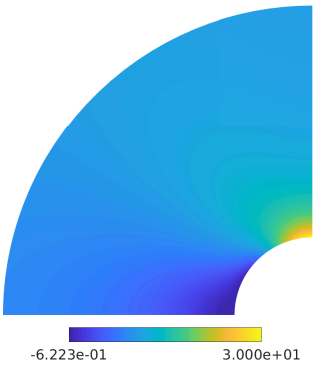

(l) RGA, $p = 5$.

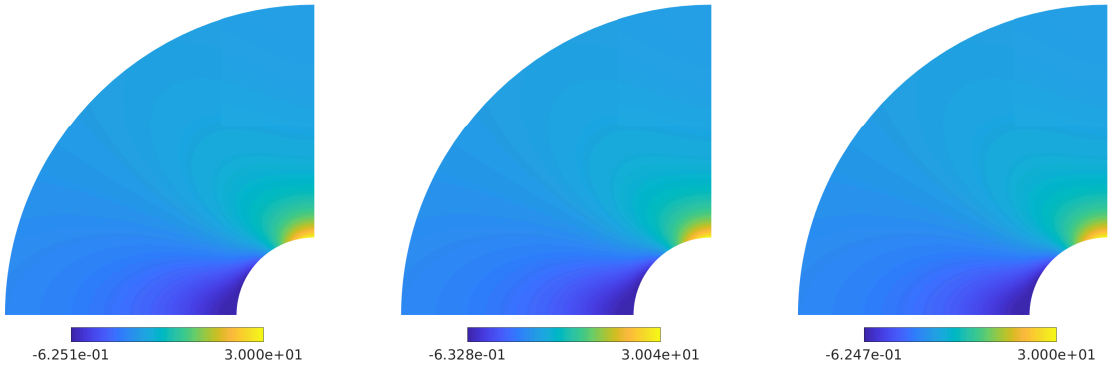

(m) GA, $p = 6$. (n) GA-GR, $p = 6$. (o) RGA, $p = 6$.

Figure 23: Infinite plate with a hole: Stress σ_{xx} for quadrature rules GA (left), GA-GR (middle) and RGA (right), degrees $p = 2$ to 6, 12×12 elements, *non-uniform* meshes. Note that the stress concentration of a factor of 3 in σ_{xx} is accurately captured in all cases.

5.5 Cylindrical shell subject to transverse loading in the radial direction

In this section we test the cylindrical shell subject to a transverse loading in the radial direction, which, even though ostensibly simple, reveals several potential shortcomings of shell elements. Figure 24a shows a schematic with radius $R = 10$, width $b = 1$, and thickness t. Young's modulus and Poisson's ratio are $E = 1000$ and $\nu = 0$, respectively. The cylindrical shell is clamped at one end and subject to a traction, $q_x = -0.1t^3$, at the other end. The analytical membrane force and bending moment, based on static equilibrium, are $n_{11}^{\text{exact}} = q_x \cos\theta$ and $m_{22}^{\text{exact}} = -q_x R \cos\theta$, respectively, where, as illustrated in Figure 24a, θ is the central angle and the subscripts "11" and "22" indicate the local coordinate components, i.e., those along the circumferential direction and parallel to the y-axis. The initial mesh consists of 2×1 elements, as shown in Figure 24b, and subsequent h- and k-refinements are used in the circumferential direction.

Figure 25 shows the convergence rates of the membrane force, calculated from KL shell theory [1], in terms of the relative error in the L^2-norm for GA, GA-GR and RGA, degrees $p = 2$ to 6, and slendernesses $R/t = 100, 1000$ and 10000. As can be seen in the left column, GA-GR obtains the same convergence rates as GA for all degrees and slendernesses except that, for $p = 6$ and slenderness $R/t = 100$, the optimal convergence rate for GA-GR is lost as the mesh is refined. We note that, for $p = 2$, as the slenderness increases, optimal convergence rates are lost for both quadrature rules due to severe locking which, however, is alleviated by higher-order bases. On the other hand, as shown in the right column, RGA obtains the same convergence rates as GA for $p = 3$ to 6 and all slendernesses, but it obviously converges faster than GA for $p = 2$. Additionally, RGA achieves better results for coarse meshes in all cases, especially for large slendernesses, due to its ability in alleviating locking.

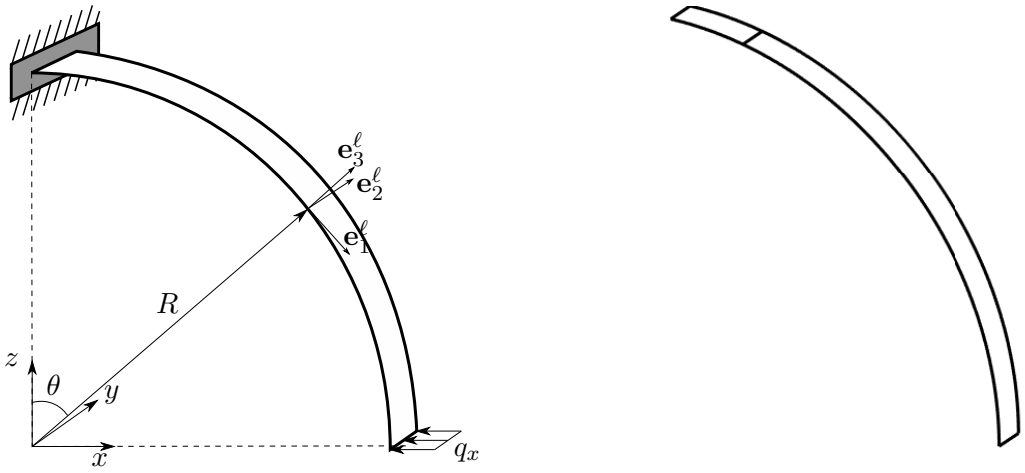

(a) Schematic. (b) Initial mesh.

Figure 24: Cylindrical shell subject to transverse loading in the radial direction. $\{e_i^\ell\}_{i=1}^3$ is a local Cartesian coordinate basis used for calculating resultant forces [1].

Figure 26 compares the accuracy of the proposed quadrature rules with that of GA for the bending moment according to KL shell theory. As can be seen on the left, GA-GR and GA obtain comparable accuracy for all degrees and slendernesses considered. More specifically, for slenderness $R/t = 100$, optimal rates are achieved for $p = 2$ and 3, and for $p > 3$ the error quickly levels off at a very small value around 10^{-5} and convergence rates are not observed. As the slenderness increases, locking becomes severe and affects the convergence rates unexpectedly. For instance, for $p = 3$ and $R/t = 1000$, both GA and GA-GR obtain the optimal convergence rate, but, as the slenderness increases to $R/t = 10000$, a superoptimal convergence rate of 5.5 is observed. Again, as shown on the right, RGA behaves similarly as GA for most cases but it achieves better results for $p = 2$ and for coarse meshes.

Figures 27 and 28 compare the convergence rates of the membrane force and bending moment calculated from RM shell theory [1] for GA, GA-GA and RGA. The convergence behavior is consistent with that observed previously for KL shells in Figures 25 and 26.

To further examine the quality of the resultant force, the membrane force n_{11}, normalized by the maximum value of the exact solution n_{11}^{exact}, is illustrated in Figures 29, where slenderness $R/t = 100$, various numbers of quadratic KL and RM shell elements, and different quadrature rules are used. It can be seen that all three quadrature rules, GA, GA-GR and RGA, obtain similar results for KL shells on the left and RM shells on the right, which oscillate significantly even with 256 elements. As the utilized meshes here are obtained by uniformly subdividing the two initial elements in Figure 24b, the elements close to the clamped end are smaller than those close to the free end, thus leading to smaller stress oscillation. Figure 30 shows that, with 32 KL or RM shell elements, elevating the basis orders effectively alleviates the membrane force oscillation for all quadrature rules, and for $p \geq 5$ the oscillation disappears for all cases. Figure 31 shows the normalized bending moment m_{22} for different quadrature rules and various numbers of quadratic KL and RM shell elements. Oscillations can be observed for all three quadrature rules with 32 KL shell elements as shown in the left column, and they reduce as the number of elements increases. With 32 quadratic RM shell elements, GA and GA-GR rules also exhibit inaccurate bending moment while RGA achieves accurate results. In addition to increasing the number of elements, elevating basis orders also effectively reduces bending moment oscillations, but the corresponding results are

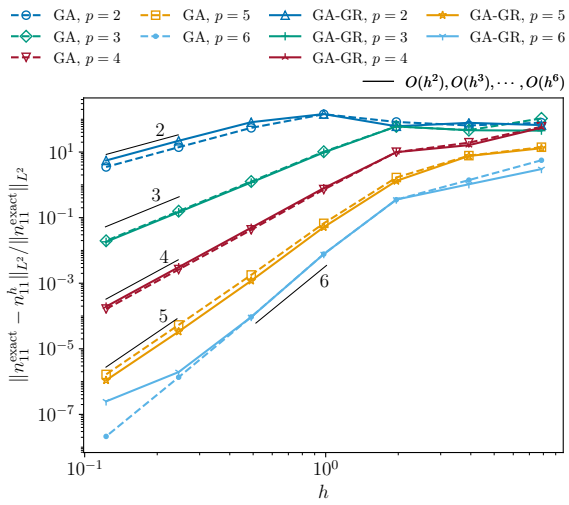

(a) $R/t = 100$, GA VS GA-GR.

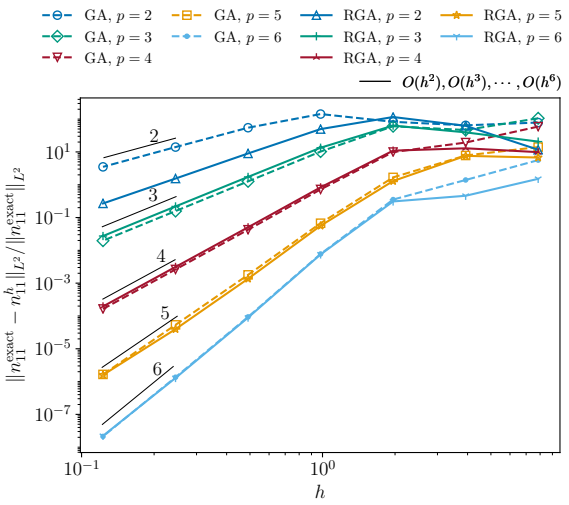

(b) $R/t = 100$, GA VS RGA.

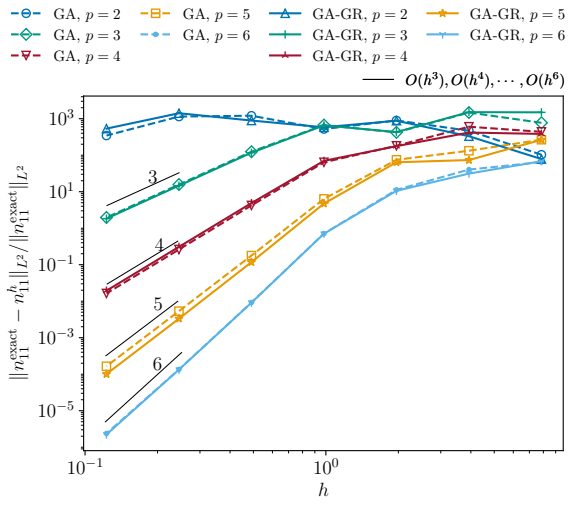

(c) $R/t = 1000$, GA VS GA-GR.

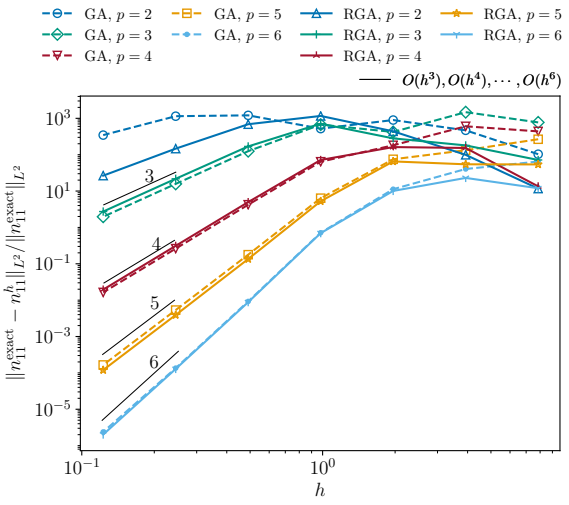

(d) $R/t = 1000$, GA VS RGA.

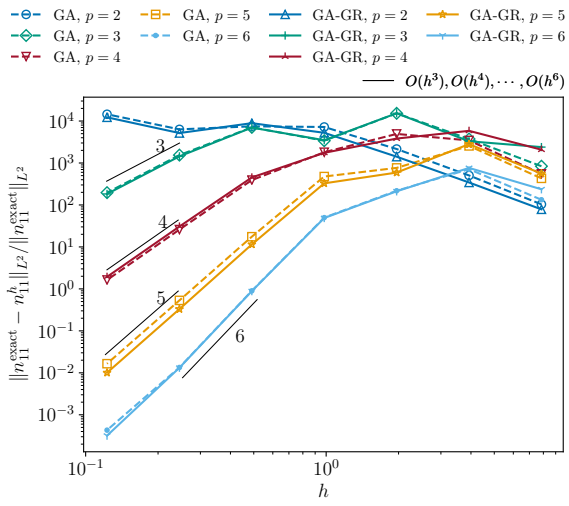

(e) $R/t = 10000$, GA VS GA-GR.

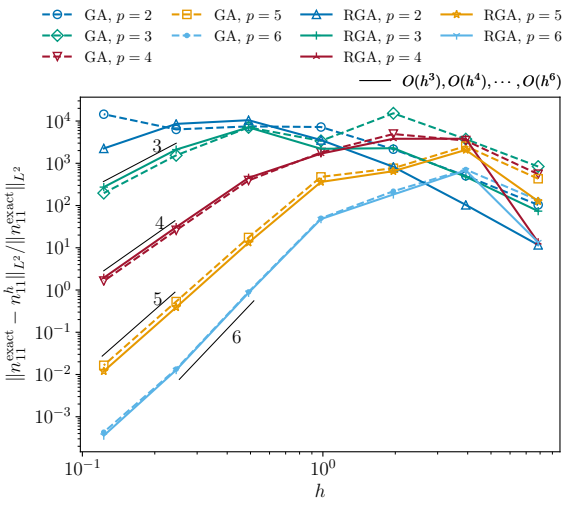

(f) $R/t = 10000$, GA VS RGA.

Figure 25: Cylindrical KL shell: Membrane force convergence rates for GA, GA-GR and RGA, increasing slenderness $R/t = 100, 1000, 10000$, degrees $p = 2$ to 6, and maximally smooth elements.

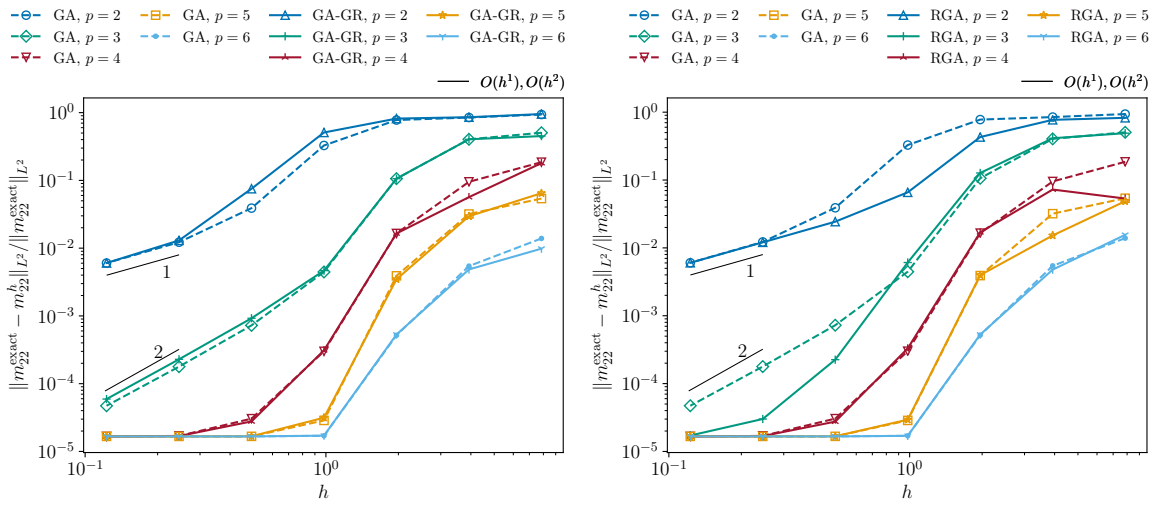

(a) $R/t = 100$, GA VS GA-GR.

(b) $R/t = 100$, GA VS RGA.

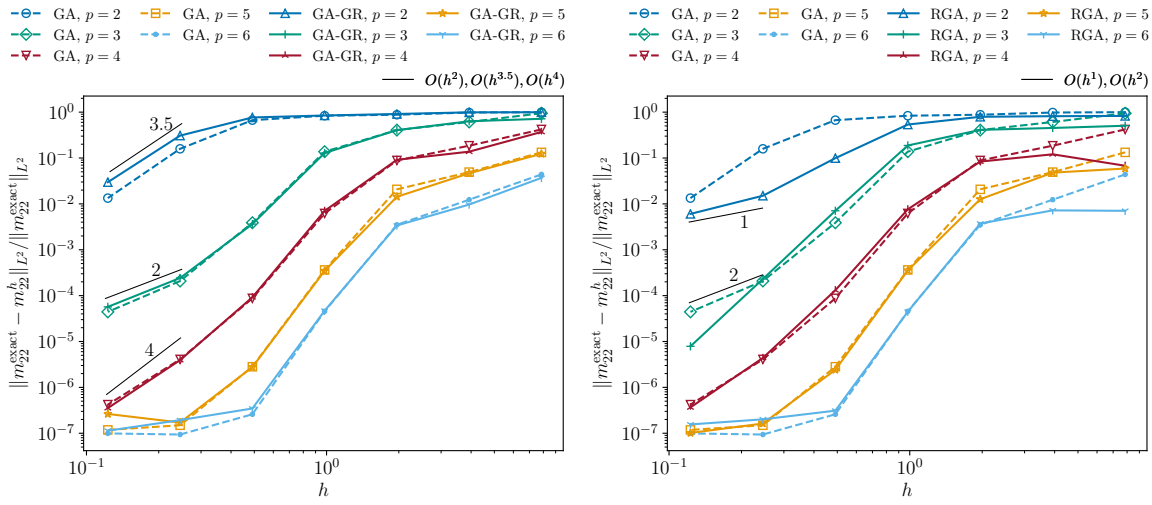

(c) $R/t = 1000$, GA VS GA-GR.

(d) $R/t = 1000$, GA VS RGA.

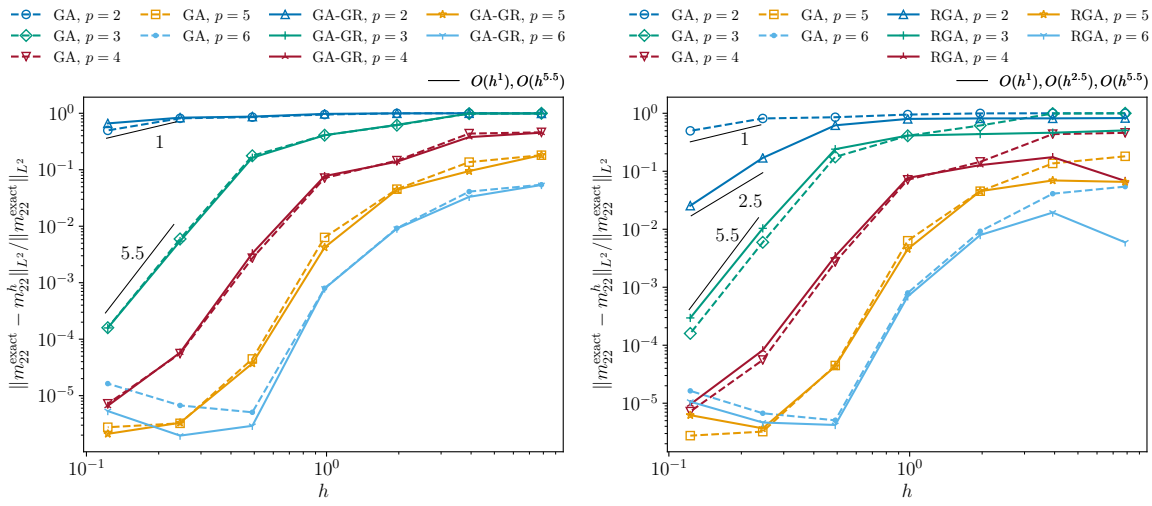

(e) $R/t = 10000$, GA VS GA-GR.

(f) $R/t = 10000$, GA VS RGA.

Figure 26: Cylindrical KL shell: Bending moment convergence rates for GA, GA-GR and RGA, increasing slenderness $R/t = 100, 1000, 10000$, degrees $p = 2$ to 6, and maximally smooth elements.

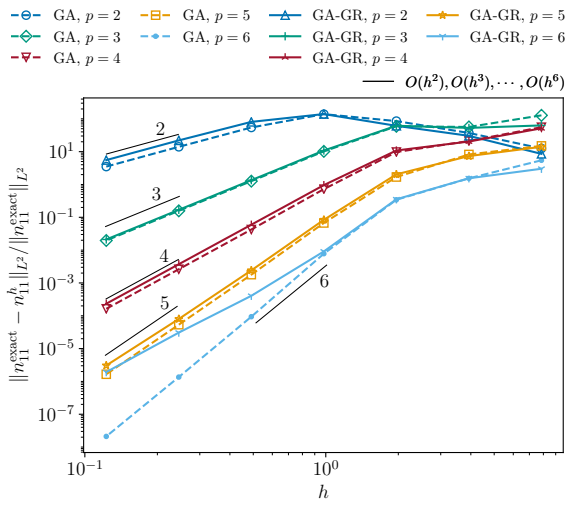

(a) $R/t = 100$, GA VS GA-GR.

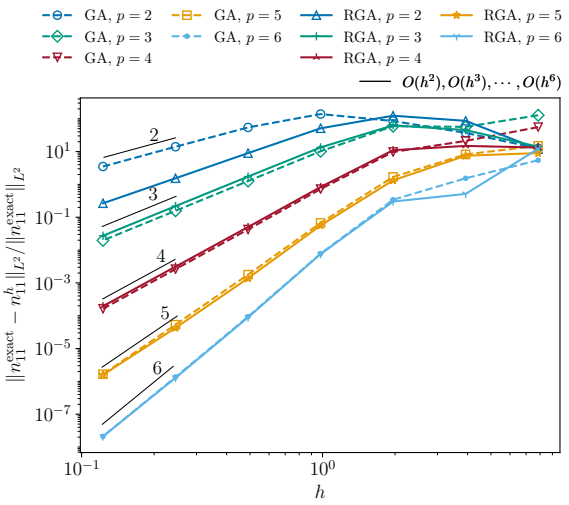

(b) $R/t = 100$, GA VS RGA.

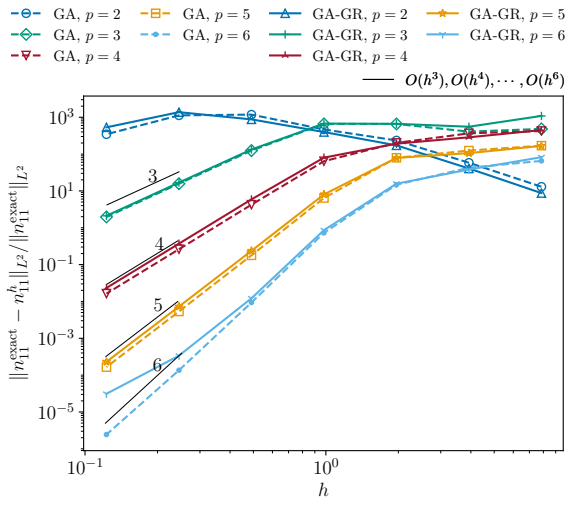

(c) $R/t = 1000$, GA VS GA-GR.

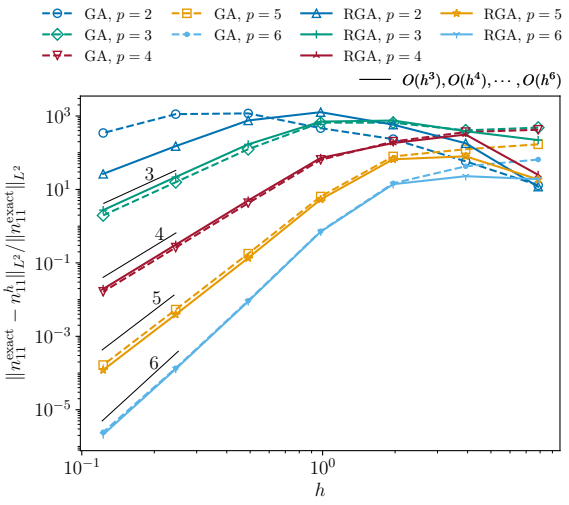

(d) $R/t = 1000$, GA VS RGA.

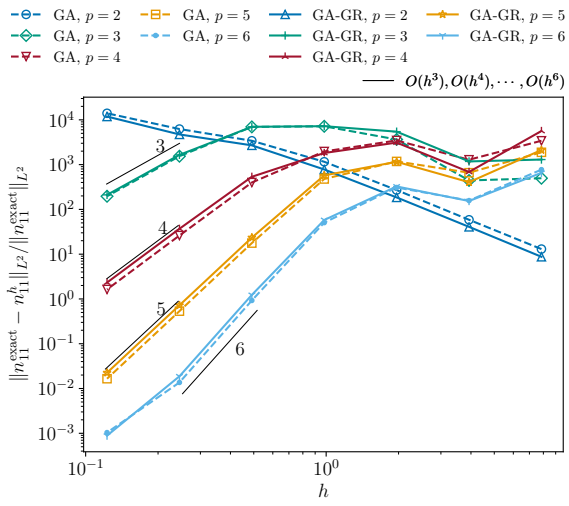

(e) $R/t = 10000$, GA VS GA-GR.

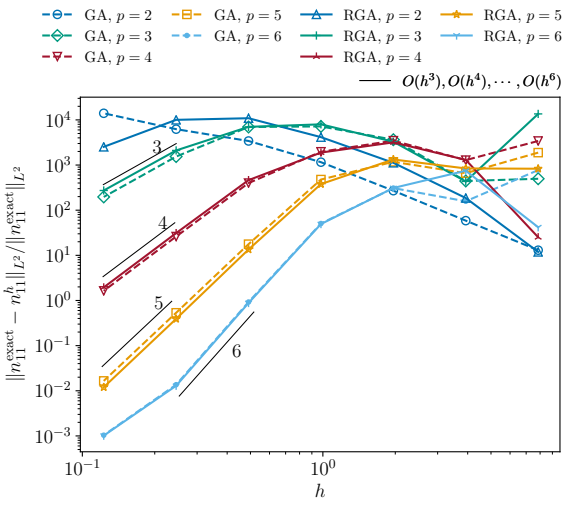

(f) $R/t = 10000$, GA VS RGA.

Figure 27: Cylindrical RM shell: Membrane force convergence rates for GA, GA-GR and RGA, increasing slenderness $R/t = 100, 1000, 10000$, degrees $p = 2$ to 6, and maximally smooth elements.

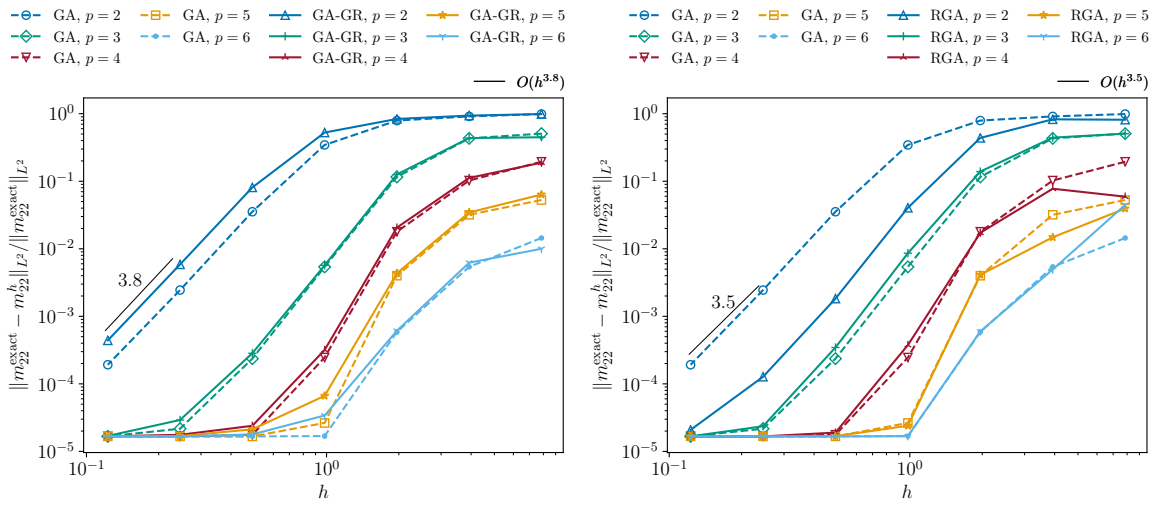

(a) $R/t = 100$, GA VS GA-GR.

(b) $R/t = 100$, GA VS RGA.

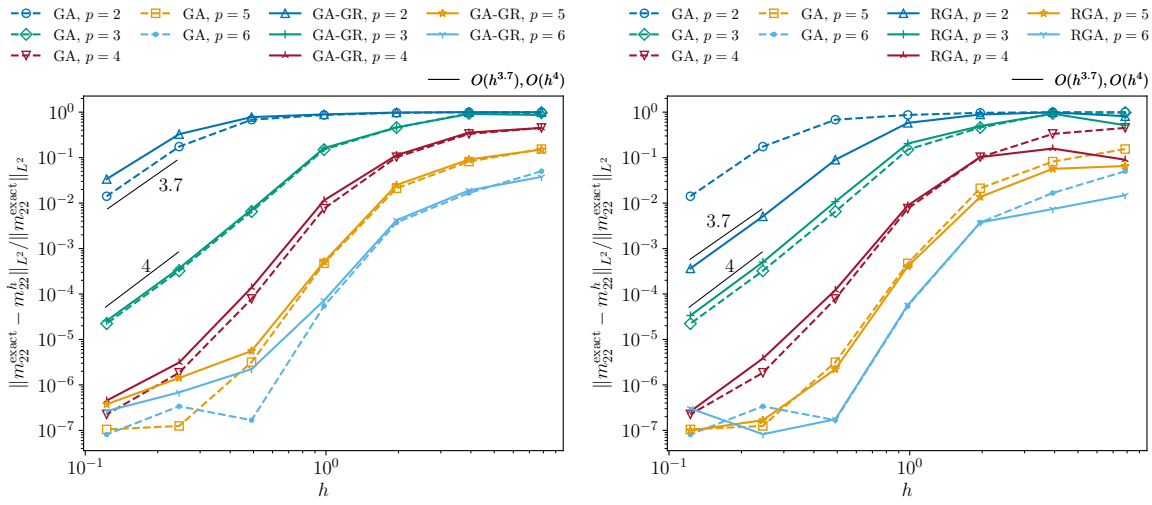

(c) $R/t = 1000$, GA VS GA-GR.

(d) $R/t = 1000$, GA VS RGA.

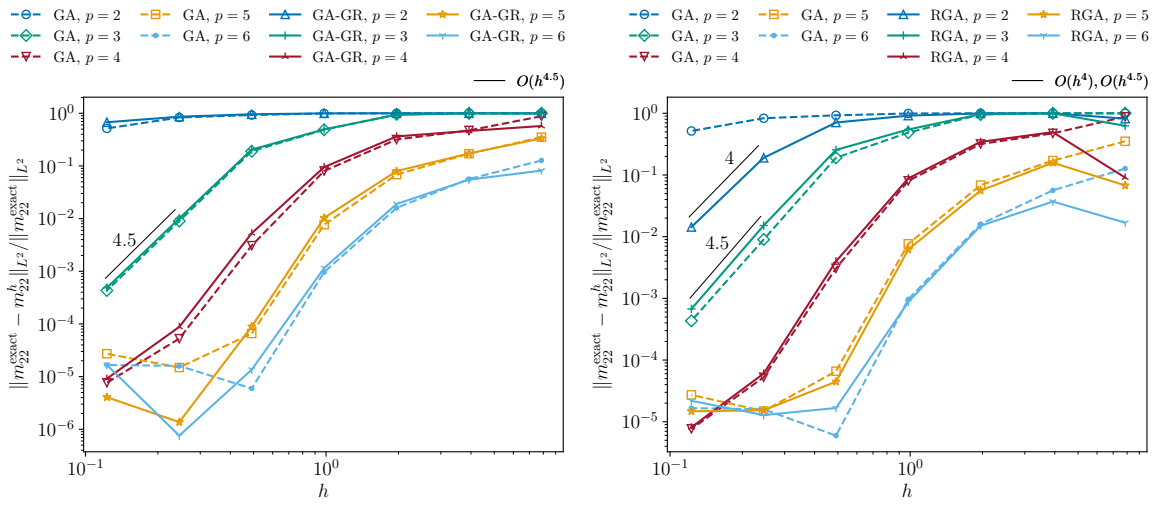

(e) $R/t = 10000$, GA VS GA-GR.

(f) $R/t = 10000$, GA VS RGA.

Figure 28: Cylindrical RM shell: Bending moment convergence rates for GA, GA-GR and RGA, increasing slenderness $R/t = 100, 1000, 10000$, degrees $p = 2$ to 6, and maximally smooth elements.

omitted for conciseness.

In addition to accuracy we also investigate the efficiency of the proposed quadrature rules. Figure 32 gives the computational time comparison between GA and the proposed rules, GA-GR and RGA, in computing stiffness matrices for the cylindrical RM shell problem. The routines for calculating stiffness matrices are the same for different quadrature rules and are implemented in Matlab [31]. For GA-GR and RGA, the computational time spent on calculating the quadrature points and weights is included. As can be seen in Figure 32a, compared with GA, the computational efficiency is improved by GA-GR for all degrees $p = 2$ to 6 as the meshes are refined. For $p >= 4$, the time ratios with respect to GA are smaller than 0.5, and they approach the ratios of the numbers of GA-GR and GA quadrature points as the basis degree increases. For instance, the time ratios for $p = 5$ and 6 are approximately 2/6 and 2/7, which are equal to the ratios of the numbers of GA-GR quadrature points to those of the GA quadrature points. This indicates that the time consumption determining the GA-GR rules is relatively small for higher-order bases. Note that here the ratios of quadrature point numbers, 2/6 and 2/7, are calculated from one-dimensional cases, because, as mentioned previously, only one element is used in the width direction and the numbers of quadrature points for GA-GR and GA are the same along the direction where only one element is used. Figure 32b shows the speedups of RGA with respect to GA. The time ratios are close to the ratios of quadrature point numbers for $p >= 4$. For example, for $p = 4$ the ratio is approximately 3/5, and for $p = 3$ and 5 the ratios are about 2/4 (or 3/6). Furthermore, for $p = 2$ and 3 we can observe that RGA shows faster speedups than GA-GR because they both have two quadrature points per element along the circumferential direction but the former does not require solving the moment-fitting equations to construct the rule. However, for $p > 4$ GA-GR becomes faster than RGA because asymptotically the number of quadrature points remains two.

Higher-order bases usually achieve better accuracy, but since they also result in an increased size of element matrices and increased bandwidth of the system matrices, the computational costs are higher than that for lower-order bases. To compare the efficiency of bases of different orders for the proposed quadrature rules, Figure 33 illustrates the convergence of the relative error of membrane force with respect to the computational time for GA-GR and GA, various basis degrees, $p = 2$ to 6, and different slendernesses, $R/t = 100$, 1000 and 10000. Unlike Figure 32, the computational time in Figure 33 not only consists of the time consumption for constructing quadrature rules and computing the stiffness matrices but also includes the time in solving the system equations, because different bandwidths resulting from various basis orders lead to different solution time. Note the computational time in Figure 33 is normalized by the maximum computational time consumed by the finest meshes of degree 6. Again, the initial mesh consists of 2×1 elements, as shown in Figure 24b, and h-refinement is used in the circumferential direction for all degrees. For GA-GR, as can be seen in Figures 33a, c and e, even though higher-order bases take more time than lower-order bases for the same mesh size, they achieve better accuracy for the same amount of computational time. As the slenderness increases, shell locking gets more severe and the superiority of higher-order bases becomes even more apparent. For instance, for slenderness $R/t = 10000$, the error for the lower-order basis ($p = 2$) does not even start to converge with the final refinement, for but higher-order bases, such as $p = 5$ and 6, it quickly converge to a number less than 5%. RGA shows similar behavior in Figures 33b, d and f, except that for $p = 5$ and 6 the computational efficiency is similar, because the basis functions of degree 6 are more accurate than those of degree 5, but employ one more quadrature point. As in our previous comprehensive studies of KL and RM shells [1], we conclude that $p = 5$ and 6, with our reduced rules RGA and GA-GR, produce accurate, efficient and almost locking-free solutions, unlike all $p \leq 4$.

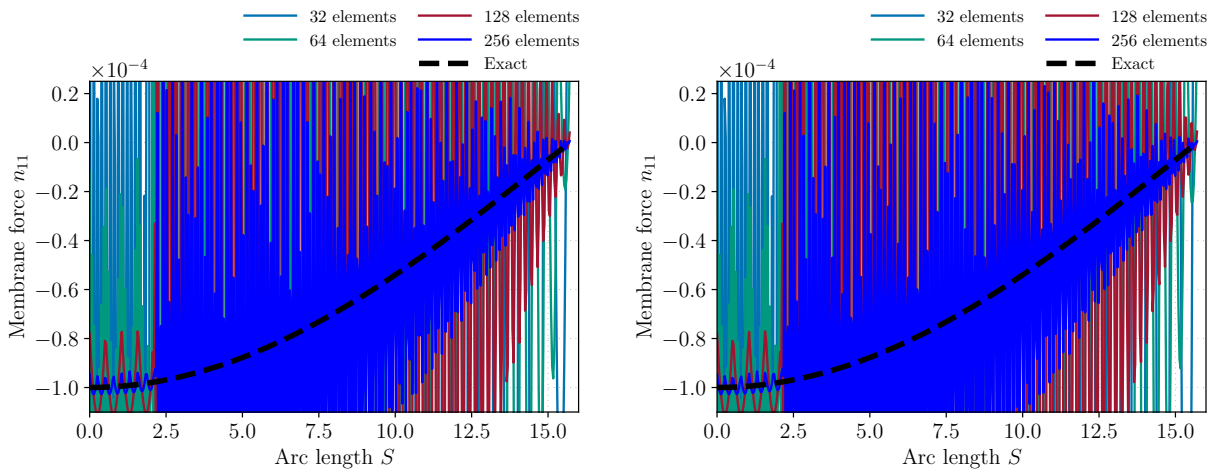

(a) GA, KL.

(b) GA, RM.

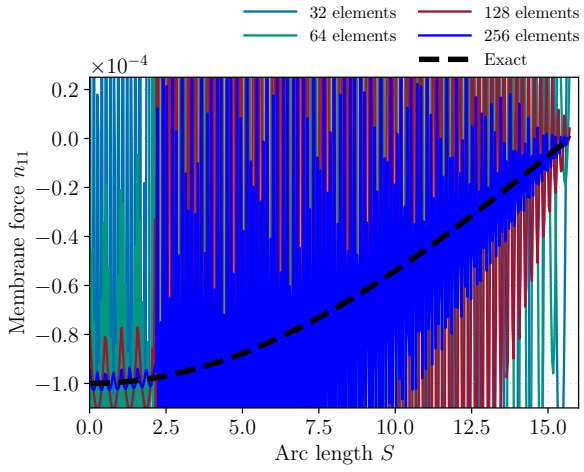

(c) GA-GR, KL.

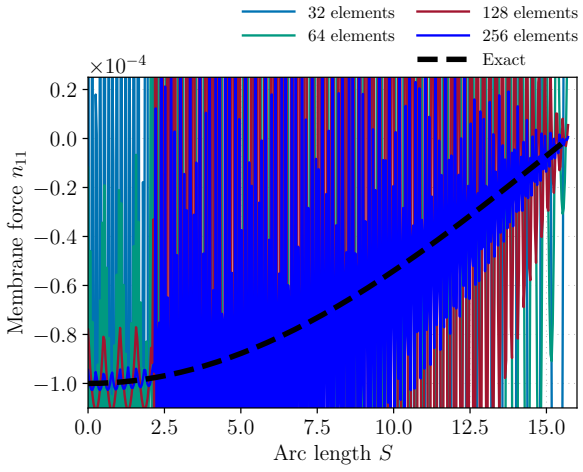

(d) GA-GR, RM.

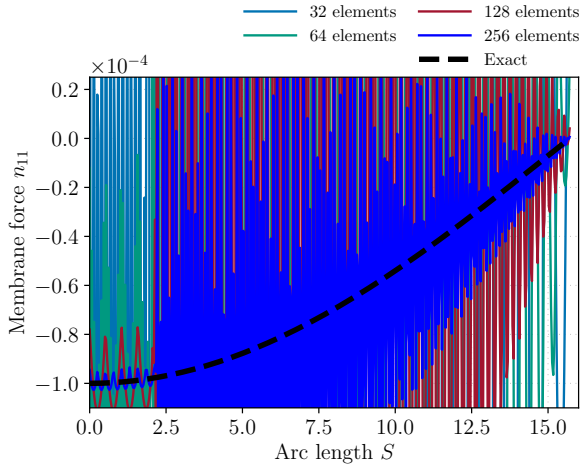

(e) RGA, KL.

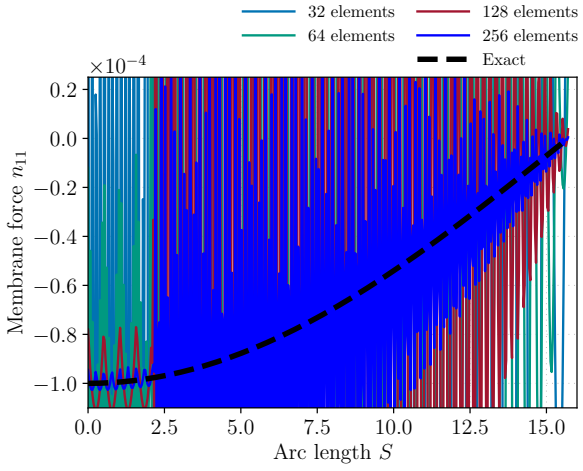

(f) RGA, RM.

Figure 29: Cylindrical KL (left) and RM (right) shells: Normalized membrane force n_{11} for GA,GA-GR and RGA, $R/t = 100$, $p = 2$, and various numbers of maximally smooth elements.

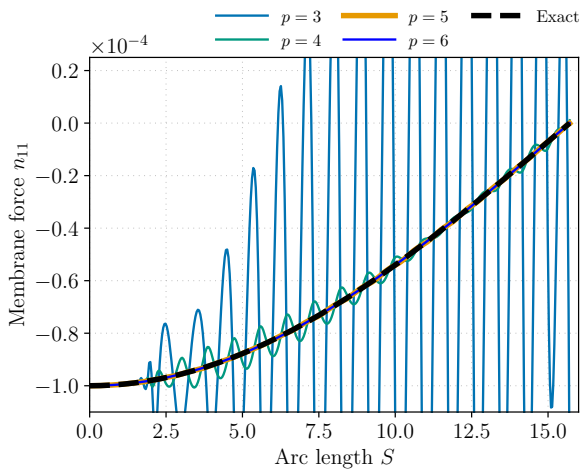

(a) GA, KL.

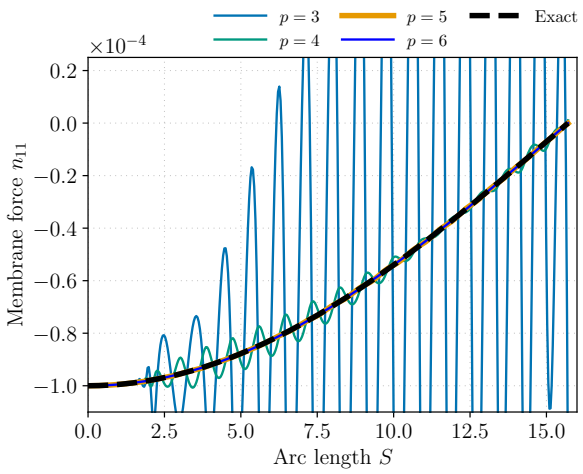

(b) GA, RM.

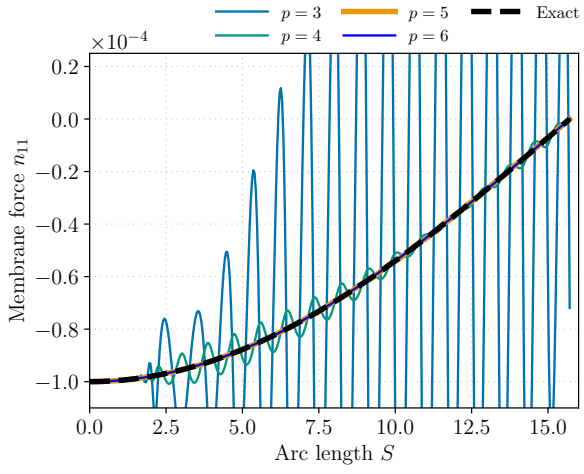

(c) GA-GR, KL.

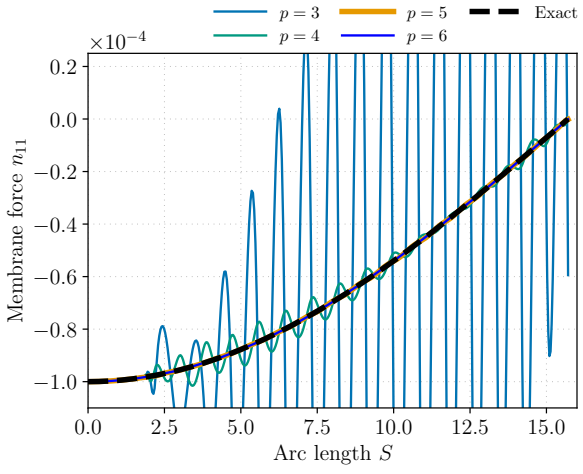

(d) GA-GR, RM.

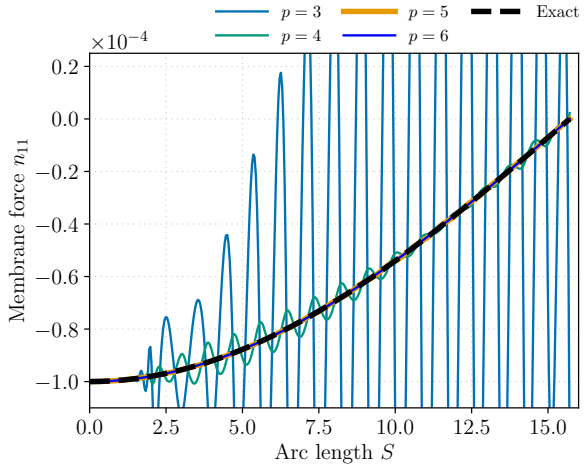

(e) RGA, KL.

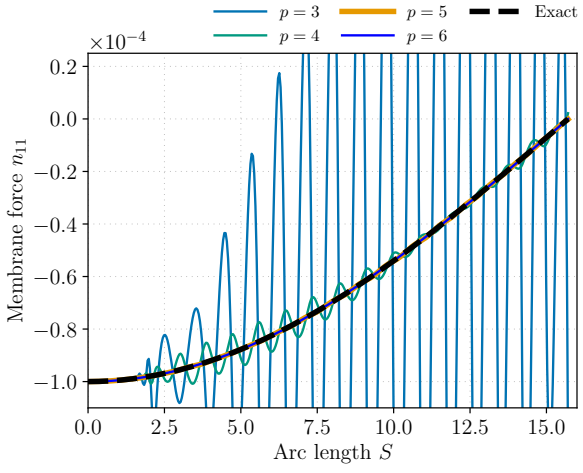

(f) RGA, RM.

Figure 30: Cylindrical KL (left) and RM (right) shells: Normalized membrane force n_{11} for GA, GA-GR and RGA, $R/t = 100$, $p = 3$ to 6, and 32 elements. Note that for $p \geq 5$, the results are free of oscillations.

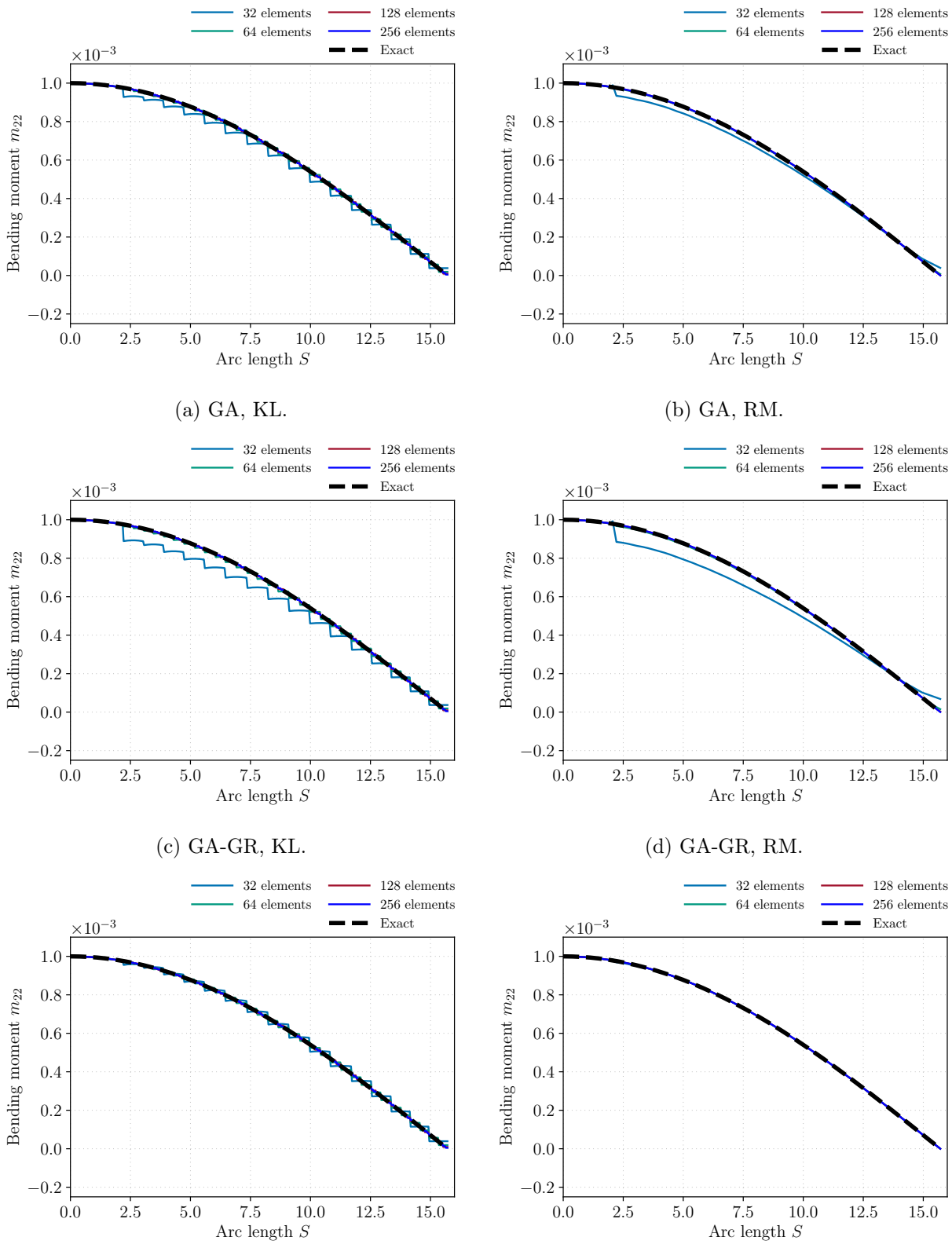

(a) GA, KL.

(b) GA, RM.

(c) GA-GR, KL.

(d) GA-GR, RM.

(e) RGA, KL.

(f) RGA, RM.

Figure 31: Cylindrical KL (left) and RM (right) shells: Normalized bending moment m_{22} for GA, GA-GR and RGA, $R/t = 100$, $p = 2$, and various numbers of maximally smooth elements.

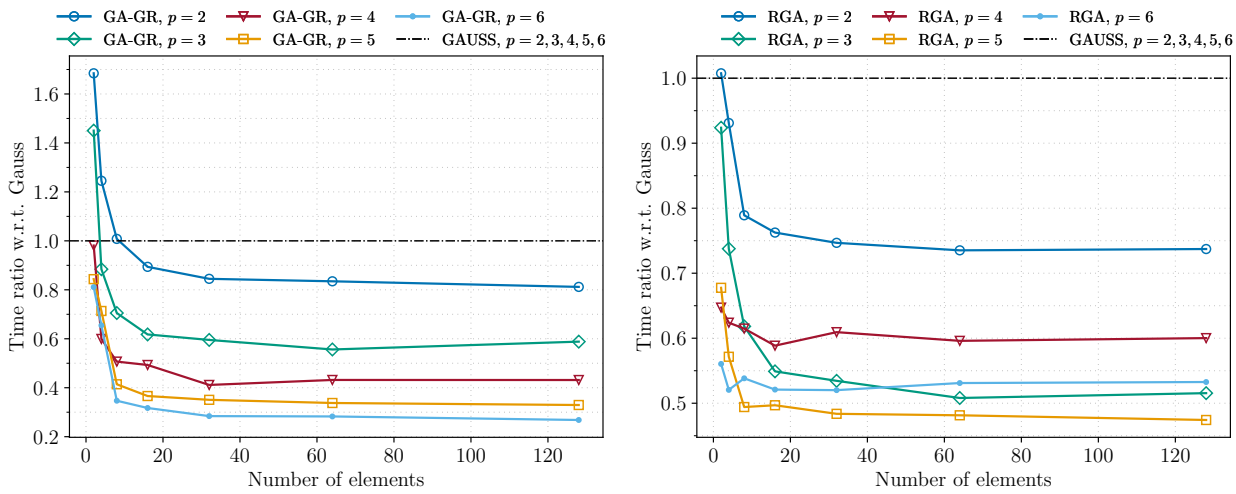

(a) GA-GR VS GA.

(b) RGA VS GA.

Figure 32: Cylindrical RM shell: Computational time of forming and assembling stiffness matrices for GA-GR and RGA, using $R/t = 1000$. Note that the time spent on computing the quadrature points and weights is included for GA-GR, RGA and GA. All calculations are done in Matlab [31] and time is measured by the `timeit` function.

5.6 Scordelis-Lo roof

The Scordelis-Lo roof problem is part of the so-called shell obstacle course [32] and tests a shell element's ability to handle both membrane and bending modes. An 80° arc of a cylinder with radius $R = 25$, length $L = 50$, and thickness $t = 0.25$ is supported on each end by a rigid diaphragm. It is loaded with its own weight $q_z = 90$. The Young's Modulus $E = 4.32 \times 10^8$ and Poisson's ratio $\nu = 0$. Figure 34a shows the problem setup. The initial mesh of the *entire* domain consists of 2×2 non-uniform Bézier elements as shown in Figure 34b, and h- and k-refinements are employed for convergence study. The maximum displacement happens on the free edge at $\frac{L}{2}$. The FEA benchmark displacement solutions converge to 0.3006 for KL shells [33, 34] and 0.3024 for RM shells [32, 35, 36]. The maximum displacement on the free edge at $\frac{L}{2}$ is monitored and results for the KL shell [1] with various quadrature rules are shown in Figure 35. As can be seen in Figure 35a, GA-GR achieves comparable results with GA for $p = 3$ to 6, which is consistent with the observations made in [1] for the Greville quadrature rules. Again, for GA-GR we omit the results for $p = 2$ here, because in this case GA-GR is simply Simpson's rule. Figure 35b shows that, for lower-order basis functions, $p = 2$ and 3, RGA obtains better results than GA. The reason for this is standard shell formulations tend to be stiff with full Gauss quadrature rules because of membrane-bending locking, which is alleviated by RGA. As the basis degrees increase to $p \geq 4$, locking phenomenon diminishes by higher-order basis functions [1, 37]. In these cases, the RGA rule converges from below to the reference solution with one refinement. Note that, even though RGA is less stiff for coarse meshes, the resulting condition numbers of the stiffness matrix are the same orders of magnitude as those obtained by the full Gauss quadrature rules. Figure 36 illustrates that the proposed quadrature rules with RM shells [1, 36, 35] behave similarly to what we observed for KL shells in Figure 35.

We next investigate the stress quality of the proposed quadrature rules for the Scordelis-Lo roof problem. Figure 37 gives a reference solution for the membrane force n_{11} that is used in [1] and calculated with full Gauss quadrature and 64×64 maximally smooth KL elements, $p = 7$. The

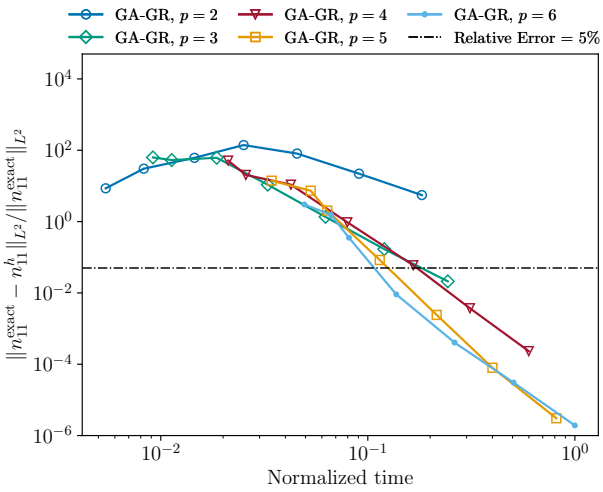

(a) $R/t = 100$, GA-GR.

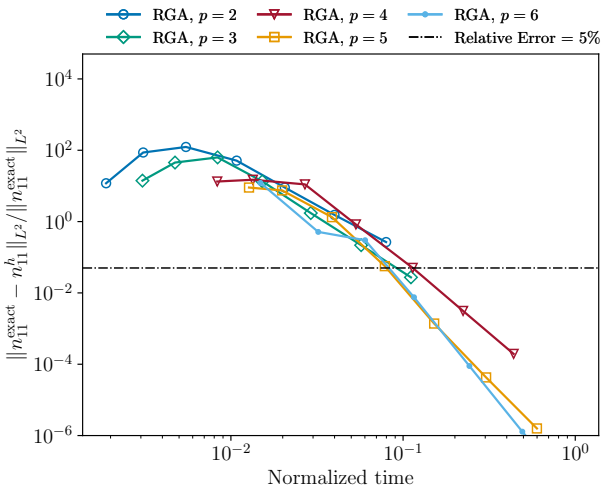

(b) $R/t = 100$, RGA.

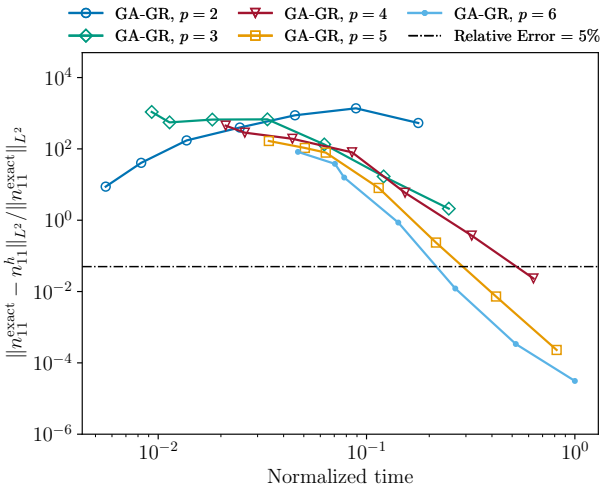

(c) $R/t = 1000$, GA-GR.

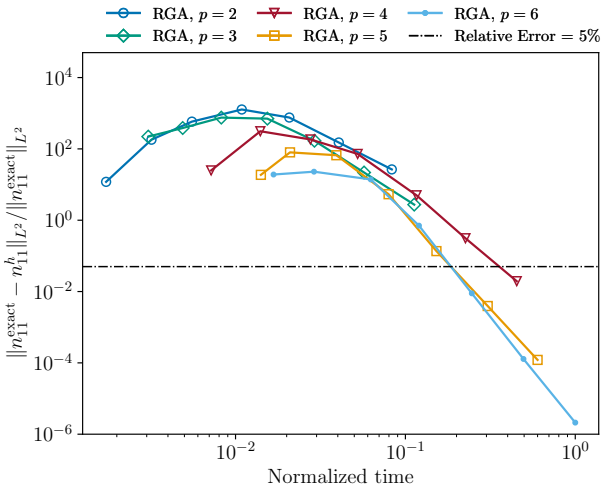

(d) $R/t = 1000$, RGA.

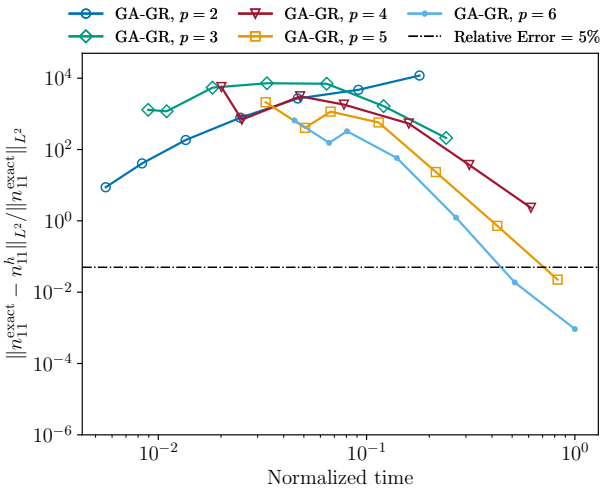

(e) $R/t = 10000$, GA-GR.

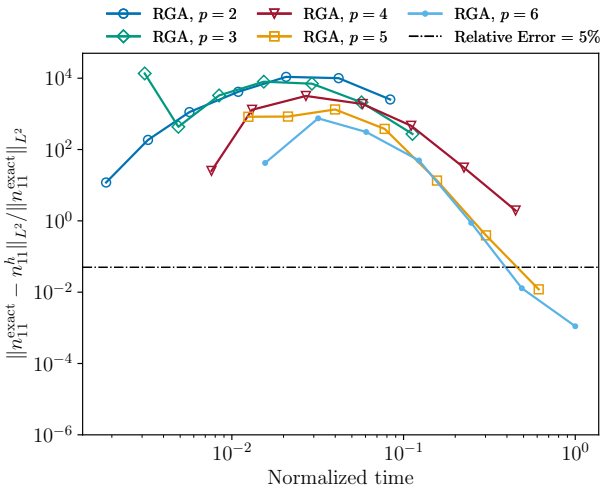

(f) $R/t = 10000$, RGA.

Figure 33: Cylindrical RM shell: Comparison of the computational efficiency for various basis degrees, $p = 2$ to 6, GA-GR and RGA. Note that the computational time, which includes the time consumption for constructing the quadrature rules, computing the stiffness matrices and solving the system equations, is normalized by the maximum computational time consumed by the finest meshes of degree 6. All calculations are done in Matlab [31] and time is measured by the `timeit` function.

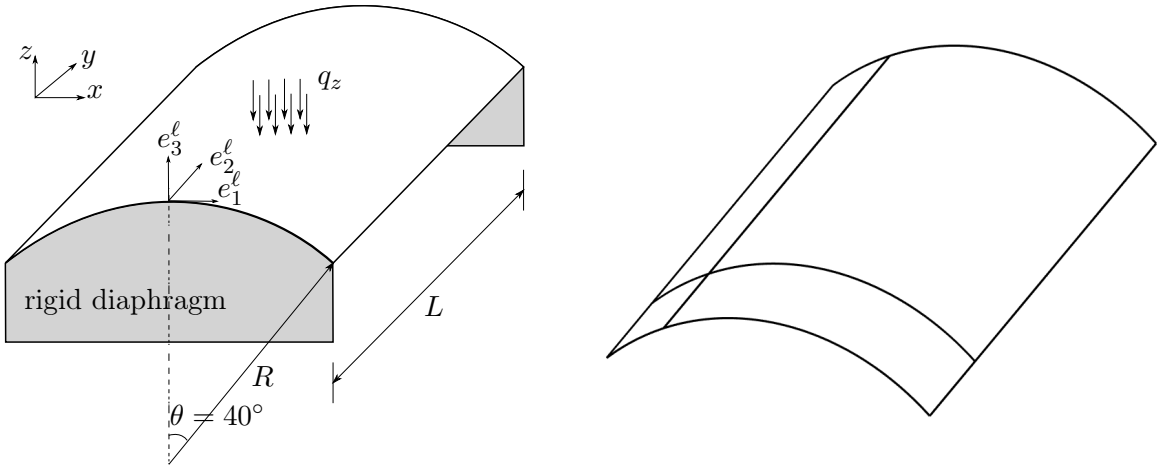

(a) Schematics. (b) Initial mesh.

Figure 34: Schematic and initial mesh for the Scordelis-Lo roof problem.

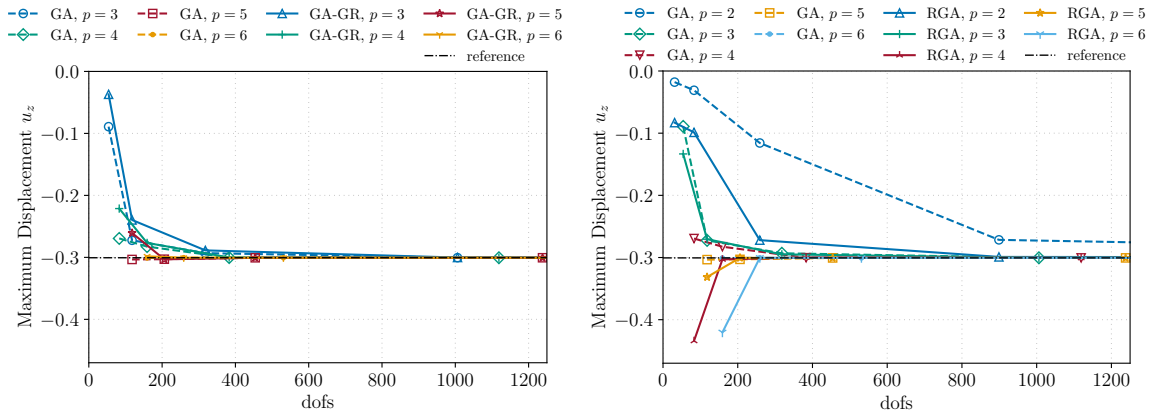

(a) GA VS GA-GR, $p = 3$ to 6. (b) GA VS RGA, $p = 2$ to 6.

Figure 35: Scordelis-Lo roof modeled as a KL shell: Convergence of the maximum displacement u_z for GA, GA-GR and RGA, and various basis degrees. The entire roof is modeled with an initial 2×2 mesh as shown in Figure 34b.

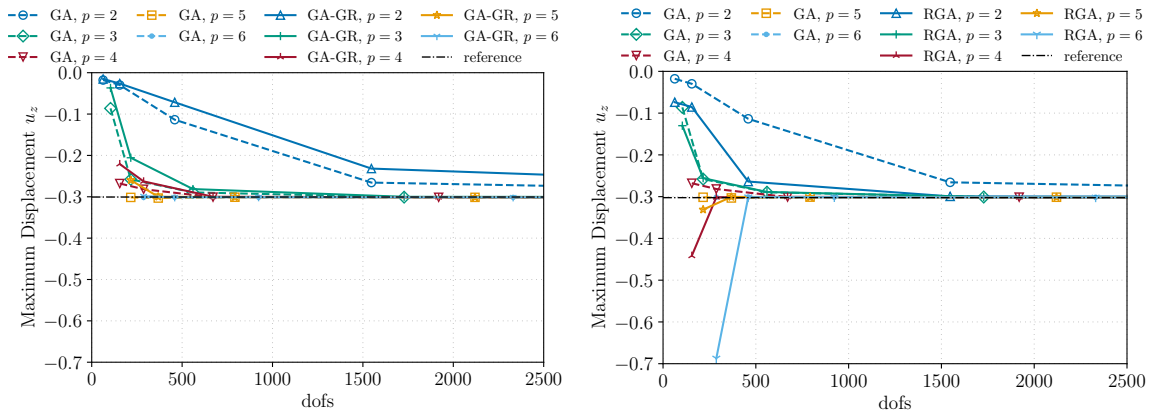

(a) GA VS GA-GR.

(b) GA VS RGA.

Figure 36: Scordelis-Lo roof modeled as an RM shell: Convergence of the maximum displacement u_z for GA, GA-GR and RGA, and degrees $p = 2$ to 6. The entire roof is modeled with an initial 2×2 mesh as shown in Figure 34b.

subscript "11" indicates the membrane force is in the circumferential direction. Figure 38 shows that KL shells with cubic basis functions exhibit significant membrane force oscillations, especially for coarse meshes, and GA, GA-GR and RGA basically achieve identical membrane force behavior for various numbers of elements. Figure 39 illustrates that, with 16×16 elements, the membrane force oscillations diminishes as we elevate the basis degrees. Again, the proposed GA-GR and RGA quadrature rules obtain similar results as the full Gauss quadrature for $p = 4$ to 6. As shown in Figures 40 and 41, the same observations can be made for RM shells with these quadrature rules, i.e., GA-GR and RGA behaving similarly as GA for all mesh sizes and basis degrees ranging from $p = 2$ to 6. Note that membrane force quality with KL shells, as shown in Figure 38, is better than that with RM shells, as shown in Figure 40, because the former uses cubic basis functions while the latter uses quadratic basis functions.

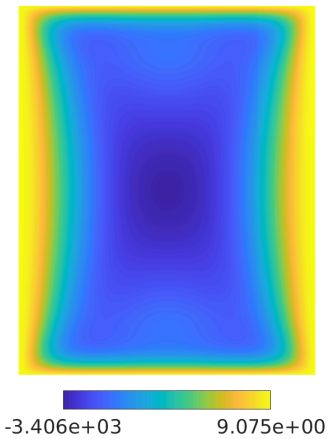

Figure 37: Scordelis-Lo roof modeled as a KL shell: Numerical reference of the membrane force n_{11}, calculated with full Gauss quadrature and 64×64 maximally smooth elements, $p = 6$.

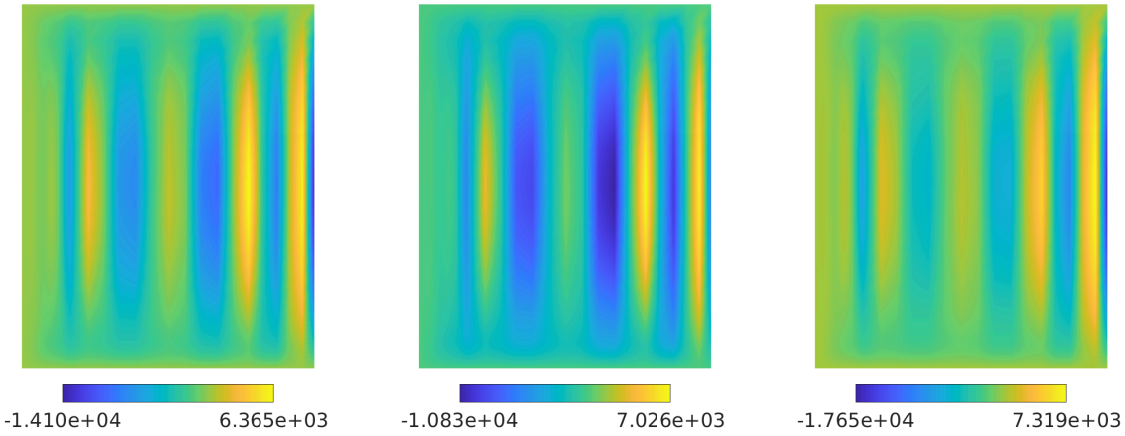

(a) GA, 8×8 elements. (b) GA-GR, 8×8 elements. (c) RGA, 8×8 elements.

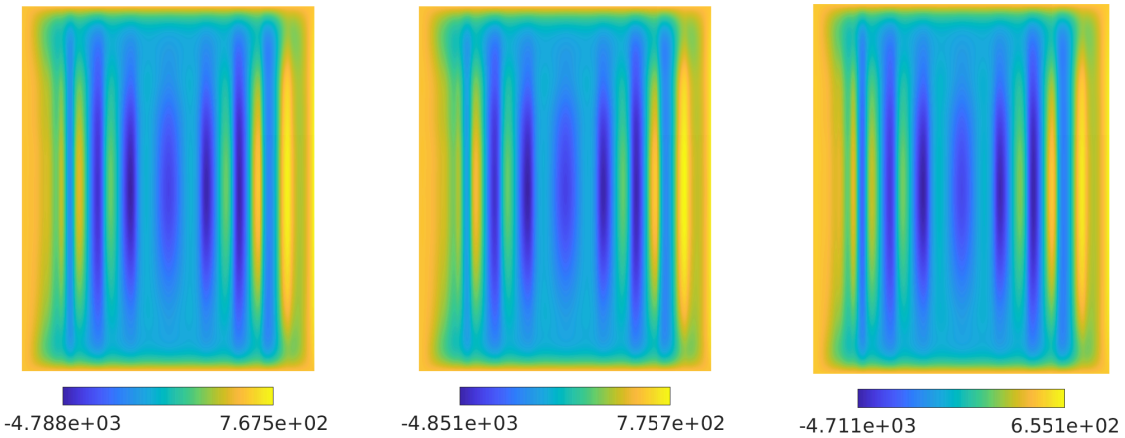

(d) GA, 16×16 elements. (e) GA-GR, 16×16 elements. (f) RGA, 16×16 elements.

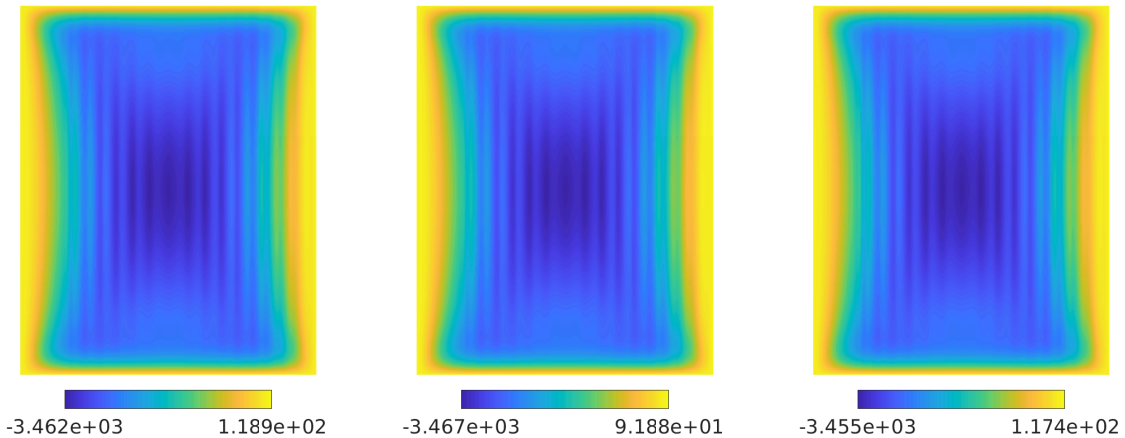

(g) GA, 32×32 elements. (h) GA-GR, 32×32 elements. (i) RGA, 32×32 elements.

Figure 38: Scordelis-Lo roof modeled as a KL shell: Membrane force n_{11} for GA (left), GA-GR (middle) and RGA (right), degree $p = 3$, and various numbers of elements.

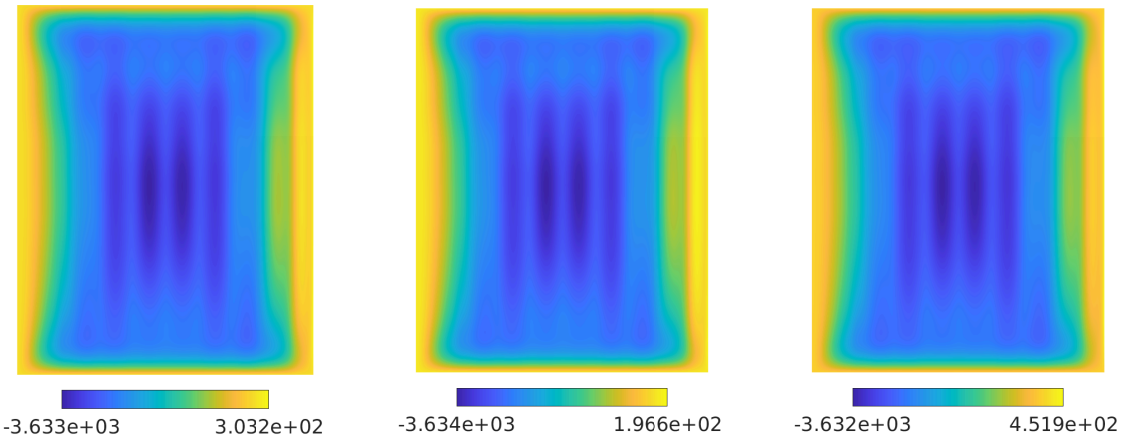

(a) GA, $p = 4$. (b) GA-GR, $p = 4$. (c) RGA, $p = 4$.

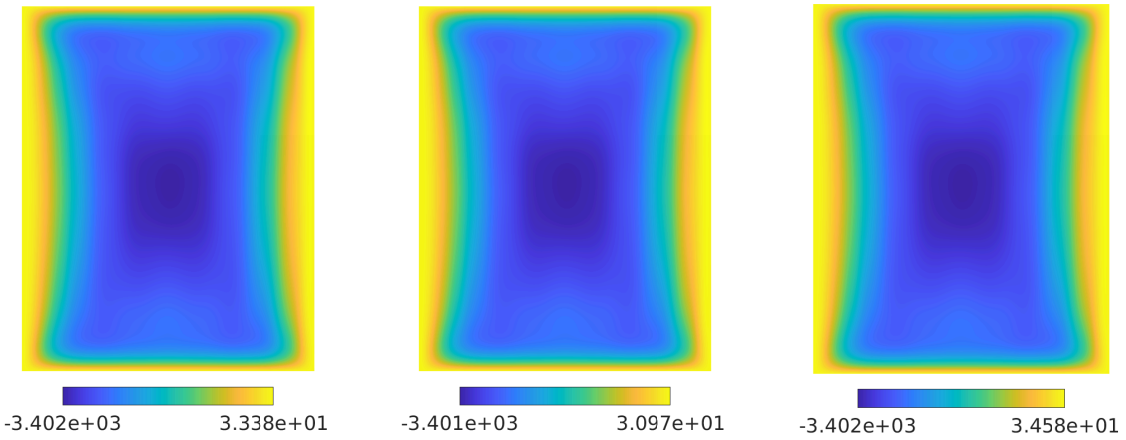

(d) GA, $p = 5$. (e) GA-GR, $p = 5$. (f) RGA, $p = 5$.

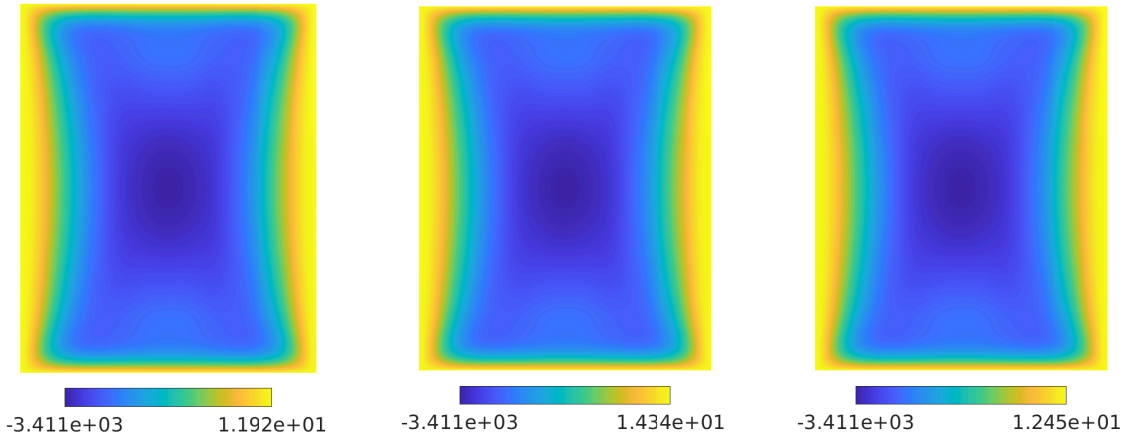

(g) GA, $p = 6$. (h) GA-GR, $p = 6$. (i) RGA, $p = 6$.

Figure 39: Scordelis-Lo roof modeled as a KL shell: Membrane force n_{11} for GA (left), GA-GR (middle) and RGA (right), degrees $p = 4$ to 6, and 16×16 elements.

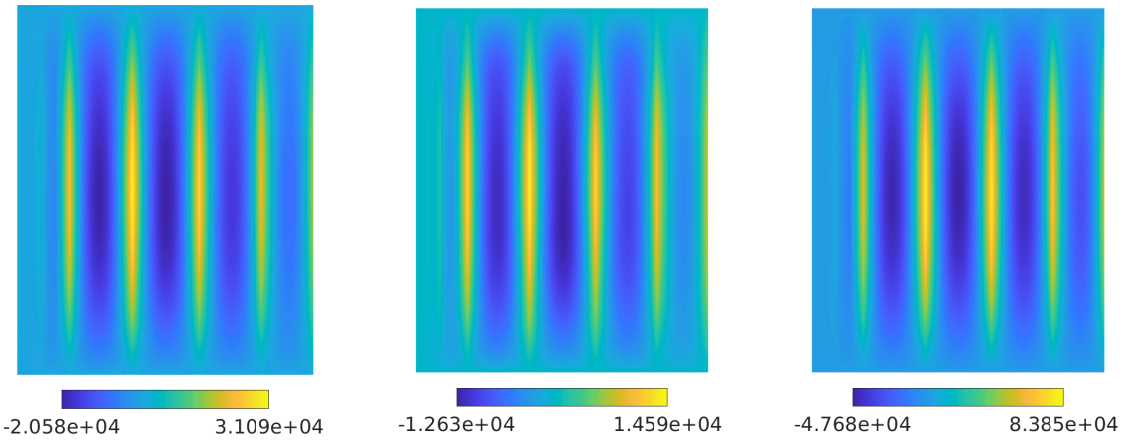

(a) GA, 8×8 elements. (b) GA-GR, 8×8 elements. (c) RGA, 8×8 elements.

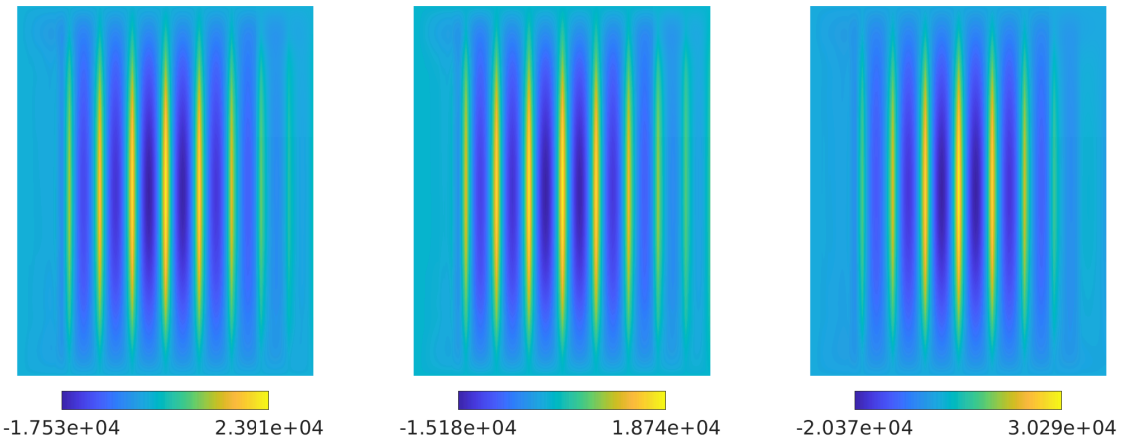

(d) GA, 16×16 elements. (e) GA-GR, 16×16 elements. (f) RGA, 16×16 elements.

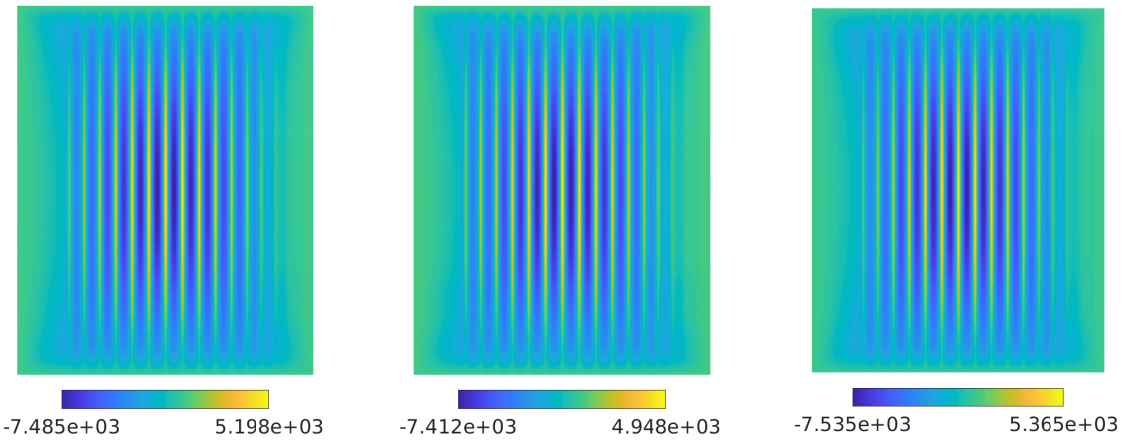

(g) GA, 32×32 elements. (h) GA-GR, 32×32 elements. (i) RGA, 32×32 elements.

Figure 40: Scordelis-Lo roof modeled as an RM shell: Membrane force n_{11} for GA (left), GA-GR (middle) and RGA (right), degree $p = 2$, and various numbers of elements.

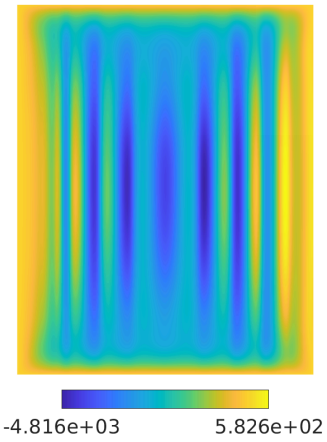

(a) GA, $p = 3$.

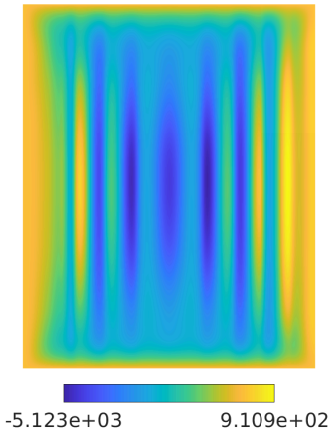

(b) GA-GR, $p = 3$.

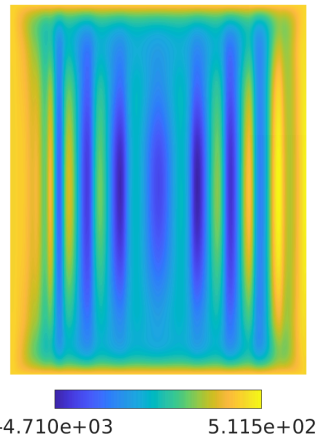

(c) RGA, $p = 3$.

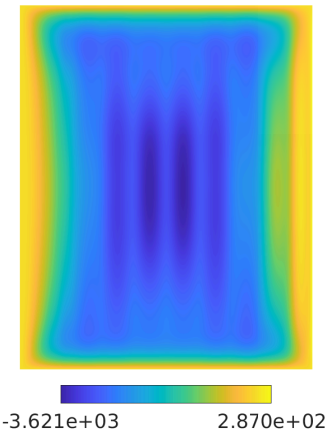

(d) GA, $p = 4$.

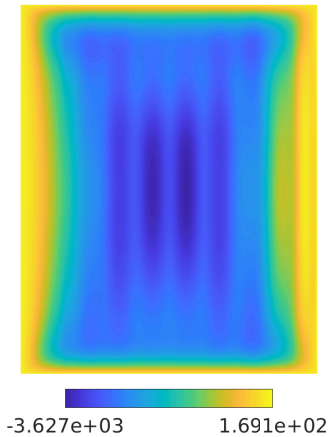

(e) GA-GR, $p = 4$.

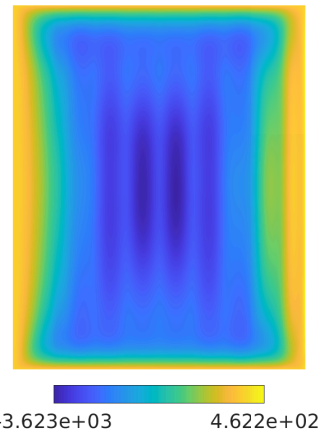

(f) RGA, $p = 4$.

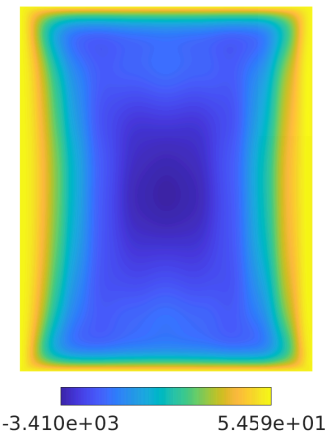

(g) GA, $p = 5$.

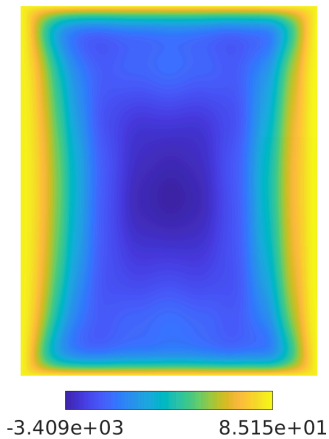

(h) GA-GR, $p = 5$.

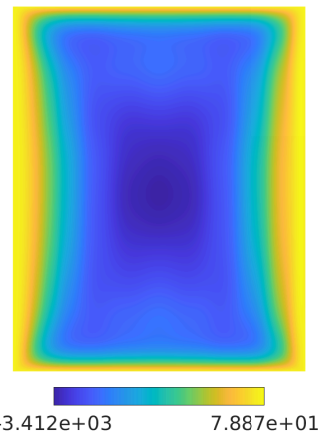

(i) RGA, $p = 5$.

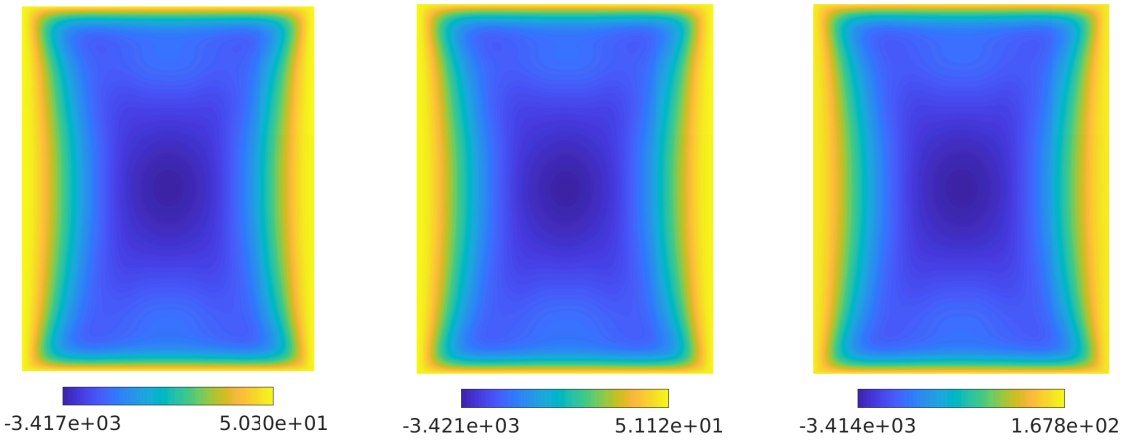

(j) GA, $p = 6$. (k) GA-GR, $p = 6$. (l) RGA, $p = 6$.

Figure 41: Scordelis-Lo roof modeled as an RM shell: Membrane force n_{11} for GA (left), GA-GR (middle) and RGA (right), degrees $p = 3$ to 6, and 16×16 elements.

5.7 Hemispherical shell with a hole

The hemispherical shell problem tests a shell element's ability to represent combined membrane and bending modes [38]. The geometry is a hemisphere with radius $R = 10$, thickness $t = 0.04$, and an 18° hole as shown in Figure 42a. Young's modulus is $E = 6.825 \times 10^7$ and Poisson's ratio is $\nu = 0.3$. The hemisphere is loaded with four point loads, $P = 200$, on the equator with alternating sign, which results in large deformations and rotations. Only one quarter of the hemisphere is modeled due to symmetry and its initial mesh is shown in Figure 42b. The radial displacement u_y at point B is monitored and compared against a reference solution of -5.86799 [35]. RM shell elements [1] are used in this problem.

Figure 43 shows the convergence of the radial displacement at point B for different quadrature rules and $p = 2$ to 6 with 10 equal load steps. As can be seen in Figure 43a, GA-GR behaves almost identically to GA for all degrees except for $p = 2$. In contrast, as shown in Figure 43b, RGA converges faster than GA for all degrees besides $p = 3$ due to its ability to alleviate locking.

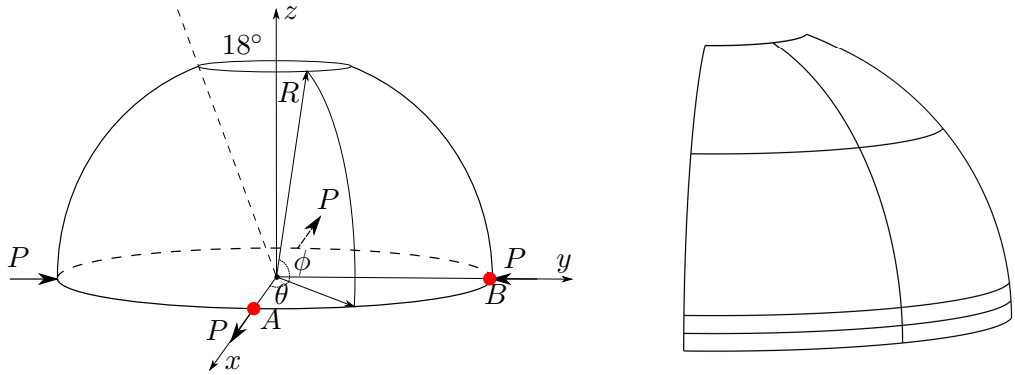

(a) Schematic. (b) Initial mesh.

Figure 42: Schematic for the hemispherical shell problem and initial mesh.

To achieve a relative displacement error $|u_B - u_{\text{ref}}|/|u_{\text{ref}}| < 5\%$ at point B, for $p = 5$, all three

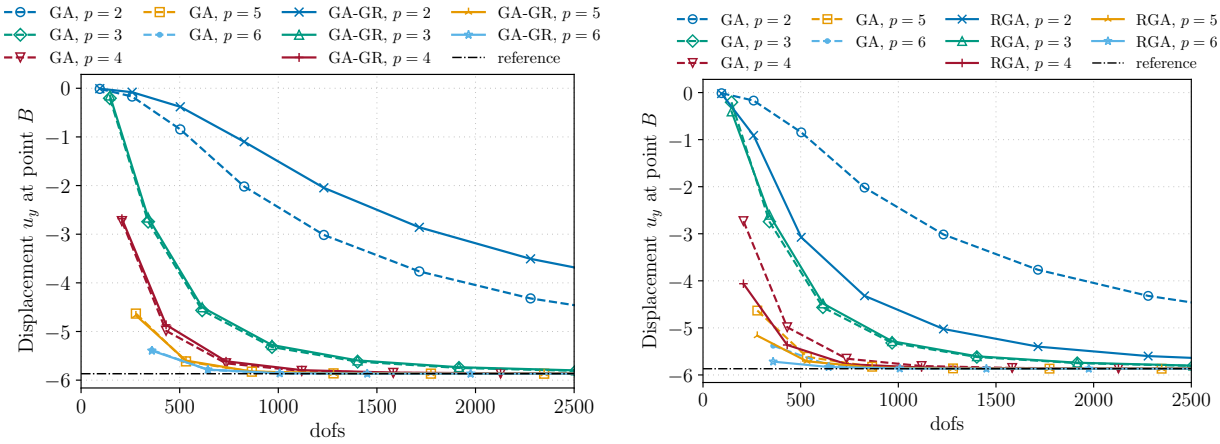

(a) GA VS GA-GR.

(b) GA VS RGA.

Figure 43: Hemispherical shell modeled as an RM shell: Convergence of the displacement u_y at point B for load $P = 200$ with GA, GA-GR and RGA, degrees $p = 2$ to 6, maximally smooth elements and 10 load steps.

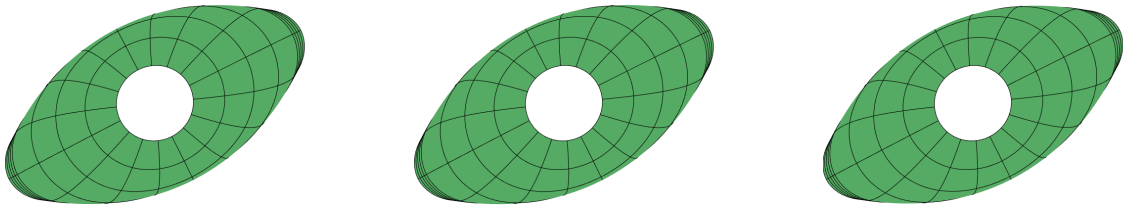

(a) GA, 8×4 elements.

(b) GA-GR, 8×4 elements.

(c) RGA, 8×4 elements.

Figure 44: Hemispherical shell and the RM shell: Deformed configurations with GA, GA-GR and RGA, maximally smooth quintic B-spline elements, $P = 200$ and 10 load steps, $|u_y - u_{\text{ref}}|/|u_{\text{ref}}| < 5\%$ at point B.

quadrature rules require 8×4 maximally smooth elements. The deformed configurations of the whole hemisphere are created by mirroring the quarter deformed configurations through symmetric planes, as shown in Figure 44. The Newton-Raphson iteration information for different quadratures is listed in Table 9. As can be seen, even though GA-GR and RGA use many fewer quadrature points, the total iteration numbers are less than that for GA.

Table 9: Hemispherical shell modeled as an RM shell: Newton-Raphson iteration behavior for GA, GA-GR and RGA rules with maximally smooth quintic B-spline elements and 10 load steps. A residual norm of 1×10^{-7} is used as the tolerance for convergence; the initial guess of each load step of the Newton-Raphson method is the solution of the previous load step.

Last load step iteration	Norm of the global residual vector		
	GA	GA-GR	RGA
1	1.4142136e+01	1.4142136e+01	1.4142136e+01
2	2.7041063e+04	2.6608136e+04	2.9705297e+04
3	6.4893743e+01	6.3193780e+01	7.6465420e+01
4	3.5557918e+01	3.6324569e+01	3.0491013e+01
5	1.1609915e+00	1.1040350e+00	1.5871918e+00
6	2.3217104e-02	2.2590331e-02	2.6317884e-02
7	1.7727158e-06	1.6449402e-06	1.9371570e-06
8	1.0504524e-07	5.3534915e-08	7.4704385e-08
9	3.6292899e-08		
10			
Element #	8×4	8×4	8×4
Total iteration #	95	94	92

6 Conclusions

We proposed a reduced Gauss quadrature rule and a Gauss-Greville quadrature rule for isogeometric analysis. Both quadrature rules are constructed so that basis functions in the space $\mathcal{S}_k^p$ can be integrated exactly, where $k = 1$ or 2 is the highest order of derivatives in the Galerkin formulation. This choice of accuracy requirement is inspired by the Greville quadrature rule [1], which revealed that the quadrature rules are stable and accurate for IGA if they satisfy this requirement. Unlike the existing Greville quadrature rule, the proposed quadrature rules are free of negative quadrature weights for arbitrary knot vectors, thus avoiding potential numerical instability. The reduced Gauss quadrature rule is constructed element-wise based on basis degrees and continuities; therefore it can be extened to unstructured meshes directly. Additionally, it asymptotically involves $\lceil (p+1)/2 \rceil$ quadrature points per element. The Gauss-Greville quadrature rule is constructed on the patch level and asymptotically uses the same number of quadrature points as the Greville quadrature rule, i.e., 2 points per element for $k = 1$ and 3 points for $k = 2$. Numerical examples with various element types demonstrate that for $k = 1$ the proposed quadrature rules achieve optimal convergence rates for $p = 2$, whereas for $p > 2$ the convergence rates are bounded above by 3.5 for the reduced Gauss rule and by 2.5 for the Gauss-Greville rule. For $k = 2$, the proposed quadrature rules even show higher convergence rates for the benchmarks considered, i.e., optimal convergence rates for $p = 2$ to 5 with Gauss-Greville quadrature and for $p = 2$ to 6 with reduced Gauss quadrature. All these convergence rates are in terms of the L^2-norm error of either the first derivative of the solution or the stress. Despite the suboptimal convergence rates for higher-order bases ($p > 2$), several examples illustrate that the resulting stress results hardly differ from those obtained from full Gauss quadrature, which indicates the proposed quadrature rules are sufficiently accurate for engineering applications. The reduced convergence rates for $p = 5$, 6 are counterbalanced by significant reduction in the number of quadrature points, compared with Gauss quadrature, and the mitigation of membrane-bending and transverse shear locking in curved shell analysis. In fact, for large scale engineering problems involving complex geometry and contact, etc., optimal convergence rates are difficult to achieve

even with exact quadrature rules. We note that the convergence study in this work is conducted numerically. A rigorous mathematical proof of the observed convergence rates is an interesting topic, but is beyond the scope of the current work.

In summary, the proposed quadrature rules are easy to construct, are stable and accurate, and provide efficient alternatives for widely used full Gauss quadrature rule. To minimize the number of quadrature points, the following guidelines are suggested for practical usage:

- For $k = 1$ and $p = 2, 3$, the reduced Gauss quadrature rule asymptotically uses two quadrature points per element, which is the same as the Gauss-Greville quadrature rule. Therefore, for these cases, the reduced Gauss quadrature rule is preferred as it is simpler to construct. For higher-order bases, i.e., $p > 3$, the Gauss-Greville quadrature rule is suggested as it uses fewer quadrature points.

- For $k = 2$ and $p \leq 5$, the reduced Gauss quadrature rule asymptotically requires two points per element for $p = 2, 3$ and three points for $p = 4, 5$, while the Gauss-Greville rule asymptotically requires three points for all these cases. So the reduced Gauss quadrature is recommended for these cases. For $p > 5$, the Gauss-Greville rule is preferred.

In curved shell applications, if locking is severe, we recommend using $p = 5$ or 6 as locking is mitigated and at the same time, relatively few quadrature points are required.

References

[1] Z. Zou, T. J. R. Hughes, M. A. Scott, R. A. Sauer, E. J. Savitha, Galerkin formulations of isogeometric shell analysis: Alleviating locking with Greville quadratures and higher-order elements, Computer Methods in Applied Mechanics and Engineering 380 (2021) 113757.

[2] T. J. R. Hughes, J. A. Cottrell, Y. Bazilevs, Isogeometric analysis: CAD, finite elements, NURBS, exact geometry and mesh refinement, Computer Methods in Applied Mechanics and Engineering 194 (2005) 4135–4195.

[3] T. J. R. Hughes, A. Reali, G. Sangalli, Duality and unified analysis of discrete approximations in structural dynamics and wave propagation: Comparison of p-method finite elements with k-method NURBS, Computer Methods in Applied Mechanics and Engineering 197 (2008) 4104–4124.

[4] J. A. Cottrell, A. Reali, Y. Bazilevs, T. J. R. Hughes, Isogeometric analysis of structural vibrations, Computer Methods in Applied Mechanics and Engineering 195 (2006) 5257–5296.

[5] Y. Bazilevs, V. M. Calo, J. A. Cottrell, T. J. R. Hughes, A. Reali, G. Scovazzi, Variational multiscale residual-based turbulence modeling for large eddy simulation of incompressible flows, Computer Methods in Applied Mechanics and Engineering 197 (2007) 173–201.

[6] T. J. R. Hughes, A. Reali, G. Sangalli, Efficient quadrature for NURBS-based isogeometric analysis, Computer Methods in Applied Mechanics and Engineering 199 (2010) 301–313.

[7] C. Adam, T. J. R. Hughes, S. Bouabdallah, M. Zarroug, H. Maitournam, Selective and reduced numerical integrations for NURBS-based isogeometric analysis, Computer Methods in Applied Mechanics and Engineering 284 (2015) 732–761.

[8] F. Auricchio, F. Calabrò, T. J. R. Hughes, A. Reali, G. Sangalli, A simple algorithm for obtaining nearly optimal quadrature rules for NURBS-based isogeometric analysis, Computer Methods in Applied Mechanics and Engineering 249–252 (2012) 15–27.

[9] K. A. Johannessen, Optimal quadrature for univariate and tensor product splines, Computer Methods in Applied Mechanics and Engineering 316 (2017) 84–99.

[10] M. Bartoň, R. Ait-Haddou, V. M. Calo, Gaussian quadrature rules for C^1 quintic splines with uniform knot vectors, Journal of Computational and Applied Mathematics 322 (2017) 57–70.

[11] R. Ait-Haddou, M. Bartoň, V. M. Calo, Explicit Gaussian quadrature rules for C^1 cubic splines with symmetrically stretched knot sequences, Journal of Computational and Applied Mathematics 290 (2015) 543–552.

[12] M. Bartoň, V. M. Calo, Gaussian quadrature for splines via homotopy continuation: Rules for C^2 cubic splines, Journal of Computational and Applied Mathematics 296 (2016) 709–723.

[13] P. Chen, X. Li, Explicit Gaussian Quadrature Rules for $$CÎ$$ Cubic Splines with Non-uniform Knot Sequences, Communications in Mathematics and Statistics 9 (2021) 331–345.

[14] F. Calabrò, G. Sangalli, M. Tani, Fast formation of isogeometric Galerkin matrices by weighted quadrature, Computer Methods in Applied Mechanics and Engineering 316 (2017) 606–622.

[15] R. R. Hiemstra, G. Sangalli, M. Tani, F. Calabrò, T. J. R. Hughes, Fast formation and assembly of finite element matrices with application to isogeometric linear elasticity, Computer Methods in Applied Mechanics and Engineering 355 (2019) 234–260.

[16] D. Schillinger, S. J. Hossain, T. J. R. Hughes, Reduced Bézier element quadrature rules for quadratic and cubic splines in isogeometric analysis, Computer Methods in Applied Mechanics and Engineering 277 (2014) 1–45.

[17] W. J. Gordon, R. F. Riesenfeld, B-spline Curves and Surfaces, in: Computer Aided Geometric Design, Elsevier, 1974, pp. 95–126.

[18] S. Hubrich, P. Di Stolfo, L. Kudela, S. Kollmannsberger, E. Rank, A. Schröder, A. Düster, Numerical integration of discontinuous functions: Moment fitting and smart octree, Computational Mechanics 60 (2017) 863–881.

[19] M. Joulaian, S. Hubrich, A. Düster, Numerical integration of discontinuities on arbitrary domains based on moment fitting, Computational Mechanics 57 (2016) 979–999.

[20] C. K. Chui, W. He, J. Stöckler, Nonstationary tight wavelet frames, I: Bounded intervals, Applied and Computational Harmonic Analysis 17 (2004) 141–197.

[21] Z. Zou, Isogeometric Shell Analysis: Multi-patch Coupling and Overcoming Locking, Ph.D. thesis, Brigham Young Unversity, Provo, 2020.

[22] S. Salsa, Partial Differential Equations in Action, volume 86 of *UNITEXT*, Springer International Publishing, Cham, 2015.

[23] G. Strang, G. Fix, An Analysis of the Finite Element Method, 2nd edition ed., Wellesley-Cambridge Press, Wellesley, Mass, 2008.

[24] T. J. Hughes, J. A. Evans, A. Reali, Finite element and NURBS approximations of eigenvalue, boundary-value, and initial-value problems, Computer Methods in Applied Mechanics and Engineering 272 (2014) 290–320.

[25] G. Xu, B. Mourrain, R. Duvigneau, A. Galligo, Parameterization of computational domain in isogeometric analysis: Methods and comparison, Computer Methods in Applied Mechanics and Engineering 200 (2011) 2021–2031.

[26] G. Xu, M. Li, B. Mourrain, T. Rabczuk, J. Xu, S. P. A. Bordas, Constructing IGA-suitable planar parameterization from complex CAD boundary by domain partition and global/local optimization, Computer Methods in Applied Mechanics and Engineering 328 (2018) 175–200.

[27] M. Kumar, T. Kvamsdal, K. A. Johannessen, Superconvergent patch recovery and a posteriori error estimation technique in adaptive isogeometric analysis, Computer Methods in Applied Mechanics and Engineering 316 (2017) 1086–1156.

[28] D. Miao, Z. Zou, M. A. Scott, M. J. Borden, D. C. Thomas, Isogeometric Bézier dual mortaring: The enriched Bézier dual basis with application to second- and fourth-order problems, Computer Methods in Applied Mechanics and Engineering 363 (2020) 112900.

[29] J. A. Cottrell, T. J. R. Hughes, Y. Bazilevs, Isogeometric Analysis: Toward Integration of CAD and FEA, John Wiley & Sons, 2009.

[30] Z. Zou, M. A. Scott, M. J. Borden, D. C. Thomas, W. Dornisch, E. Brivadis, Isogeometric Bézier dual mortaring: Refineable higher-order spline dual bases and weakly continuous geometry, Computer Methods in Applied Mechanics and Engineering 333 (2018) 497–534.

[31] Matlab, Version R2020a (9.8.0.1323502), The MathWorks Inc., Natick, Massachusetts, 2020.

[32] R. Macneal, R. Harder, A proposed standard set of problems to test finite element accuracy, Finite Elements in Analysis and Design 1 (1985) 3–20.

[33] J. Kiendl, K.-U. Bletzinger, J. Linhard, R. Wüchner, Isogeometric shell analysis with Kirchhoff–Love elements, Computer Methods in Applied Mechanics and Engineering 198 (2009) 3902–3914.

[34] Y. Guo, Z. Zou, M. Ruess, Isogeometric multi-patch analyses for mixed thin shells in the framework of non-linear elasticity, Computer Methods in Applied Mechanics and Engineering 380 (2021) 113771.

[35] W. Dornisch, R. Müller, S. Klinkel, An efficient and robust rotational formulation for isogeometric Reissner–Mindlin shell elements, Computer Methods in Applied Mechanics and Engineering 303 (2016) 1–34.

[36] Z. Zou, M. A. Scott, D. Miao, M. Bischoff, B. Oesterle, W. Dornisch, An isogeometric Reissner–Mindlin shell element based on Bézier dual basis functions: Overcoming locking and improved coarse mesh accuracy, Computer Methods in Applied Mechanics and Engineering 370 (2020) 113283.

[37] R. Echter, M. Bischoff, Numerical efficiency, locking and unlocking of NURBS finite elements, Computer Methods in Applied Mechanics and Engineering 199 (2010) 374–382.

[38] R. MacNeal, Finite Elements: Their Design and Performance, M. Dekker, New York, 1994.